Université de Toulouse

THÈSE

En vue de l'obtention du
DOCTORAT DE L'UNIVERSITÉ DE TOULOUSE

Délivré par:
Université Toulouse III Paul Sabatier (UT3 Paul Sabatier)

Discipline ou spécialité:
Mathématiques Appliquées

Présentée et soutenue par
Thi-Bich-Ngoc MAC
le: 1 Octobre 2014

Titre:
Modélisation des suspensions de particules actives: application à la motilité séminale

---

École doctorale :
Mathématiques Informatique Télécommunications (MITT)

Unité de recherche:
UMR 5219

Directeurs de thèse:
Pierre DEGOND, Chair Professor, Imperial College, London
Giacomo DIMARCO, Professor, University of Ferrara

Rapporteurs:
Bernt WENNBERG, Professor, Chalmers University of Technology, Göteborg, Suède
Cécile APPERT-ROLLAND, Director of Research, Université Paris- Sud, Orsay, France

Autres membres du jury:
Bertrand MAURY, Professeur, Université Paris- Sud, Orsay
Christophe BESSE, Professeur, Université Paul Sabatier, Toulouse
Giacomo DIMARCO, Professor, University of Ferrara, Italie
Franck PLOURABOUÉ, Directeur de Recherche, IMFT, Toulouse.

Remerciements

Je voudrais tout d'abord remercier Pierre Degond pour m'avoir donné l'opportunité de travailler sur ce sujet passionnant, d'abord pour mon stage de master 2 et ensuite pour cette thèse. Il m'a donné aussi l'opportunité de travailler pendant une longue periode de 6 mois à l'Imperial College où l'environnement scientifique très stimulant. Pour sa patience, son calme, sa compréhension et sa gentillesse ainsi que pour les nombres heures d'écoutes qu'il m'a accordé et qui m'a permi de mener à bien ce projet. Je suis fier de l'avoir rédigée sous sa direction. Je tiens aussi à remercier mon co-directeur de thèse Giacomo Dimarco qui a su me guider sur touts les simulations numeriques. Merci encore à touts les deux pour leur engagement et leur soutien durant ces années.

Je tiens ensuite à remercier toutes les personnes avec qui j'ai eu la chance de colaborer: Franck Plouraboué, Olivier Praud, Éric Climent. Ils sont du laboratoire de physiques IMFT où j'ai effectué touts les manips sur les bugs. Je remercie encore Franck pour m'avoir donné ses nombreux conseils. Pour sa gentillesse, sa patience et l'excellente ambiance qui a régné durant tout la période à IMFT.

Je souhaiterais remercier mes rapporteurs Bernt Wennberg and Cécile Appert-Rolland qui ont passés du temps sur mon manuscript et dont les commentaires ont été des plus detaillés.

Je souhaiterais exprimer un grand merci à Bertrand Maury, Christophe Besse, Giacomo Dimarco et Franck Plouraboué pour leur participations à mon jury.

Je remercie à mon "grand frère" Sébastien Motsch qui m'a aidé de préciser pour les travails de simulations.

J'adresse mes remerciments à José Antonio Carrillo et ses post-docs avec qui j'ai passé des bons moments aux séminares internes et aux déjeuners pendant la période à Londres.

Je remercie sincèrement à Nguyen Tien Zung pour leur conseils, leur enseignement en Mathématiques. Je recercie aussi mes amis Vienamiens qui m'ont soutenu pendant mes années à Toulouse.

Je remercie également Nan, Hui, Adama, Blaise pour tout le temps passé ensemble que ce soit pour le travail ou en dehors. Merci encore à Nan et Hui avec qui j'ai eu de longues discussions sur le travail dans la thèse.

Enfin, je tiens à remercier mon copain Chinh pour m'avoir apporté beaucoup de bonheur et de me donner la force nécessaire pour accomplir tout ce que j'entreprends. Merci encore d'avoir passé ses nombres d'heures pour m'aider à corriger des erreurs anglaise et francaise dans ma thèse. Merci à ma famille pour mille choses, mais surtout, pour etre là tout simplement.

Résumé

Dans cette thèse, nous étudions le comportement collectif de particules auto-propulsées. Ce travail comporte trois parties.

Dans la première partie, nous considérons un modèle individu-centré pour les particules d'auto rotation interagissant par une règle d'alignement et étudions leurs limites macroscopiques. Ce modèle décrit des particules auto-propulsées qui ont des fréquences de rotation propre et s'alignent à chaque pas de temps avec la vitesse moyenne de leurs voisins. Deux cas de scaling ont été étudiés. Dans le cas de petite vitesse angulaire, le modèle obtenu est une légère modification du modèle 'Hydrodynamique auto-organisé' qui avait été introduit précédemment par Degond et Mostch. Dans le cas de grande vitesse angulaire, le modèle obtenu est plus compliqué. Une étude préliminaire de la stabilité linéaire a été également proposée.

Le principal objet de la deuxième partie est le modèle de Vicsek avec répulsion. Plus précisément, nous étudions un système de particules auto-propulsées interagissant avec leurs voisins par une règle d'alignement et de répulsion. Les vitesses des particules résultent de l'auto-propulsion et de la force répulsive. La direction de l'auto-propulsion est alignée à celle de leurs voisins, à un bruit près. Un modèle continu a été dérivé à partir d'une équation cinétique du système de particules. Il nous amène à un système d'équations hydrodynamique non-conservatif. Nous fournissons une validation numérique de ce modèle en le comparant avec le modèle individu centré. L'existence de solutions à deux dimensions est prouvée en utilisant la méthode standard de Galerkin pour les équations quasi-linéaires paraboliques. D'autre part, nous avons effectué des simulations pour comparer les résultats théoriques et numériques

La dernière partie est consacrée à l'étude expérimentale du comportement collectif de robots auto-propulsés dans une enceinte annulaire confinée. Les observations mettent un évidence une organisation du mouvement où les individues s'alignent orthogonalement au bord de l'enceinte annulaire, pour fomer des paquets (clusters) dérivants. Un modèle microscopique numérique est capable de reproduire qualitativement ces comportements.

Contents

1 General Introduction 9
- 1.1 Motivation . . . 9
- 1.2 Overview of the subject . . . 10
  - 1.2.1 Pure alignment model: The Vicsek model and its variants . . . 10
  - 1.2.2 Pure attraction-repulsion models . . . 12
  - 1.2.3 Combined alignment and attraction-repulsion models . . . 13
  - 1.2.4 Synchronization and combined alignment and synchronization models . . . 13
  - 1.2.5 Models and experiments . . . 14
- 1.3 Presentation of main results . . . 14
  - 1.3.1 Chapter 1: The Vicsek - Kuramoto model . . . 14
  - 1.3.2 Chapter 2: The Vicsek model with repulsion . . . 15
  - 1.3.3 Chapter 3. The existence of solution of the SOHR model: comparison between theory and simulations . . . 16
  - 1.3.4 Chapter 4: Experiments . . . 17

Part I: The Vicsek-Kuramoto model 21

2 Hydrodynamics of the Kuramoto-Vicsek model of rotating self-propelled particles 21
- 2.1 Introduction . . . 21
- 2.2 Individual-Based model, mean-field limit and scaling . . . 23
- 2.3 Small angular velocities . . . 27
- 2.4 Large angular velocities . . . 30
- 2.5 Properties of the SOHPR-L hydrodynamic model . . . 33
  - 2.5.1 Linearized stability of the SOHPR-L system . . . 34
  - 2.5.2 Small angular velocity limit of the SOHPR-L model . . . 36
- 2.6 Conclusion and perspectives . . . 38
- Appendix A Small angular velocity . . . 40
  - A1 Determination of the equilibria . . . 40
  - A2 Generalized Collision Invariants (GCI) . . . 41
  - A3 Hydrodynamic limit $\varepsilon \to 0$ . . . 43
- Appendix B Large angular velocity . . . 44
  - B1 Determination of equilibria . . . 44
  - B2 Generalized collision invariants . . . 46
  - B3 Hydrodynamic limit $\varepsilon \to 0$ . . . 49
- Appendix C Small angular velocity limit of the SOHPR-L model . . . 52
  - C1 Proof of Proposition 2.5.3 . . . 52
  - C2 Proof of Proposition 2.5.1 . . . 54
- Appendix D Graphical representations . . . 55

Part II: The Vicsek model with repulsion 61

3 A macroscopic model for a system of self-propelled particles with alignment and repulsion 61
3.1 Introduction . . . 61
3.2 Model hierarchy and main results . . . 64
3.2.1 The individual based model and the mean field limit . . . 64
3.2.2 Scaling . . . 66
3.2.3 Hydrodynamic limit . . . 67
3.3 Numerical discretization of the SOHR model . . . 71
3.4 Numerical tests . . . 72
3.4.1 Convergence test . . . 73
3.4.2 Comparison between the SOHR and the Vicsek model with repulsion . . . 73
3.4.3 Comparison between the SOH and the SOHR model . . . 77
3.4.4 Comparison between the SOHR and the DLMP model . . . 77
3.5 Conclusion . . . 79
Appendix A Proof of formulas (3.2.21) and (3.2.22) . . . 79
Appendix B Proof of Theorem 3.2.1 . . . 80
Appendix C Proof of Proposition 3.3.1 . . . 81

4 Existence of solution for a system of repulsion and alignment 83
4.1 Introduction . . . 83
4.2 Existence theory in 2D . . . 85
4.2.1 Maximum principle and symmetrization . . . 85
4.2.2 Existence of approximating solution . . . 86
4.2.3 Estimation of the approximating solution . . . 86
4.3 Simulations . . . 90
4.4 Conclusion . . . 93

Part III: Experiments 99

5 Collective motion of self-propelled robots 99
5.1 Introduction . . . 99
5.2 Results . . . 100
5.3 Discussion . . . 102
5.4 Material and Methods . . . 103
5.4.1 Experimental setup and data processing . . . 103
5.4.2 Data analysis . . . 105
5.4.3 Clustering Method . . . 105
5.4.4 Simulation Model . . . 106

Conclusion 109

Chapter 1

General Introduction

1.1 Motivation

Collective motion can be observed everywhere and at every scales, from fish school, bird flock to bacteria, sperm cells as well as molecular motors in the cell. In spite of complexity of these systems, we see that there are some common features:

- Individuals have only local interaction,
- There is no leader inside these groups;
- The global organization of the groups is at much larger scale than the individual size

By this way these groups form coherent structures which can be seen as a result of the local interaction between the agents without intervenor of leader. One asks the following natural questions.

- How these individuals coordinate their behavior to form groups that move collectively?
- What are interaction rules between particles inside the groups?

One can answer these questions by experiment method. First, mathematical models are constructed by observing phenomena in the real life. Then the validity of these models will be tested by performing simulations or experiments. Two kinds of model are often used. Individual Based Model(IBM) focus on the evolution of each particle in time while continuous model describes the evolution of macroscopic quantities such as density or the mean velocity. In many works the IBMs have been used. Its advantage is able to test different hypotheses on the individual mechanism. However, the macroscopic models allow one to better understand and study the behavior of the systems at large scales. In order to benefit from both models, a solution is to derive the macroscopic models from the particle models. To do so, one can change time and space variables of the microscopic models, so that the dynamics of the individual based models are considered over long periods of time and lager distances. In order to establish a link between microscopic models and macroscopic models, we use an intermediate description, so-called mesoscopic models or mean-field kinetic models, where the state of the system is described by the probability distribution of a single particle. The IBMs, the kinetic models and the continuous models constitute a hierarchy of models in the sense that each level can be deduced from the previous one by a model reduction methodology. More precisely, kinetic models are deduced from IBMs by considering the probability distribution of a single particle while continuous model are reduced from kinetic model by taking averages over the velocity variable.

We focus on systems of dense suspensions of active particles. We refer to [63] for recent developments on the subject. Suspensions of active particles are fluid consisting of self-propelled particles

such as water including of bacteria, sperm cells, etc. When particles are highly concentrated, they may induce turbulences. A typical example of such fluid is sperm. The flow fluctuations induced by spermatozoa motion, that can be observed through a microscope, are known to be an excellent fertility criterion for the sample considered while the individual spermatozoa motility is not. This suggests the existence of a collective unknown effect which seems to have significant influence on the fertility of the sample.

The Seminal Motility Imaging and Modeling project (MOTIMO) has been recently created and supervised by the company IMV-Technologies. The goal of the MOTIMO project is to develop concepts which are necessary to the design of automated fertility tests of animal semen samples. My thesis, as a part of the MOTIMO project, results from a collaboration between several institutions: L'Institut de Mathématiques de Toulouse (IMT), l'Institut de Mécanique des Fluides de Toulouse (IMFT), l'Institut National de la Recherche Agronomique de Tours (INRA Tours), le Laboratoire d'Informatique, Signaux et Systèmes de Sophia-Antipolis (I3S) in Nice and transnational company, IMV-Technologies, the world leader in the reproduction biotechnologies. This manuscript will provide a better understanding in modelling of the collective mechanisms of dense suspension of active particles with a specific application concerning the so-called "massal motility" induced by the movement of spermatozoid in the semen.

1.2 Overview of the subject

This thesis aims to construct model hierarchies for active suspensions of particles including not only individual particles and their hydrodynamic interaction but also fluid. Many related works have been done, for example [81, 83, 84] to mention a few. However, most of these works deal with diluted suspensions of the active particles for which it is possible to develop a micro macro approach, wherein active particles are described by a distribution function satisfying an equation of Fokker-Planck, coupled with the Navier-Stokes equation for the fluid motion via the expression of the extra-constraint tensors [5, 9].

On the other hand, some experimental observations in raw ram sperm reveal that nearly 50% of the total volume of sperm is constituted of sperm cells, the remaining volume being filled with the seminal plasma. It is thus expected that sperm cells in raw ram sperm have extremely high concentration. In this situation, sperm cells are very close to each other and interactions via volume exclusion are certainly very important. The volume exclusion interaction has been considered by Peruani et al [75] where it was shown that the volume exclusion between elongated self-propelled particles results in alignment [5, 23, 58, 75]. Under these conditions, micro-macro approaches can be modified to account for these effects. One should also consider collective effects, the synchronization of beating flagella, which explain why spermatozoon individual motility is not well correlated with massal motility.

The first model of collective motion has been proposed by Aoki [3]. More recently, a simplified version of this model was introduced by Couzin et al [20]. These models (the so-called three zone model) in which the authors considered three types of interaction rules: long-range attraction, medium-range alignment and short-range repulsion to explain three different behaviors of particles: avoidance of being isolated, collective movement, avoidance of collisions, respectively. This model can be considered as a good compromise between physical accuracy and simplicity.

1.2.1 Pure alignment model: The Vicsek model and its variants

Microscopic model: The simplest model of collective motion that is based on the alignment interaction introduced by Vicsek [93] has attracted a lot of attention in the recent years. In this model, one merely assumes that individuals move at constant speed and update their direction so as to align with their neighbors up to a certain noise level. Alignment interaction can be classified into

polar and apolar alignment mechanisms. The polar interactions can be considered as ferromagnetic interaction (or F-alignment) where particles end up moving in the same direction. The apolar interaction causes effect similar to those in liquid-crystals at high density where particles get locally aligned. Degond and Motsch [29] (see the review [25]) have proposed a time continuous version of this model by replacing the time step Δt by collision frequency ν. Let $X_k(t) \in \mathbb{R}^n$ and $V_k(t) \in \mathbb{S}^{n-1}$ be the position and the velocity direction of the k-th particle at time t. The model is described by the following equations

$$\begin{aligned}
&\frac{dX_k}{dt} = cV_k,\\
&dV_k = P_{V_k^\perp} \circ (\nu \bar{V}_k dt + \sqrt{2D} dB_t^k)\\
&\bar{V}_k = \frac{\mathcal{J}_k}{|\mathcal{J}_k|}, \quad \mathcal{J}_k = \sum_{i,|X_i - X_k| \le R} V_i.
\end{aligned}$$

where, for $V \in \mathbb{S}^{n-1}$, $P_{V^\perp} = \mathrm{Id} \quad V \otimes V$ is the orthogonal projection onto the plan orthogonal to V. This projection insures that the resulting solution $V_k(t)$ stays on the unit sphere. Finally dB_t denotes the Brownian motion with intensity $\sqrt{2D}$.

In spite of its simplicity, this model is able to exhibit complex phase transitions from disordered to order states when the noise decreases or when the density increases (see e.g. [2, 16, 27, 52, 93]). We refer to [94] for a recent survey on this study. The phase transition is studied through the order parameter which is defined by

$$\varphi = \frac{1}{N}\Big|\sum_{i=1}^{N} V_i\Big| \tag{1.2.1}$$

This parameter measures the global alignment of particles, which tends to 1 as the motion is order and which is close to 0 as the motion is disordered. In [93], the authors showed that the Vicsek model exhibits a second order phase transition which results in a continuous change of the order parameter. By contrast, phase transition is of first-order during which, by definition, the order parameter jumps from one value to another.

Variants of the Vicsek model:

- In [52], the authors changed the way in which the noise is introduced. More precisely, "vectorial noise" is added to J_k instead of angle in the original model.
- The Cucker-Smale model [21] assumes that particles tend to align their speed with the speed of their neighbors and does not impose any constraint on the particle speed. Denote by $(X_k(t), V_k(t))$ the position and the velocity of the k-particle at time t. The state of this system is described by the following equations

$$\begin{aligned}
&\frac{dX_k}{dt} = V_k,\\
&\frac{dV_k}{dt} = \alpha \sum_{i=1}^{N} \varphi_{ik}(V_i - V_k)
\end{aligned}$$

  where α is constant and the functions φ_{ik} quantify the way the particles influence each other. It is assumed that the influence only depend on the distance between the particles i.e $\varphi_{ik} = \varphi(|X_i - X_k|)$. When φ decays sufficiently slowly, one can observe flocking behavior. This model has triggered considerable mathematical activity [15, 55, 56, 72].
- Frouvelle [43] proposed a variant of the time continuous version by assuming the parameter ν depending on the density and introducing an anisotropy in the kernel of observation. In [24], the authors assume that ν is proportional to the absolute value of the mean momentum of

the neighbors $|J_i|$. This assumption allows one to get a macroscopic phase transition. Under this assumption, the continuous time version is very close to the discrete one.

Mean-field model: From the continuous time version of the Vicsek model, a mean-field model is obtained by letting the number of particles $N \to \infty$. The kinetic model can be described by the one-particle distribution $f(x, v, t)$ where (x, v) is the position in the phase space $\mathbb{R}^n \times \mathbb{S}^{n-1}$. The evolution equation for f is given by the following Fokker-Planck equation:

$$\partial_t f + c\nabla_x \cdot (vf) = \nabla_v \cdot (F_f f) + D\Delta_v f. \tag{1.2.2}$$

$$F_f(x, v, W, t) = P_{v^\perp}(\nu \bar{v}_f(x, t)), \ \bar{v}_f(x, t) = \frac{\mathcal{J}_f(x, t)}{|\mathcal{J}_f(x, t)|} \tag{1.2.3}$$

$$\mathcal{J}_f(x, t) = \int_{(y,v)\in\mathbb{R}^n\times\mathbb{S}^{n-1}} K\Big(\frac{|x-y|}{R}\Big) f(y, v, t)\, v\, dy\, dv \tag{1.2.4}$$

where $\nabla_v \cdot, \Delta_v$ stand for the divergence and the Laplace-Beltrami operators on the sphere. The kernel K depends on the distance between the particle and its neighbors $|x - y|$ within the range with radius R.

Kinetic models have been proposed for some variants of the Vicsek model (e.g. [12, 13, 15]). In [14], the authors proved that the kinetic Cucker-Smale model converges to the kinetic Vicsek model. Peruani et al [76] have proposed a mean-field approach for self-propelled particles which interact through ferromagnetic and liquid-crystal alignment mechanisms.

Macroscopic model: Many macroscopic models have been proposed for the Vicsek model [9, 29, 90]. However, most of them are based on the phenomenological method and closure moment [9, 79, 90, 91]. The first rigorous derivation of hydrodynamic model from kinetic one of the Vicsek model has been proposed by Degond and Motsch [29] (see [21] for a survey). This model is called Self-Organized Hydrodynamic (**SOH**) model . The main contribution of this work is to introduce a new concept "Generalized Invariant Collision" which allows one to derive hydrodynamic models despite a lack of momentum conservation. The lack of conservations is acknowledged (see e.g the discussion in the introduction of [94]) as one of the essential differences between collective phenomena in standard statistical physics and biology.

The SOH model describes the evolution of the density ρ and the mean direction Ω, given by

$$\partial_t \rho + \nabla_x \cdot (c_1 \rho \Omega) = 0,$$
$$\rho\, \partial_t \Omega + c_2\, \rho\, (\Omega \cdot \nabla_x)\Omega + d\, P_{\Omega^\perp} \nabla_x \rho - \gamma\, P_{\Omega^\perp} \Delta_x (\rho\Omega)$$

where the coefficients c_1, c_2, γ, d satisfy $c_1 > c_2$, $d > 0$ and $\gamma \geq 0$. This model consists first of a conservative equation of mass, second of an evolution equation for the mean direction Ω. The two equations are supplemented by a geometric constraint $|\Omega| = 1$. The SOH model is not Galilean-invariant because of this constraint. Simulations of the SOH model without diffusion term have been performed to validate the SOH model [71]. Furthermore, several works on the SOH model have been investigated as existence of solution [32]. Phase transitions have been analyzed [4, 24, 27, 44].

1.2.2 Pure attraction-repulsion models

Microscopic - Macroscopic models: In contrast to the Vicsek model, many other models consider only short range interaction and long range attraction of particles [19, 37, 69]. Within these frame works, a force field is introduced which allows particles push or attract together. The attractive-repulsive force are described through a Morse type of potential. The long-range attraction accounts for how social groups form. The short range repulsion is motivated from the fact that the finite size particles can not overlap and repel each other when they are too close.

So, there exists a maximum value that the particle density can not pass. This maximum value of density comes from volume exclusion interaction which is referred to as a congestion constraint. The congestion phenomena also occurs in vehicular traffic [8]. The first work dealing with simultaneous self-propulsion and volume exclusion interactions was published by Peruani et al [75]. Volume exclusion can result in apolar alignment [75] as well as polar alignment [53]. In [87, 58], the authors took care of the emergence of collective motion of observed from experiments with bacteria as a consequence of direct cell-to-cell interactions which are modelled by a short-range attractive-repulsive inter-cellular forces.

In [49], a model describing the movement of elongated self-propelled particles under the influence of nematic collision and of noise was introduced. Consider two particles and let α be the included angle of their velocity vectors at some time before impingement. Then nematic collision means that if α is smaller than 180°, the particles will move in the same direction after collision and if α is bigger than 180° they will move in the opposite direction. However, this interaction rule can also be regarded as resulting from volume exclusion and alignment.

1.2.3 Combined alignment and attraction-repulsion models

Microscopic model: We are interested in modelling of collective motion in large systems of self-propelled particles through medium-range alignment and short-range repulsion. As mentioned above, the three zones model is the first model of collective motion which accounts for three different rules of interaction: alignment, attraction and repulsion. Some variants of this model have been proposed in [57, 68]. These models are used to describe the motion of fish. Degond et al have also proposed [32] a variant of this model by adding a pairwise attractive-repulsive force to the time continuous version of the Vicsek model. In [51], a Lennard-Jones type force was added into the Vicsek model to take into account simultaneously collective and cohesion motion.

With reflecting boundary condition, the Vicsek model represents an accumulation of particles swimming along the boundary. In order to avoid this effect, a repulsion is added into the Vicsek model [23]. It was observed that reflecting boundary breaks the large-scale order and that domains of ordered particles are separated by slip lines, in a similar fashion as wall domain in spin systems. It is also observed that the Vicsek model with repulsion exhibit symmetry breaking in an annular domain with reflecting boundaries: after some time, all particles choose to swim in one direction, either clockwise or anti-clockwise.

Macroscopic model: One method to account for both alignment and repulsion interactions is to consider the SOH model with the congestion constraint. As mentioned above, in the congestion case, the density of individuals cannot exceed a maximal density threshold at which they are in contact with each other. To analyse this problem, in [28, 33] the authors consider a singular pressure when the density ρ approaches the congestion density ρ^*. This model is used to describe the congestion phenomena of animal living in group such as sheep.

In chapter 2, we will build up a model hierarchy for active suspensions of particles from the microscopic model to the macroscopic model based on alignment and volume exclusion. In [77], volume exclusion effects are presented via lattice nodes: nodes can be occupied at most by one particle. In our model, steric interaction is modelled by a repulsive force.

1.2.4 Synchronization and combined alignment and synchronization models

Microscopic model: The Kuramoto model [65] describes synchronization which is observed in biological, chemical, physical, and social systems. A paradigmatic example illustrating synchronization is the synchronous flashing of fireflies observed in some South Asian forests. This model has found widespread applications such as in neuroscience. It consists of N-oscillators $\theta_i(t)$ having

intrinsic frequencies ω_i distributed with a given probability density $g(\omega)$. Oscillators are related to all other oscillators through the sine of their difference. Their dynamics are described by the following equation

$$\dot{\theta}_i(t) = \omega_i - \frac{K}{N}\sum_{j=1}^{N}\sin(\theta_j - \theta_i), \quad i = 1, \cdots, N.$$

When the coupling is large enough, collective synchronization emerges spontaneously. In spite of simplicity, this model can display a large variety synchronization patterns. Several variants of the Kuramoto model have been proposed such as the Kuramoto model with noise, short-range model, models with disorder, models with external fields. These variant models and their applications have been discussed in [1] Some works have acknowledged the proximity between the Kuramoto and Vicsek models, such as [18, 54].

Mean-field model: Mean-field models have been proposed for the Kurammoto model and with noise. More studies on the Kuramoto model have been done in [1, 10, 11, 47, 48, 67].

In chapter 1, we introduce a model which combines the Vicsek model and the Kuramoto model. It borrows from the Kuramoto model the way the agents synchronize the phase of their rotation and from the Vicsek model the way this synchronization is coupled with the spatial localization of the agents. The goal of this work is to derive hydrodynamic models for this model and to study some properties of the hydrodynamic models obtained.

1.2.5 Models and experiments

As mentioned above, studying interaction rules between particles inside systems plays an important role to understanding collective phenomena. Many works have explored interaction rules between particles from the observation of global dynamics Several models have been built from experiment data. For examples, the so-called "Persistent Turner" model has been built step by step from experiment data of fish [45]. Some projects have been built to study collective behavior based on experiment data such as the PEDIGREE project (PEDestrIan GRoups : EmErgence of collective behaviour through experiments, modelling and simulation) or the PANURGE project (Study of gregariousness in vertebrate species).

In order to investigate if elongated self-propelled particles undergoing volume exclusion interactions may exhibit emergent phenomena, we have performed experiments with a model system consisting of simple self-propelled robots. Experiments consist of placing the hexabugs in a ring and the video tracking of the bugs and the calibration of the models against these data. There already exists some works based on robots such as the work of TaylorKing et al on E-Puck robots [89]. Some microscopic models have been proposed to describe the motion of robots such as the model of Sugawara et al [86].

1.3 Presentation of main results

1.3.1 Chapter 1: The Vicsek - Kuramoto model

In this chapter, we introduce a new model for large system of rotating self-propelled particles subject to alignment interaction. This model combines the Kuramoto and Vicsek dynamics. We denote by $(X_k(t), V_k(t), W_k)_{k=1\cdots N}$ the positions, the normalized velocities and the proper angular velocities of the particles, respectively, with $X_k(t) \in \mathbb{R}^2$, $V_k(t) \in \mathbb{S}^2$ and $W_k \in \mathbb{R}$. The particles move at constant speed c. The dynamical system satisfies the following stochastic differential equations:

$$\begin{aligned} \frac{dX_k}{dt} &= cV_k, \\ dV_k &= P_{V_k^\perp} \circ (\nu \bar{V}_k dt + \sqrt{2D} dB_t) + W_k V_k^\perp dt. \end{aligned}$$

where $P_{V_k^\perp} = Id - V_k \otimes V_k$, the quantity dB_t refers to the standard white noise in $\mathbb{R}^2$ with intensity $\sqrt{2D}$, $V_k^\perp$ denote the vector obtained from V_k by a rotation a angle $\pi/2$. The quantity ν refers to the relaxation constant of the velocity of one particle towards the neighbors' average velocity $\bar{V}_k$. The average direction around the particle $X_k(t)$ with radius R is defined by

$$\bar{V}_k = \frac{\mathcal{J}_k}{|\mathcal{J}_t|}, \quad \mathcal{J}_k = \sum_{j, |X_j - X_k| \le R} V_j.$$

After scaling, the kinetic equations are then given by

$$\partial_t f^\varepsilon + \nabla_x \cdot (v f^\varepsilon) = \frac{1}{\varepsilon}\Big(\nabla_v \cdot (P_{v^\perp} \Omega_{f^\varepsilon} f^\varepsilon) + d\Delta_v f^\varepsilon \Big) - \frac{1}{\eta} W \nabla_v \cdot (v^- f^\varepsilon),$$

$$\Omega_f(x,t) = \frac{J_f(x,t)}{|J_f(x,t)|}, \quad J_f(x,t) = \int_{(v,W)\in \mathbb{S}^1 \times \mathbb{R}} f(x,v,W,t)\, v\, dv\, dW.$$

Two regimes will be investigated following two scaling assumptions on η :

(i) Small angular velocities: $\eta = \mathcal{O}(1)$. In this regime, the equilibrium of the system is still a Von-Mises-Fisher distribution function. Taking the limit $\varepsilon \to 0$, we obtain an equation for the density $\rho_W(x,t)$ and the velocity director $\Omega(x,t)$ as follows:

$$\partial_t \rho_W + \nabla_x \cdot (c_1 \rho_W \Omega) = 0, \quad \forall W \in \mathbb{R},$$
$$\rho\left(\partial_t \Omega + c_2 (\Omega \cdot \nabla_\perp)\Omega - Y \Omega^\perp\right) + d P_{\Omega^\perp} \nabla_x \rho = 0,$$
$$\rho(x,t) = \int_{W\in\mathbb{R}} \rho_W(x,t)\, dW, \qquad (\rho Y)(x,t) = \int_{W\in\mathbb{R}} \rho_W(x,t)\, W\, dW.$$

(ii) Large angular velocities: $\eta = \mathcal{O}(\varepsilon)$. This changes significantly the equilibrium velocity distribution of the particles. In order to preserve the particle propensity to locally align with their neighbors, we are led to modify the interaction force. Then the density $\rho_W(x,t)$ and the mean direction $\Omega(x,t)$ satisfy the following system of hydrodynamic equations:

$$\partial_t \rho_W + \nabla_x \cdot (c_1 \rho_W \Omega) = 0, \quad \forall W \in \mathbb{R},$$
$$m_1[\rho_W]\,\Omega_t - m_2[\rho_W]\,(\Omega \cdot \nabla_x)\Omega - m_3[\rho_W]\,(\Omega^\perp \cdot \nabla_x)\Omega$$
$$-\Omega^\perp\left(m_4[\rho_W](\nabla_x \cdot \Omega) + (\Omega^\perp \cdot \nabla_x)\, m_5[\rho_W] + (\Omega \cdot \nabla_x)\, m_6[\rho_W]\right) = 0,$$

where $m_1[\rho_W], \ldots, m_6[\rho_W]$ are moments of ρ_W. Some properties of this model are investigated as the linearized stability in some particular cases and the asymptotics when the proper rotation is small. We show that this hydrodynamic model is reduced to the SOH model in this limit but with different coefficients.

1.3.2 Chapter 2: The Vicsek model with repulsion

In this chapter we introduce a new model to describe the movement of elongated self-propelled particles like bacteria, sperm cells in large systems. We consider a system of N-particles which interact through volume exclusion interaction and alignment. Let $X_k(t)$ denote the position of k-particle at time t, and $v_k(t), \omega_k(t)$ denote the velocity and the orientation, respectively. Volume exclusion interactions are modelled by a repulsive force which is defined through a repulsive potential ϕ with mobility μ. The particle orientations relax towards the neighbors' average orientation $\bar{\omega}_k$ with relaxation constant ν. The dynamics are described by the following equations

$$\begin{aligned}
\frac{dX_k}{dt} &= v_k, \\
v_k &= v_0 \omega_k - \mu\Big(\frac{1}{N}\sum_{i=1}^{N} \nabla\phi(|X_i - X_i|)\Big), \\
d\omega_k &= P_{\omega_k^\perp} \circ (\nu \bar{\omega}_k dt + \alpha \omega_k dt + \sqrt{2D} dB_t).
\end{aligned}$$

where the projection $P_{\omega^\perp} = (\mathrm{Id} \quad \omega \otimes \omega)$ insures that the orientation of each particle remains on the unit sphere. The parameter α represents the relaxation rate of the orientation ω_k towards the velocity V_k. v_0 is the constant self-propulsion speed of particles. B_t is the Brownian motion with intensity $\sqrt{2}\bar{D}$. The mean orientation $\bar{\omega}_k$ is defined by

$$\bar{\omega}_k = \frac{\mathcal{J}_k}{|\mathcal{J}_k|}, \quad \mathcal{J}_k = \sum_{i=1}^{N} K(|X_i - X_k|)\omega_i.$$

where the kernel K measures how the orientation of one particle is influenced by its neighbors.

The mean-field equation with hydrodynamic scaling reads

$$\varepsilon\Big(\partial_t f^\varepsilon + \nabla_x \cdot (v^\varepsilon_{f^\varepsilon} f^\varepsilon) + \alpha \nabla_\omega \cdot (P_{\omega^\perp} v^\varepsilon_{f^\varepsilon} f^\varepsilon) + \nabla_\omega \cdot (P_{\omega^\perp} G^1_{f^\varepsilon} f^\varepsilon)\Big) = \mathcal{Q}(f^\varepsilon),$$

$$v^\varepsilon_{f^\varepsilon}(x,\omega,t) = v_0\omega \quad \mu\Phi_0 \nabla_x \rho_{f^\varepsilon}, \quad G^1_{f^\varepsilon}(x,t) = \frac{k_0}{|J_{f^\varepsilon}|} P_{\omega^\perp} \Delta_x J_{f^\varepsilon},$$

where the coefficients Φ_0, k_0 come from the kernels ϕ, K, and the collision operator $\mathcal{Q}(f)$ is given by

$$\mathcal{Q}(f) = \nabla_\omega \cdot (\cdot \; P_{\omega^\perp} \Omega_f f) + d\Delta_\omega f.$$

The local density ρ_f, the local current density J_f and local average orientation Ω_f are defined by

$$\rho_f(x,t) = \int_{\mathbb{S}^{n-1}} f(x,w,t)dw,$$

$$J_f(x,t) = \int_{\omega \in \mathbb{S}^{n-1}} f(x,w,t)\omega d\omega,$$

$$\Omega_f(x,t) = \frac{J_f(x,t)}{|J_f(x,t)|}.$$

Due to the concept of GCI, the rigorous derivation of hydrodynamic model is possible. The evolution of density $\rho(x,t)$ and the mean orientation $\Omega(x,t)$ satisfy the following equations

$$\partial_t \rho + \nabla_x \quad (\rho U) = 0,$$
$$\rho\partial_t \Omega + \rho(V \cdot \nabla_x)\Omega + P_{\Omega^\perp} \nabla_x p(\rho) - \gamma P_{\Omega^\perp} \Delta_x(\rho\Omega),$$
$$|\Omega| = 1,$$

where

$$U = c_1 v_0 \Omega - \mu\Phi_0 \nabla_x \rho, \quad V = c_2 v_0 \Omega - \mu\Phi_0 \nabla_x \rho,$$

$$p(\rho) = v_0 d\rho + \alpha\mu\Phi_0\big((n \quad 1)d - c_2\big)\frac{\rho^2}{2}, \quad \gamma = k_0\big((n-1)d + c_2\big).$$

and c_1, c_2 are constants depending on d. This model is called the " Self-Organized Hydrodynamics with Repulsion" (SOHR). Numerical simulations have been performed for two purposes. The first one is to validate the SOHR model by comparison to those of the particle model. The second one is to highlight the difference between the SOH model and the SOHR model.

1.3.3 Chapter 3: The existence of solution of the SOHR model: comparison between theory and simulations

In this chapter, we study the existence of solution of the following system in two dimensions:

$$\partial_t \rho + \beta_1 \nabla_x \cdot (\rho\Omega) - \beta_2 \Delta(\frac{\rho^2}{2}) = 0,$$
$$\rho\partial_t \Omega + \beta_3 \rho(\Omega \cdot \nabla_x)\Omega \quad \beta_4 \rho(\nabla\rho \cdot \nabla_x)\Omega + P_{\Omega^\perp} \nabla_x p(\rho) - \gamma P_{\Omega^\perp} \Delta_x(\rho\Omega)$$
$$|\Omega| = 1,$$

where $p(\rho) = c_1\rho + c_2\rho^2/2$ and the constants $\beta_1, \cdots, \beta_4, \gamma, c_1, c_2$ are non-negative. By using the method in '88 and the techniques to estimate the solution in [32], we obtain the following theorem

Theorem 1.3.1. *We assume that the initial data belong to $H^m(\Pi^2)$ with $m > 2$. Then there exists a time $T > 0$ and a unique solution (ρ, ψ) in $L^\infty([0,T]; H^m(\Pi^2)) \cap H^1([0,T]; H^{m-2}(\Pi^2))$ such that ρ is positive. Moreover, if the coefficients $\beta_2, \gamma > 0$ then the solution also belongs to $L^2([0,T]; H^{m+1}(\Pi^2)) \cap H^1([0,T], H^{m-1}(\Pi^2))$.*

On the other hand, by simulations, we show that the term $\beta_4\rho(\nabla\rho \cdot \nabla_x)\Omega$ plays a role of an unstable term. When we change of β_4 by a small quantity, the stability of the system will be changed. As β_4 exceeds all of the coefficients $\beta_2, \gamma, c_1, c_2$, the numerical solution exists only for short time. The solution will become regular if one of the coefficients $\beta_2, \gamma, c_1, c_2$ are large enough. Therefore, the existence of numerical solution depends on the relation between the coefficients.

1.3.4 Chapter 4: Experiments

This chapter is devoted to investigate experimentally collective behavior in systems of elongated self-propelled particles which interact through volume-exclusion interactions. For this purpose, we performed experiments with simple self-propelled robots. A system consisting of 80 Hexbug (see fig 5.9) was used. Experiments were conducted with 2, 5, 10, 15, 20, 30 bugs in confined ring shaped arenas. We observe a new organisation of motion where the particles align orthogonally at the boundary of the ring to form drifted clusters.

Figure 1.1: A self-propelled robot of the brand Hexbug: a small battery-powered electric engine triggers the vibration of the device. The bended plastic legs offer differential friction with the substrate. As a result, the device moves ahead. Due to unbalanced bending, most of these devices move along circles of various radii.

To study this phenomena of the bugs, we measure some characteristics for clusters as cluster size and cluster lifetime. This study provides some statistical measures to validate a model between bugs. We also constructed a model which is able to reproduce qualitatively this behavior. We consider a system of N-rod particles. Each rod particle consists of n-beads with its radius r_b and its mass m_b. Let $X_i(t) \subset \mathbb{R}^2$ denote the centre position of i-rod at time t, and $v_i(t), \omega_i(t), \Omega_i(t)$ denote the velocity and the orientation and the angular velocity, respectively. The position of the j-th bead of the i-th rod X_{ij} is computed by the following formula:

$$X_{ij} = X_i + \omega_i\Big[\big(-(n-1) + 2(j-1)\big)r_b\Big].$$

The dynamics are described by the following equations:

$$\frac{dX_i}{dt} = v_i,$$
$$m\frac{dv_i}{dt} = \lambda(v_0\omega_i - v_i) + F_i, \quad I_i\frac{d\Omega_i}{dt} = \tau_i, \quad \beta\Omega_i I_i.$$

where the mass of the rod m is equal nm_b. The repulsive force F_i acts on each rod given by

$$F_i = \sum_{j=1}^{n} \sum_{\substack{k=1,N \\ l=1,n}} F_{ijkl}$$

where $F_{ijkl} = F(X_{ij} - X_{kl})$ is the repulsive force between the j-th bead of the i-th rod and the the l-th bead of the k-th rod, given by

$$F(x) = \begin{cases} F_0 \frac{x}{|x|}(1 - \frac{|x|}{r}) \text{ if } |x| < r \\ 0 \quad \text{otherwises.} \end{cases} \tag{1.3.5}$$

The coefficients λ, F_0 represent the intensities of self-propulsive and repulsive force, respectively. The torque τ_i and the moment of inertia I_i are given by

$$\tau_i = \sum_{j=1}^{n} \left((X_{ij} - X_i) \times \sum_{\substack{k=1,N \\ l=1,n}} F_{ijkl} \right)$$

$$I_i = \sum_{j=1}^{n} |X_{ij} - X_i|^2 m_b.$$

Part I: The Vicsek-Kuramoto model

Chapter 2

Hydrodynamics of the Kuramoto-Vicsek model of rotating self-propelled particles

This chapter has given an article in collaboration with P. Degond and G. Dimarco and published in the Journal of Mathematical Models and Methods in Applied Sciences: Hydrodynamics of the Kuramoto-Vicsek model of rotating self-propelled particles, M3AS, (2014).

2.1 Introduction

This chapter is concerned with the study of large system of rotating self-propelled particles subject to collective 'social' interactions. Specifically, we consider particles evolving in the plane under the following influences. (i) self-propulsion, (ii) proper rotation, (iii) 'social interaction' resulting in velocity alignment with their neighbors' average velocity and (iv) random velocity fluctuations in the form of Brownian motions in the velocity direction. Proper rotation means that the self-propelled particle trajectories, in the absence of any other influence (i.e. without (iii) or (iv)) are circles of constant centers and radii. Moreover, the centers and radii of different particles can be different. The goal of the present work is to establish a set of hydrodynamic equations for the density and mean-velocity of these particles. Such hydrodynamic equations will be valid at large time and space scales compared with the typical interaction time and distance between the particles.

Systems of self propelled particles interacting through local alignment have received considerable interest since the early work of Vicsek and coauthors [93]. This is because despite its simplicity, this paradigm is able to reproduce many of the collective patterns observed in nature. It also exhibits complex behaviors such as phase transitions which have motivated a huge literature [2, 16, 27, 52, 93]. We refer to [94] for a recent review on the subject. But in the vast majority of previous works, the influence of proper rotation (see item (ii) above) has been ignored.

Furthermore, a majority of works on such systems use Individual-Based Models (IBM) which consist in following the evolution of each particle (or individual, or agent) in time [15, 16, 19, 21, 55, 69, 72]. These models aim at describing systems of swarming biological agents such as animals living in groups [3, 20, 46] or bacterial colonies [22] among others. Alignment interaction has also been shown to result from volume exclusion interaction in the case of elongated self-propelled particles [6, 75].

When the number of agents is large, it is legitimate to consider mean-field kinetic models, [7, 9, 13, 42, 56] where the state of the system is described by the probability distribution of a single particle. It is even possible to reduce the description further by considering hydrodynamic models.

which follow the evolution of average quantities such as the local density or average velocity. Until recently, hydrodynamic models of interacting self-propelled particle systems were mostly derived on phenomenological considerations [5, 9, 79, 90, 91]. A series of works [29, 32, 43] have firmly established the derivation of such hydrodynamic models from microscopic ones, and particularly of one of them, the 'Self-Organized Hydrodynamics' (SOH) (see the review [25]). Within this framework, phase transitions have been analyzed [4, 24, 27, 44] (see also the review [26]). We wish to follow the same methodology here and derive hydrodynamic models of **rotating** self-propelled particles interacting through local alignment. This work is focused on model derivation. So, we defer the analysis of phase transitions to future work.

Situations where swarming agents are trapped in a rotation motion are not uncommon. A typical example is given by swimming agents such as bacteria or algae in a shear flow. In the case of elongated particles, the velocity shear induces a rotation of the particles in a motion named Jeffrey's orbits [62]. The combination of this effect with swimming leads bacteria to undergo a circular motion near boundaries [38, 66]. This nurtures the so-called gyrotactic effect which is responsible for accumulation of phytoplankton in layers [39] and patches [40]. Staying in the biological realm, we note that some strains of swarming bacteria exhibit circular motion and vortex formation [22]. In some circumstances, coordination of flagella beats leads sperm cells to self-organize in a collective formation of vortices [80]. In a different context, roboticists are keen to find decentralized control algorithms of robot swarms inducing a collective circular motion of the swarm [17, 73, 85]. Applications target the design of mobile sensor networks for mapping or monitoring.

The goal of this chapter is to provide a continuum description of these systems when the number of agents is large. We start by proposing an IBM which encompasses features (i) to (iv) above. This IBM combines the Kuramoto [65] and Vicsek [93] dynamics (see [1] and [94] for reviews on the Kuramoto and Vicsek models respectively). It borrows from the Kuramoto model the way the agents synchronize the phase of their rotation and from the Vicsek model the way this synchronization is coupled with the spatial localization of the agents. Indeed, agents look for neighbors, compute the average phase of their rotation motion and choose this phase as their target for their own phase. In the absence of proper rotation of the particles, one recovers exactly the Vicsek model in its time continuous form [22, 29] By contrast, if the synchronization is global, i.e. the agents compute the average phase over the whole ensemble of particles, the original Kuramoto model is recovered. Previous works have acknowledged the proximity between the Kuramoto and Vicsek models [18, 54]. The present model is close to that proposed in [73, 85]. A different, but related approach where the oscillators move diffusively in space, has been studied in [78]. But none of them have proposed a hydrodynamic description of a system of particles undergoing a combined Kuramoto-Vicsek dynamics. This is the goal pursued here.

Similar to the present work, previous works have used circular motion as the free motion of the agents. In particular, the so-called 'Persistent Turner' model has been proposed to describe the dynamics of fish [30, 45] and fish schools [31, 46] However, there are significant differences. In the 'Persistent Turner' model, the curvature of the motion undergoes stochastic changes. In the mean over time, the curvature is zero, and there is no preferred turning direction. By contrast, in the present work, the curvature is constant and so is its mean over time. Consequently, there is a definite preferred turning direction. These differences are significant and can be read on the structure of the resulting hydrodynamic models.

After writing the combined Kuramoto-Vicsek IBM, we propose a mean-field kinetic description of this system by means of a Fokker-Planck type equation for the one-particle ensemble distribution function. After scaling the kinetic equation to dimensionless variables, we realize that two regimes are of interest. In the first one, the proper rotation of the particles is slow enough, so that the particles can reach an equilibrium under the combined influences of the alignment and noise without deviating from a straight line too much. In this regime, the hydrodynamic limit yields the SOH model [25, 29, 32, 43] with an additional source term in the velocity evolution equation stemming from the average proper rotation of the particle ensemble. This regime is called the slow angular velocity regime and the associated hydrodynamic models, the **'Self-Organized Hydrodynamics**

with Proper Rotation (Small angular velocity case)' or SOHPR-S .

Another regime is possible, where the proper rotation is of the same order as the alignment interaction and noise. This changes significantly the equilibrium velocity distribution of the particles. In order to maintain the propensity of the particles to align with the ensemble of neighboring particles, we are led to modify the definition of the direction to which elementary particles align. This modification is commented in great length in the corresponding section below. At this point, let us simply mention that this modification could account for the influence of volume exclusion interaction in the spirit of [6, 75]. In this regime, the obtained hydrodynamic model involves significant modifications compared with the previous SOH model and is called the **'Self-Organized Hydrodynamics with Proper Rotation (Large angular velocity case)' or SOHPR-L**

The changes compared with the previous SOH model consist of two aspects. First, the velocity equation is coupled to the whole angular velocity distribution function (and not through simple moments such as the density or average angular momentum, by contrast with the SOHPR-S model). Second, this equation involves additional terms which correspond to transport in the direction normal to the velocity, or off-diagonal terms in the pressure tensor. In spite of its complexity, the model is shown to be linearly well-posed when the angular velocity distribution function is an even function (i.e. there is no preferred turning direction when averaged over the particles). Also, the asymptotics for small angular velocities reduces the complexity of the system to that of three first order partial differential equations. More detailed analytical studies of this system are in progress.

In both regimes, the derivation of hydrodynamic models is possible, in spite of the lack of momentum conservation. The lack of conservations is acknowledged (see e.g. the discussion in the introduction of [94]) as one of the major differences and sources of analytical difficulties that complex systems in biology and social sciences present. The main contribution of previous works on the SOH model (see e.g. the review [25]) has been to provide a way to bypass this lack of momentum conservation. The main tool for this is the concept of Generalized Collision Invariant (GCI). Again, this concept will be the key of the derivation of the SOHPR models, in both the small and the large angular velocity cases.

The paper is organized as follows. In section 2.2, the IBM and its mean-field kinetic limit are introduced and scaling considerations are developed. Section 2.3 is devoted to the statement of the convergence of the mean-field kinetic model towards the hydrodynamic limit in the small angular velocity case. Some properties of the SOHPR-S model are discussed. The case of the large angular velocity regime is then treated in section 2.4. Section 2.5 details some of the properties of the SOHPR-L model, such as its linearized stability or its asymptotics in the small angular velocity limit. A conclusion is drawn in section 2.6. Then, three appendices are devoted to the proofs of the formal convergence results towards the hydrodynamic limit in the small angular velocity case (Appendix A) and in the large angular velocity case (Appendix B) and to the formal asymptotics of the SOHPR-L model when the angular velocities become small (Appendix C). Finally Appendix D presents some graphical illustrations.

2.2 Individual-Based model, mean-field limit and scaling

We consider a system of N particles or agents moving with constant speed c in the two-dimensional plane $\mathbb{R}^2$. We denote by $(X_k(t), V_k(t))_{k=1,\dots,N}$ the positions and the normalized velocities of the particles, with $X_k(t) \in \mathbb{R}^2$ and $V_k(t) \subset \mathbb{S}^1$, where $\mathbb{S}^1$ denotes the unit circle in $\mathbb{R}^2$. The actual velocities of the particles are $\bar{V}_k = cV_k$. Each particle is subject to three different actions. The first one is a proper angular velocity W_k, which, in the absence of any other action, would result in a circular motion of radius $R_k = \frac{c}{|W_k|}$, rotating counter-clockwise if $W_k > 0$ and clockwise if $W_k < 0$. Then, each particle is subject to independent Brownian white noises $P_{V_k^\perp} \circ (\sqrt{2D}\, dB_t^k)$ with uniform diffusivity D. The quantity dB_t^k refers to the standard white noise in $\mathbb{R}^2$. It is projected onto a standard white noise on $\mathbb{S}^1$ thanks to the projection operator $P_{V_k^\perp}$. Denoting by $V_k^\perp$ the vector obtained from V_k by a rotation of angle $\pi/2$, $P_{V_k^\perp}$ is the orthogonal projection onto the

line generated by V_k^-, i.e. $P_{V_k^\perp} = V_k^\perp \otimes V_k^\perp = \mathrm{Id} - V_k \otimes V_k$, where $\otimes$ denotes the tensor product of two vectors and Id is the identity matrix. The symbol '$\circ$' indicates that the corresponding stochastic differential equation is taken in the Stratonovich sense. The fact that the projection of a standard white noise in $\mathbb{R}^2$ onto the tangent line to the circle in the Stratonovich sense leads to a standard white noise on $\mathbb{S}^1$ can be found e.g. in [61]. Finally, the particle velocities relax towards the neighbors' average velocity $\bar{V}_k$ with relaxation constant ν. The quantity ν is also supposed uniform (i.e. all particles have identical ν) and constant in time for simplicity. Following these rules, the particles evolve according to the following stochastic differential equations:

$$\frac{dX_k}{dt} = cV_k, \tag{2.2.1}$$

$$dV_k = P_{V_k^\perp} \circ (\nu \bar{V}_k\, dt + \sqrt{2D}\, dB_t) + W_k V_k^\perp\, dt. \tag{2.2.2}$$

The vector $\bar{V}_k$ may be computed by different rules, leading to different types of models. For the time being, we assume that $\bar{V}_k$ is obtained by normalizing the average $\mathcal{J}_k$ of the velocities V_j of the particles j lying in a disk of given radius R centered at X_k, i.e.

$$\bar{V}_k = \frac{\mathcal{J}_k}{|\mathcal{J}_k|}, \quad \mathcal{J}_k = \frac{1}{N} \sum_{j,\,|X_j - X_k| \le R} V_j. \tag{2.2.3}$$

In the absence of self-rotation velocity ($W_k = 0$), the system reduces to the time-continuous version of the Vicsek alignment model [93] as proposed in [22, 29]. On the other hand, if the neighbor's average velocity is computed over all the particles, i.e. if (2.2.3) is replaced by

$$\bar{V}_k = \bar{V} = \frac{\mathcal{J}}{|\mathcal{J}|}, \quad \mathcal{J} = \frac{1}{N} \sum_{j=1}^{N} V_j, \tag{2.2.4}$$

then, the evolution of the velocities $(V_k)_{k=1,\dots,N}$ does not depend on the positions $(X_k)_{k=1,\dots,N}$ and the resulting system for $(V_k)_{k=1,\dots,N}$ is nothing but the noisy Kuramoto model of oscillator synchronization [1]. Indeed, considering the noiseless case $D = 0$ for simplicity, we can write $V_k = (\cos\theta_k, \sin\theta_k)$, $\bar{V} = (\cos\bar{\theta}, \sin\bar{\theta})$ and Eq. (2.2.2) with (2.2.4) can be written:

$$\begin{aligned} \frac{d\theta_k}{dt} &= \nu \sin(\bar{\theta} - \theta_k) + W_k \\ &= \frac{\nu}{|\mathcal{J}|} \frac{1}{N} \sum_{j=1}^{N} \sin(\theta_j - \theta_k) - W_k. \end{aligned}$$

This is the Kuramoto model with a coupling constant $K = \frac{\nu}{|\mathcal{J}|}$. In the standard Kuramoto model the coupling constant K is supposed independent of $|\mathcal{J}|$. The reason for taking $K = \frac{\nu}{|\mathcal{J}|}$ here is that the original time-continuous version of the Vicsek model as in [22, 29] corresponds to this choice. Additionally, with this choice, the macroscopic limit is simpler.

In the context of the Vicsek model, the case where $\frac{\nu}{|\mathcal{J}|}$ is a constant (or more generally a smooth function of $|\mathcal{J}|$) has been studied in [24, 26, 27]. In this case, multiple equilibria and phase transitions may appear. Phase transitions are also seen in the Kuramoto model.[1, 10, 11, 47, 48, 67] This makes the physics more interesting but on the other hand, complicates the derivation of hydrodynamic models. Hence, in the present work, we keep the assumption of constant ν for the sake of simplicity and defer the study of the constant $\frac{\nu}{|\mathcal{J}|}$ case to future work.

In the limit of an infinite number of particles $N \to \infty$, the system can be described by the one-particle distribution function $f(x, v, W, t)$ where (x, v, W) is the position in the phase space $\mathbb{R}^2 \times \mathbb{S}^1 \times \mathbb{R}$. The quantity $f(x, v, W, t)\, dx\, dv\, dW$ represents the probability of finding a particle in

a neighborhood $dx\,dv\,dW$ of (x, v, W). The evolution equation for f deduced from system (2.2.1), (2.2.2) is given by the following Fokker-Planck equation[12]:

$$\partial_t f - c\nabla_x \cdot (vf) + \nabla_v \cdot (F_f f) - D\Delta_v f = 0, \tag{2.2.5}$$

$$F_f(x, v, W, t) = P_{v^\perp}(\nu\, v_f(x, t)) + Wv^\perp, \tag{2.2.6}$$

This equation expresses that the time derivative of f is balanced by, on the one hand, first order fluxes in the (x, v) space describing spatial transport by the velocity cv (the second term) and velocity transport by the force F_f (the third term) and by, on the other hand, velocity diffusion due to the Brownian noise (the fourth term). The operators $\nabla_v\cdot$ and Δ_v respectively stand for the divergence of tangent vector fields to $\mathbb{S}^1$ and the Laplace-Beltrami operator on $\mathbb{S}^1$. For later usage, we also introduce the symbol ∇_v which denotes the tangential gradient of scalar fields defined on $\mathbb{S}^1$. Let $\varphi(v)$ be a scalar function defined on $\mathbb{S}^1$ and let $\varphi(v)v^\perp$ a tangent vector field to $\mathbb{S}^1$. Denote by $\bar\varphi(\theta)$ the expression of $\varphi(v)$ in a polar coordinate system. Then, these operators are expressed as follows:

$$\nabla_v \cdot (\varphi(v)v^\perp) = \partial_\theta\bar\varphi, \quad \nabla_v\varphi(v) = \partial_\theta\bar\varphi\, v^\perp, \quad \Delta_v\varphi(v) = \partial_\theta^2\bar\varphi.$$

Eq. (2.2.6) describes how the force term is computed. The first term describes the interaction force: it has has the form of a relaxation towards the neighbors' average velocity $\bar v_f(x, t)$ with a relaxation frequency ν. The second term is the self-rotation force with angular velocity W. We note that there is no operator explicitly acting on the angular velocity W. Indeed, this quantity is supposed attached to each particle and invariant over time. System (2.2.5), (2.2.6) is supplemented with an initial condition $f_I(x, v, W) = f(x, v, W, t = 0)$.

We will present several ways of computing the neighbors' average velocity $\bar v_f(x, t)$. To make the model specific at this point, we simply consider the case where it is computed by the continuum counterpart of the discrete formula (2.2.3), namely:

$$\bar v_f(x, t) = \frac{\mathcal{J}_f(x, t)}{|\mathcal{J}_f(x, t)|}, \tag{2.2.7}$$

$$\mathcal{J}_f(x, t) = \int_{(y,v,W)\in\mathbb{R}^2\times\mathbb{S}^1\times\mathbb{R}} K\Big(\frac{|x-y|}{R}\Big)\, f(y, v, W, t)\, v\, dy\, dv\, dW. \tag{2.2.8}$$

Here the summation of the neighbor's velocities over a disk centered at the location x of the particle and of radius R which was used in the discrete model (formula (2.2.3)) is replaced by a more general formula involving a radially symmetric interaction kernel K. We recover an integration over such a disk if we choose $K(\xi) = \lambda_{[0,1]}(\xi)$, with $\xi = \frac{|x-y|}{R}$ and $\lambda_{[0,1]}$ is the indicator function of the interval $[0, 1]$. For simplicity, we now normalize K such that $\int_{\mathbb{R}^2} K(|x|)\, dx = 1$. The parameter R will be referred to as the interaction range.

In order to define the hydrodynamic scaling, we first non-dimensionalize the system. We introduce the time scale $t_0 = \nu^{-1}$ and the associated space scale $x_0 = ct_0 = c/\nu$. With these choices, the time unit is the time needed by a particle to adjust its velocity due to interactions with other particles (or mean interaction time) and the space unit is the mean distance traveled by the particles during the mean interaction time. We set W_0 the typical angular frequency. For instance, we can assign to W_0 the value $\bar W_1 + \bar W_2$ where $\bar W_1$ and $\bar W_2$ are respectively the mean and the standard deviation of W over the initial probability distribution function $f_I\, dx\, dv\, dW$. Similarly, we introduce a distribution function scale $f_0 = \frac{1}{r_0^2 W_0}$ and a force scale $F_0 = \frac{1}{t_0}$.

We introduce dimensionless variables $x = x_0 x'$, $t = t_0 t'$, $W = W_0 W'$, $f = f_0 f'$, $F_f = F_0 F'_{f'}$ as well as the following dimensionless parameters:

$$d = \frac{D}{\nu}, \qquad \Upsilon = \frac{W_0}{\nu}, \qquad r = \frac{R\,\nu}{c}. \tag{2.2.9}$$

These parameters are respectively the dimensionless diffusivity, the dimensionless intrinsic angular velocity and the dimensionless interaction range. The non-dimensionlized system solved by

$f'(x', v', W', t')$ is written as follows (dropping the primes for simplicity):

$$\partial_t f + \nabla_x \cdot (v f) + \nabla_v \cdot (F_f f) - d\Delta_v f = 0. \tag{2.2.10}$$

$$F_f(x, v, W, t) = P_{v^\perp} \bar{v}_f(x, t) - \Upsilon W v^\perp, \tag{2.2.11}$$

where, in the simple example given above, the neighbors' average velocity is now given by

$$\bar{v}_f(x, t) = \frac{\mathcal{J}_f(x, t)}{|\mathcal{J}_f(x, t)|}, \tag{2.2.12}$$

$$\mathcal{J}_f(x, t) = \int_{(y,v,W)\in\mathbb{R}^2\times\mathbb{S}^1\times\mathbb{R}} K\Big(\frac{|x - y|}{r}\Big) f(y, v, W, t)\, v\, dy\, dv\, dW. \tag{2.2.13}$$

So far, the chosen time and space scales are microscopic ones: they are set up to describe the evolution of the system at the scale of the interactions between the agents. We are now interested by a description of the system at macroscopic scales, i.e. at scales which are described by units $\bar{x}_0 = \frac{x_0}{\varepsilon}$ and $\bar{t}_0 = \frac{t_0}{\varepsilon}$ where $\varepsilon \ll 1$ is a small parameter. By changing these units, we correspondingly change the variables x and t and the unknown f to new variables and unknowns $\tilde{x} = \varepsilon x$, $\tilde{t} = \varepsilon t$, $\tilde{f} = \frac{f}{\varepsilon^2}$. In performing this change of variables, we must state how the dimensionless parameters (2.2.9) behave as $\varepsilon \to 0$. We assume that $d = \mathcal{O}(1)$ and $r = \mathcal{O}(1)$ as $\varepsilon \to 0$, and for simplicity, we assume that d and r remain constant. By contrast, we will investigate two different scaling assumptions for Υ and we define a new parameter $\eta = \frac{\varepsilon}{\Upsilon}$. After changing to the macroscopic variables $\tilde{x}$, $\tilde{t}$ the system reads (dropping the tildes for simplicity):

$$\partial_t f^\varepsilon + \nabla_x \cdot (v f^\varepsilon) = \frac{1}{\varepsilon}\Big(- \nabla_v \cdot (P_{v^\perp} \bar{v}^\varepsilon_{f^\varepsilon} f^\varepsilon) + d\Delta_v f^\varepsilon\Big) - \frac{1}{\eta} W \nabla_v \cdot (v^\perp f^\varepsilon), \tag{2.2.14}$$

where again in the simplest case, the neighbors' average velocity is given by

$$\bar{v}^\varepsilon_f(x, t) = \frac{\mathcal{J}^\varepsilon_f(x, t)}{|\mathcal{J}^\varepsilon_f(x, t)|}, \tag{2.2.15}$$

$$\mathcal{J}^\varepsilon_f(x, t) = \int_{(y,v,W)\in\mathbb{R}^2\times\mathbb{S}^1\times\mathbb{R}} K\Big(\frac{|x - y|}{\varepsilon r}\Big) f(y, v, W, t)\, v\, dy\, dv\, dW. \tag{2.2.16}$$

Next, by Taylor expansion and owing to the rotational symmetry of the function $x \in \mathbb{R}^2 \mapsto K(|x|)$, we have [29]:

$$\bar{v}^\varepsilon_f(x, t) = \Omega_f(x, t) - \mathcal{O}(\varepsilon^2), \qquad \Omega_f(x, t) = \frac{J_f(x, t)}{|J_f(x, t)|}, \tag{2.2.17}$$

$$J_f(x, t) = \int_{(v,W)\in\mathbb{S}^1\times\mathbb{R}} f(x, v, W, t)\, v\, dv\, dW \tag{2.2.18}$$

In other words, up to $\mathcal{O}(\varepsilon^2)$ terms, the interaction force is given by a local expression, involving only the distribution function f at position x. The quantity $J_f(x, t)$ is the local particle flux at point x and time t. By contrast, the expression (2.2.15), (2.2.16) of $\bar{v}^\varepsilon_f$ is spatially non-local: it involves a convolution of f with respect to the non-local kernel K. We now omit the $\mathcal{O}(\varepsilon^2)$ terms as they have no contribution to the hydrodynamic limit at leading order (which is what we are interested in).

The remainder of this work is concerned with the formal limit $\varepsilon \to 0$ of the following perturbation problem:

$$\partial_t f^\varepsilon + \nabla_x \cdot (v f^\varepsilon) = \frac{1}{\varepsilon}\Big(- \nabla_v \cdot (P_{v^\perp} \Omega_{f^\varepsilon} f^\varepsilon) + d\Delta_v f^\varepsilon\Big) - \frac{1}{\eta} W \nabla_v \cdot (v^\perp f^\varepsilon), \tag{2.2.19}$$

$$\Omega_f(x, t) = \frac{J_f(x, t)}{|J_f(x, t)|}, \quad J_f(x, t) = \int_{(v,W)\in\mathbb{S}^1\times\mathbb{R}} f(x, v, W, t)\, v\, dv\, dW. \tag{2.2.20}$$

We will be interested in the following two scaling assumptions for η

(i) Small angular velocities: $\eta = \mathcal{O}(1)$. In this regime, the characteristic angular velocity satisfies $\Upsilon = \mathcal{O}(\varepsilon)$. It takes the particles a macroscopic time interval to perform a finite angle rotation.

(ii) Large angular velocities: $\eta = \mathcal{O}(\varepsilon)$. In this case, the characteristic angular velocity satisfies $\Upsilon = \mathcal{O}(1)$. It takes the particles a microscopic time interval to perform finite angle rotations. Over a macroscopic time interval, the number of rotations is $\mathcal{O}\left(\frac{1}{\varepsilon}\right)$.

We expect that case (i) is just a perturbation of the case where there is no proper rotation, and which has previously been investigated in [29]. On the other hand, case (ii) involves a larger modification and we expect that significant new behaviors are captured. However, we will see that case (ii) requires a modification of the way the agents' turning velocity is computed. Indeed, the agents need to take their proper angular velocity into account in the evaluation of the turning velocity that produces alignment with their neighbors. Therefore, according to whether that proper velocity goes along or against their will, the agents need to achieve smaller or larger turning. Precisely, the changes to Eq. (2.2.20) that are needed will be described in greater detail below. The next section is devoted to the investigation of case (i).

2.3 Small angular velocities

In the case of small angular velocities, we have $\eta = \mathcal{O}(1)$. We make $\eta = 1$ for simplicity. The problem is now written:

$$\partial_t f^\varepsilon + \nabla_\perp \cdot (v f^\varepsilon) - W \nabla_v \cdot (v^\perp f^\varepsilon) = \frac{1}{\varepsilon} Q(f^\varepsilon), \tag{2.3.21}$$

where the 'collision operator' $Q(f)$ is given by:

$$Q(f) = -\nabla_v \cdot (P_{v^\perp} \Omega_f f) + d\Delta_v f, \tag{2.3.22}$$

$$\Omega_f(x,t) = \frac{J_f(x,t)}{|J_f(x,t)|}, \quad J_f(x,t) = \int_{(v,W)\in\mathbb{S}^1\times\mathbb{R}} f(x,v,W,t)\, v\, dv\, dW. \tag{2.3.23}$$

The formal limit $\varepsilon \to 0$ has been established in [29, 32] when there is no self-rotation term $W\nabla_v \cdot (v^\perp f^\varepsilon)$ and no dependence of f upon W. The present analysis is a somewhat straightforward extension of this earlier work. Before stating the theorem, we need to recall the definition of the von Mises-Fisher (VMF) distribution $M_\Omega(v)$. Its expression is given by:

$$M_\Omega(v) = Z_d^{-1} \exp\left(\frac{v\cdot\Omega}{d}\right), \qquad Z_d = \int_{v\in\mathbb{S}^1} \exp\left(\frac{v\cdot\Omega}{d}\right) dv. \tag{2.3.24}$$

By construction, $M_\Omega(v)$ is a probability density and due to rotational symmetry, the constant Z_d does not depend on Ω. The flux of the VMF distribution is given by:

$$\int_{v\in\mathbb{S}^1} M_\Omega(v)\, v\, dv = c_1\, \Omega, \qquad c_1 = c_1(d) = \frac{\int_{v\in\mathbb{S}^1} \exp\left(\frac{v\cdot\Omega}{d}\right)(v\cdot\Omega)\, dv}{\int_{v\in\mathbb{S}^1} \exp\left(\frac{v\cdot\Omega}{d}\right) dv}. \tag{2.3.25}$$

The parameter $c_1(d)$ does not depend on Ω. It is given by

$$c_1(d) = \frac{\int_0^\pi e^{\frac{\cos\theta}{d}} \cos\theta\, d\theta}{\int_0^\pi e^{\frac{\cos\theta}{d}}\, d\theta} = \frac{I_1\left(\frac{1}{d}\right)}{I_0\left(\frac{1}{d}\right)},$$

where $\beta \in \mathbb{R} \to I_k(\beta) \in \mathbb{R}$ is the modified Bessel function:

$$I_k(\beta) = \frac{1}{\pi}\int_0^\pi \exp\{\beta\cos\theta\}\, \cos(k\,\theta)\, d\theta. \quad \forall \beta \in \mathbb{R}, \quad \forall k \in \mathbb{N}.$$

It verifies $0 \leq c_1(d) < 1$ and is a strictly decreasing function of $d \in [0, \infty)$. When c_1 is small, the VMF distribution is close to the uniform distribution. By contrast, when c_1 is close to 1, the VMF distribution is close to the Dirac delta at $v = \Omega$. The parameter c_1 measures the degree of alignment of the VMF distribution about the direction of Ω, hence its name of 'order parameter'.

Now, we can state the theorem which establishes the limit $\varepsilon \to 0$ of (2.3.21).

Theorem 2.3.1. *We assume that the limit $f^0 = \lim_{\varepsilon \to 0} f^\varepsilon$ exists and that the convergence is as regular as needed (i.e. occurs in functional spaces that allow the rigorous justification of all the computations below). Then, we have*

$$f^0(x, v, W, t) = \rho_W(x, t)\, M_{\Omega(x,t)}(v). \tag{2.3.26}$$

where, for any (x, t), the function $W \in \mathbb{R} \to \rho_W(x, t) \in \mathbb{R}$ belongs to $L^1(\mathbb{R})$ and has first moment finite, and the vector $\Omega(x, t)$ belongs to $\mathbb{S}^1$. The functions $\rho_W(x, t)$ and $\Omega(x, t)$ satisfy the following system of hydrodynamic equations:

$$\partial_t \rho_W + \nabla_x \cdot (c_1 \rho_W\, \Omega) = 0, \quad \forall W \in \mathbb{R}, \tag{2.3.27}$$

$$\rho \left(\partial_t \Omega + c_2\, (\Omega \cdot \nabla_x)\Omega - Y \Omega^\perp \right) + d\, P_{\Omega^\perp} \nabla_x \rho = 0, \tag{2.3.28}$$

$$\rho(x, t) \int_{W \in \mathbb{R}} \rho_W(x, t)\, dW, \qquad (\rho Y)(x, t) \int_{W \in \mathbb{R}} \rho_W(x, t)\, W\, dW. \tag{2.3.29}$$

The constants c_1, c_2 are respectively given by formulas (2.3.25) and (2.6.100) in 2.6 below. Moreover, the 'average rotation velocity' Y satisfies the following transport equation (for smooth solutions):

$$\partial_t Y + c_1\, \rho \Omega \cdot \nabla_x Y = 0, \tag{2.3.30}$$

which simply expresses that the average rotation velocity Y is convected at the flow speed $c_1 \Omega$.

The proof of Theorem 2.3.1 is developed in 2.6. We now discuss the significance of the results. Eq. (2.3.27) is a continuity equation for the density of particles of given proper angular velocity W. Indeed, since the interactions do not modify the proper angular velocities of the particles, we must have an equation expressing the conservation of particles for each of these velocities W. However, the self alignment force modifies the actual direction of motion v of the particles. This interaction couples particles with different proper angular velocities. Therefore, the mean direction of motion Ω is common to all particles (and consequently, does not depend on W) and obeys a balance equation which bears similarities with the gas dynamics momentum conservation equations.

Since c_1 and Ω do not depend on W, the dependence on W in eq. (2.3.27) can be integrated out, which leads to the following system of equations:

$$\partial_t \rho + \nabla_x \cdot (c_1 \rho \Omega) = 0, \tag{2.3.31}$$

$$\partial_t (\rho Y) + \nabla_x \cdot (c_1 \rho Y \Omega) = 0, \tag{2.3.32}$$

$$\rho \left(\partial_t \Omega + c_2\, (\Omega \cdot \nabla_x)\Omega - Y \Omega^\perp \right) + d\, P_{\Omega^\perp} \nabla_x \rho = 0. \tag{2.3.33}$$

Therefore, ρ, Y and Ω can first be computed by solving the system (2.3.31), (2.3.32), (2.3.33). Once Ω is known, eq. (2.3.27) is just a transport equation with given coefficients, which can be easily integrated (provided that the vector field Ω is smooth). Eq. (2.3.31) expresses the conservation of the total density of particles (i.e. integrated with respect to $W \in \mathbb{R}$), while (2.3.32) expresses the conservation of the 'angular momentum density' ρY. Eq. (2.3.30) can be deduced from eq. (2.3.32) (for smooth solutions) by using the mass conservation eq. (2.3.31).

Suppose that $Y_{t=0} = 0$. Then, by (2.3.30), we have $Y(x, t) \equiv 0$ for all $(x, t) \in \mathbb{R}^2 \times [0, \infty)$. In this case, the system reduces to the following one:

$$\partial_t \rho + \nabla_x \cdot (c_1 \rho \Omega) = 0, \tag{2.3.34}$$

$$\rho \left(\partial_t \Omega + c_2\, (\Omega \cdot \nabla_x)\Omega \right) + d\, P_{\Omega^\perp} \nabla_x \rho = 0, \tag{2.3.35}$$

which has been studied in earlier work.[25, 29, 32, 71] This system is referred to as the **'Self-Organized Hydrodynamics' (SOH)**. As mentioned above, it bears similarities with the isothermal compressible gas dynamics equations, but differs from it by several aspects, which have been developed in earlier work (see e.g. the review [25]). These are:

(i) The mean velocity Ω is a vector of unit norm (specifically, it is the direction of the mean velocity rather than the mean velocity itself).

(ii) The projection operator $P_{\Omega^\perp}$ multiplies the pressure gradient term $d\nabla_x\rho$. It is required to maintain the constraint that $|\Omega| = 1$. Indeed, multiplying scalarly (2.3.28) by Ω, we realize that $(\partial_t + c_2\Omega\cdot\nabla_x)|\Omega|^2 = 0$. Therefore, if $|\Omega| = 1$ uniformly at $t = 0$, it stays of unit norm at all times. The projection operator $P_{\Omega^\perp}$ brings a non-conservative term in this equation. Hence, (2.3.28) is not a conservation equation: it does not express any momentum balance.

(iii) The convection velocity of Ω is c_2 and is different from the convection velocity c_1 of ρ. In classical fluids, these two velocities are equal. This results from the Galilean invariance of the gas dynamics system. Here, the system is not Galilean invariant (the velocities are normalized to 1: this property is not invariant under Galilean transforms) and consequently, these two convection velocities may differ. The loss of Galilean invariance by fluid models of self-propelled particles has been noted earlier [91, 92]. As a consequence, in such fluids, the propagation of sound is anisotropic [92].

The model with non-vanishing average rotation velocity (2.3.31)-(2.3.33) appears as an enrichment of the standard SOH model by the following two aspects:

(i) An additional term, namely $-Y\Omega^\perp$, is present in the velocity evolution eq. (2.3.33). This term expresses how the self-rotation of the particles influences the evolution of the mean velocity direction Ω. Quite naturally, it depends on the angular momentum density ρY which provides the contribution of the proper angular rotation of the particles to the evolution of the mean velocity.

(ii) An additional equation, namely (2.3.32) (or (2.3.30) in non-conservative form) is added to the system. It shows that the average angular velocity Y is passively transported by the flow velocity $c_1\Omega$.

This model will be referred to as the **'Self-Organized Hydrodynamics with Proper Rotation (small angular velocity case)' or SOHPR-S**.

In [29, 32], it is shown that the SOH model (2.3.34), (2.3.35) is hyperbolic. Its two eigenvalues evaluated at a state (ρ,Ω) are given by

$$\lambda_\pm = \frac{1}{2}\left[(c_1+c_2)\cos\theta \pm \left((c_2 - c_1)^2\cos^2\theta + 4d\sin^2\theta\right)^{1/2}\right], \tag{2.3.36}$$

where $\Omega = (\cos\theta,\sin\theta)^T$ and the exponent "T" denotes the transpose of a vector. Apart from additional zero-th order terms, the SOHPR-S model is derived from the SOH model by the addition of the convection equation (2.3.30) with convection velocity $c_1\Omega$. It is a hyperbolic problem, whose eigenvalues consist of the two eigenvalues (2.3.36) of the SOH model on the one hand, and of the convection speed $c_1\cos\theta$ of the additional equation (2.3.30) on the other hand. These three eigenvalues are real and distinct, except in the case $\theta = 0$. Therefore, the problem is strictly hyperbolic in most of the domain where the state variables (ρ,Ω) are defined. This gives a good indication that at least local well-posedness of the SOHPR-S model can be achieved.

2.4 Large angular velocities

Now, we investigate the case of large proper angular velocities, i.e. $\eta = \mathcal{O}(\varepsilon)$. We make $\eta = \varepsilon$ for simplicity. The problem is now written:

$$\partial_t f^\varepsilon + \nabla_x \cdot (v f^\varepsilon) - \frac{1}{\varepsilon}\big(\quad \nabla_v \cdot (P_{v^\perp} \omega_{f^\varepsilon}(W)\, f^\varepsilon) - W \nabla_v \cdot (v^\perp f^\varepsilon) + d\Delta_v f^\varepsilon \big), \tag{2.4.37}$$

Now, by contrast to the small angular velocity case (section 2.3), we abandon the hypothesis that ω_f which is defined by (2.4.37), is equal to Ω_f, where we recall that (see 2.3.23):

$$\Omega_f(x,t) = \frac{J_f(x,t)}{|J_f(x,t)|}, \quad J_f(x,t) = \int_{(v,W)\in \mathbb{S}^1 \times \mathbb{R}} f(x,v,W,t)\, v\, dv\, dW. \tag{2.4.38}$$

Indeed, the agents' proper angular velocity being large, it influences their evaluation of the turning velocity that produces alignment with their neighbors. According to the situation, the proper angular velocity goes along or against the turning direction they want to achieve. Therefore, the agents need to compensate for it by realizing smaller or larger turning speeds. This results in a prescription for ω_f which is different from Ω_f and which requires ω_f to be dependent of W, as indicated in (2.4.37).

The precise determination of ω_f requires several steps. Before going into this determination, we write (2.4.37) as follows:

$$\partial_t f^\varepsilon + \nabla_x \cdot (v f^\varepsilon) = \frac{1}{\varepsilon} \tilde{Q}(f^\varepsilon), \tag{2.4.39}$$

where $\tilde{Q}(f)$ is a new collision operator given by:

$$\tilde{Q}(f) = \tilde{Q}_{\omega_f}(f). \tag{2.4.40}$$

where ω_f: $W \in \mathbb{R} \to \omega_f(W) \in \mathbb{S}^1$ is the function to be determined below and where, for any given function ω: $W \subset \mathbb{R} \to \omega(W) \in \mathbb{S}^1$, we define:

$$\tilde{Q}_\omega(f) := -\nabla_v \cdot (F_\omega f) + d\Delta_v f, \tag{2.4.41}$$

$$F_\omega(v,W) := P_{v^\perp}\omega(W) + Wv^\perp. \tag{2.4.42}$$

We define $\tilde{\mathcal{E}}_\omega$, the set of equilibria of $\tilde{Q}_\omega$, as follows:

Definition 2.4.1. *Let ω: $W \subset \mathbb{R} \to \omega(W) \in \mathbb{S}^1$ be given. The set $\tilde{\mathcal{E}}_\omega$ of equilibria of $\tilde{Q}_\omega$ is defined by*

$$\tilde{\mathcal{E}}_\omega := \big\{ f \in L^1(\mathbb{R}, C^2(\mathbb{S}^1)) \mid f \geq 0 \ \text{ and } \ \tilde{Q}_\omega(f) = 0 \big\}.$$

To determine $\tilde{\mathcal{E}}_\omega$, we first define what are the analogs of the von Mises-Fisher distributions in the present case. The existence of these objects requires the following preliminary lemma.

Lemma 2.4.2. *Let $W \subset \mathbb{R}$ be given. There exists a unique 2π periodic solution of the following problem:*

$$\Phi''_W(\theta) - \frac{1}{d}\big((W - \sin\theta)\Phi_W\big)'(\theta) = 0, \qquad \int_0^{2\pi} \Phi_W(\theta)\, d\theta = 1, \tag{2.4.43}$$

where the primes denote derivatives with respect to θ. We denote by Φ_W this unique solution. It is positive and it belongs to $C^\infty(\mathbb{S}^1)$.

We can now define the analogs of the von Mises-Fisher distributions:

Definition 2.4.3. *Let Φ_W be the function defined in the previous lemma. Let $\omega: W \in \mathbb{R} \to \omega(W) \in \mathbb{S}^1$ be fixed. We define $\tilde{M}_\omega$ such that:*

$$\tilde{M}_\omega(v, W) = \Phi_W(\theta), \quad \text{with} \quad \theta = \widehat{(\omega(W), v)}. \tag{2.4.44}$$

For any given $W \in \mathbb{R}$, the distribution $\tilde{M}_\omega(v, W)\, dv$ is a probability measure on $\mathbb{S}^1$. We refer to it as the 'Generalized von Mises-Fisher' (GVM) distribution.

Thanks to the definition of $\tilde{M}_\omega$, we can describe the set $\tilde{\mathcal{E}}_\omega$, as done in the lemma just below:

Lemma 2.4.4. *The set $\tilde{\mathcal{E}}_\omega$ is the set of all functions of the form*

$$(v, W) \mapsto \rho_W \tilde{M}_\omega(v, W), \tag{2.4.45}$$

where the function $W \mapsto \rho_W \in \mathbb{R}_+$ is arbitrary in $L^1(\mathbb{R})$.

We now define the direction of the flux associated to a GVM equilibrium $\tilde{M}_\omega$:

Definition 2.4.5. *Given $\omega: W \in \mathbb{R} \mapsto \omega(W) \subset \mathbb{S}^1$ and $W \in \mathbb{R}$, we define:*

$$u_\omega(W) = \int_{v \in \mathbb{S}^1} \tilde{M}_\omega(v, W)\, v\, dv, \tag{2.4.46}$$

$$\Psi_\omega(W) = \frac{u_\omega(W)}{|u_\omega(W)|}, \qquad \tilde{c}_{1,\omega}(W) = |u_\omega(W)|. \tag{2.4.47}$$

We have $u_\omega(W) \in \mathbb{R}^2$, $\Psi_\omega(W) \subset \mathbb{S}^1$. The vector $\Psi_\omega(W)$ is the direction of the GVM $\tilde{M}_\omega$ for a given angular rotation W and the real number $\tilde{c}_{1,\omega}(W)$ is its order parameter for this angular rotation (again, we have $0 \leq \tilde{c}_{1,\omega}(W) \leq 1$).

We stress the fact that $\Psi_\omega(W) \neq \omega$ unless $W = 0$. This is in marked contrast with the small angular velocity case, where the direction of the VMF distribution M_Ω is precisely equal to Ω. This is the reason why, in the present case, we cannot set $\omega_f = \Omega_f$ (we recall that, for a given distribution f, the direction of the local flux Ω_f is given by (2.4.38)). Indeed, the 'consistency relation' that the direction of the equilibrium M_{Ω_f} should be Ω_f would not be realized. So for a given local velocity direction Ω_f, we will have to look for $\omega_f(W)$ which realizes that, for any value of the angular velocity W, the direction of the associated GVM $\tilde{M}_{\omega_f}$ is equal to Ω_f, i.e. $\Psi_{\omega_f}(W) = \Omega_f$. From the present considerations, we will have $\omega_f(W) \neq \Omega_f$, unless $W = 0$. To do this, we have a few steps to go. For later usage, we first state the following auxiliary lemma:

Lemma 2.4.6. *The real number $\tilde{c}_{1,\omega}(W)$ does not depend on ω and is denoted below $\tilde{c}_1(W)$.*

Now, as developed above, for a fixed direction Ω, we are interested in finding a function ω such that the direction $\Psi_\omega(W)$ of $\tilde{M}_\omega$ coincides with Ω, for all angular velocities W. Such an ω can be uniquely determined, as the lemma below shows.

Lemma 2.4.7. *Let $\Omega \subset \mathbb{S}^1$. Then, the equation $\Psi_\omega(W) = \Omega$, $\forall W \in \mathbb{R}$, determines a unique function $\omega: W \in \mathbb{R} \mapsto \omega(W) \in \mathbb{S}^1$. We denote this unique solution by ω_Ω. By definition, we have*

$$\Psi_{\omega_\Omega}(W) = \Omega, \quad \forall W \in \mathbb{R}. \tag{2.4.48}$$

Now, as explained above, we define ω_f such that the direction $\Psi_{\omega_f}(W)$ of the associated GVM $\tilde{M}_{\omega_f}$ coincides with the local flux Ω_f for all values of the angular velocity $W \in \mathbb{R}$. This leads to the following definition:

Definition 2.4.8. *Given a distribution function $f(\omega, W)$, we define ω_f by:*

$$\omega_f = \omega_{\Omega_f}, \tag{2.4.49}$$

i.e. we have,

$$\Psi_{\omega_f}(W) = \Omega_f, \quad \forall W \in \mathbb{R}. \tag{2.4.50}$$

The proofs of Lemmas 2.4.2 to 2.4.7 are given in 2.6.

We now comment on the rationale for the definition of ω_f. The Individual-Based model whose mean-field limit gives rise to the kinetic equation (2.4.37) is obviously as follows (with the notations of section 3.2):

$$\frac{dX_k}{dt} = V_k, \tag{2.4.51}$$

$$dV_k = P_{V_k^\perp} \circ (\omega_{\bar{V}_k}(W_k)\,dt + \sqrt{2D}\,dB_t) + W_k V_k^\perp\,dt. \tag{2.4.52}$$

Here, $\omega_{\bar{V}_k}$ is the function defined by (2.4.48) where Ω is substituted by $\bar{V}_k$. The goal is to model a relaxation dynamic towards the local mean alignment direction, i.e. the direction $\bar{V}_k$. For this to happen, the particles have to choose the alignment force $P_{V_k^\perp}\omega_{\bar{V}_k}$ in a proper way. Because of the self-rotation velocity W_k, this force cannot be equal to $P_{V_k^\perp}\bar{V}_k$. Indeed, if this were the case, the relaxation force would vanish when $V_k = \bar{V}_k$ and could not compensate for the self-rotation force $W_k V_k^\perp$. In the absence of noise, the alignment force $P_{V_k^\perp}\omega_{\bar{V}_k}$ which compensates for self rotation is given by

$$P_{V_k^\perp}\omega_{\bar{V}_k} + W_k V_k^\perp = P_{V_k^\perp}\bar{V}_k,$$

(which has a solution $\omega_{\bar{V}_k}$ only in a finite range of values of W_k). In the presence of noise, the alignment force which compensates for self-rotation cannot be computed a priori. To propose an explicit value of $\omega_{\bar{V}_k}$, we assume that the distribution of the particles in (v, W)-space is locally at equilibrium, i.e. is a GVM distribution $M_{\omega_{\bar{V}_k}}$. Then, the alignment force $P_{V_k^\perp}\omega_{\bar{V}_k}$ vanishes when V_k is equal to $\omega_{\bar{V}_k}$, i.e. when V_k coincides with the direction ω_{V_k} such that there is no action on the particles when they are distributed according to a GVM. Indeed, when $V_k = \omega_{\bar{V}_k}$, the right-hand side of (2.4.52) is zero on the average in the sense that the associated Fokker-Planck operator resulting from applying the Ito formula to (2.4.52) vanishes (which is what saying that the particle distribution is a GVM means). This means that the relaxation has been achieved 'statistically'. Once translated in the mean-field framework of (2.4.37), this leads to our definition (2.4.50).

Obviously, the use of the equilibrium to compute ω_f restricts the applicability of this model to a situation close to such an equilibrium. Since the goal is precisely to explore the hydrodynamic regime which prevails in such situations of closeness to equilibrium, this approach is still consistent. Another question is about the likeliness that agents are able to perform such a complicated computation. However, we can think that this dynamic is a simple outcome of collisions between the particles. Imagine a set of self-rotating robots with elongated shapes. The volume-exclusion interaction between elongated self-propelled objects through hard-core collisions results in an alignment dynamic, as already shown in e.g. [5, 23, 58, 75]. Therefore, the 'computation' of the magnitude of the self-alignment force may be just an outcome of an equilibration between the self rotation force and the pressure exerted by the neighboring agents through the collisions.

The goal is now to investigate the limit $\varepsilon \to 0$ of the solution of (2.4.39). More precisely, we show the

Theorem 2.4.9. *Let f^ε be a solution of (2.4.37) with ω_f given by (2.4.49). We assume that the limit $f^0 = \lim_{\varepsilon\to 0} f^\varepsilon$ exists and that the convergence is as regular as needed. Then, we have*

$$f^0(x,v,W,t) = \rho_W(x,t)\,\tilde{M}_{\omega_{\Omega(x,t)}}(v,w). \tag{2.4.53}$$

where, for any (x,t), the function $W \in \mathbb{R} \mapsto \rho_W(x,t) \in \mathbb{R}$ belongs to $L^1(\mathbb{R})$ and the vector $\Omega(x,t)$ belongs to $\mathbb{S}^1$. The functions $\rho_W(x,t)$ and $\Omega(x,t)$ satisfy the following system of hydrodynamic equations:

$$\partial_t \rho_W + \nabla_x \cdot (c_1 \rho_W \Omega) = 0, \quad \forall W \in \mathbb{R}, \tag{2.4.54}$$

$$\begin{aligned} &m_1[\rho_W]\,\Omega_t + m_2[\rho_W](\Omega\cdot\nabla_x)\Omega + m_3[\rho_W]\,(\Omega^\perp\cdot\nabla_x)\Omega \\ &\quad + \Omega^\perp\left(m_4[\rho_W]\,(\nabla_x\cdot\Omega) + (\Omega^\perp\cdot\nabla_x)\,m_5[\rho_W] + (\Omega\cdot\nabla_x)\,m_6[\rho_W]\right) = 0, \end{aligned} \tag{2.4.55}$$

where $m_1[\rho_W], \ldots, m_6[\rho_W]$ are moments of ρ_W given by formulas (2.6.137) in 2.6 below.

Eq. (2.4.54) expresses the conservation of particles of given angular momentum W, exactly in the same way as in the small angular velocity case (see Eq. (2.3.27)). The velocity evolution eq. (2.4.55) has also a similar structure (see Eq. (2.3.28)) but contains more terms. The analog terms to those of (2.3.28) are the first term (corresponding to the first term of (2.3.28)), the second one (corresponding to the second term of (2.3.28)) and the fifth one (corresponding to the fourth term of (2.3.28)). The difference is the replacement of ρ, which appears in the three terms of (2.3.28) by three different moments of ρ_W. This is a consequence of the dependence of the GVM $\tilde{M}_{\omega_\Omega}$ and the GCI $\tilde{\chi}_\Omega$ (which will be found in section 2.6) on the angular velocity W. There was no such dependence of the VMF M_Ω and of the GCI χ_Ω in the small angular velocity case.

The third term of (2.3.28) which originated from the particle self-rotation disappears in the large angular velocity case investigated here, but three new terms appear. The third term of (2.4.55) describes transport in the direction perpendicular to the mean velocity Ω. The direction of transport is determined by the sign of m_3. The fourth term is a contribution of the compressibility of the velocity field to its transport: regions of compression or rarefaction induce rotation of the velocity field in one direction or the other one according to the sign of m_4. Finally, the sixth term is an off-diagonal term in the pressure tensor, where gradients of the moment m_6 of the density distribution ρ_W induce rotation of the velocity field. All these three terms obviously translate the average influence of the individual particle self-rotation.

By analogy with the previous model, this model will be referred to as the **'Self-Organized Hydrodynamics with Proper Rotation (Large angular velocity case)' or SOHPR-L** .

The proof of Theorem 2.4.9 follows the same structure as the small angular velocity case. We start with the definition of the equilibria, followed by the determination of the GCI. We end up with the convergence $\varepsilon \to 0$.

2.5 Properties of the SOHPR-L hydrodynamic model

We investigate some properties of the SOHPR-L hydrodynamic model (2.4.54), (2.4.55). In a first section, we study its linearized stability about a uniform steady-state. For the sake of simplicity, we restrict ourselves to the case where the unperturbed density distribution ρ_W is even in W (which means that there are as many particles rotating in the clockwise direction with angular speed $|W|$ as particles rotating counter-clockwise with the same angular speed). In this case, we prove the linearized stability of the model. This is a good indication of the well-posedness of the SOHPR-L model in this case, although a rigorous proof of this fact is still lacking. The investigation of the linearized stability of the SOHPR-L model in the general case is deferred to future work.

In a second section, we investigate the asymptotics of the SOHPR-L model (as well as that of the SOHPR-S model) when W is small. We show that both models reduce to the SOH model (2.3.34), (2.3.35) in this limit, but with different coefficients. We also establish the asymptotics

of the SOHPR-L model to second order for small W and compare the resulting model to the SOHPR-S model.

2.5.1 Linearized stability of the SOHPR-L system

We first consider a pair (ρ_{0W}, Ω_0) such that (i) ρ_{0W} and Ω_0 are independent of x, (ii) the function $W \in \mathbb{R} \mapsto \rho_{0W}$ belongs to $L^1(\mathbb{R})$, (iii) $\rho_{0W} \geq 0$, (iv) all the moments $m_K[\rho_{0W}]$, $k = 1, \ldots, 6$ exist, (v) $|\Omega_0| = 1$. Such a pair (ρ_{0W}, Ω_0) is a steady-state of the SOHPR-L system (2.4.54), (2.4.55). The goal of this section is to study the linearized stability of the SOHPR-L system about such a uniform steady-state.

We linearize the system. We introduce a small parameter $\delta \ll 1$ and look for solutions such that

$$\rho_W(x,t) = \rho_{0W} + \delta\, \rho_{1W}(x,t) + \mathcal{O}(\delta^2), \qquad \Omega(x,t) = \Omega_0 + \delta\, \Omega_1 + \mathcal{O}(\delta^2). \tag{2.5.56}$$

The constraint $|\Omega(x,t)| = 1$ translates into the constraint

$$\Omega_0 \cdot \Omega_1 = 0. \tag{2.5.57}$$

The linearized system obtained by introducing (2.5.56) into (2.4.54), (2.4.55) and neglecting terms of order $\mathcal{O}(\delta^2)$ reads as follows:

$$\partial_t \rho_{1W} + \tilde{c}_1\, \Omega_0 \cdot \nabla_x \rho_{1W} + \tilde{c}_1\, \rho_{0W}\, \nabla_x \cdot \Omega = 0, \quad \forall W \in \mathbb{R}, \tag{2.5.58}$$

$$\begin{aligned} &m_1\, \Omega_t + m_2\, (\Omega_0 \cdot \nabla_x)\Omega - m_3\, (\Omega_0^{\perp} \cdot \nabla_x)\Omega \\ &\quad + \Omega_0^{\perp} \left(m_4\, (\nabla_x \cdot \Omega) + (\Omega_0^{\perp} \cdot \nabla_x)\, m_5[\rho_W] + (\Omega_0 \cdot \nabla_x)\, m_6[\rho_W] \right) = 0. \end{aligned} \tag{2.5.59}$$

where $m_1, \ldots m_4$ are evaluated on ρ_{0W} except otherwise stated and where the index '1' on the perturbation is omitted for the sake of clarity. Next, we consider plane-wave solutions:

$$\rho_W(x,t) = \tilde{\rho}_W\, e^{i(x\cdot\xi - \mu t)}, \qquad \Omega = \tilde{\Omega}\, e^{i(x\cdot\xi - \mu t)}, \tag{2.5.60}$$

where $\tilde{\rho}_W$, $\tilde{\Omega}$ are the wave amplitudes, $\xi \in \mathbb{R}$ is the wave-number and $\mu \in \mathbb{C}$ is the frequency. Here, $x \in \mathbb{R}$ is a one-dimensional spatial variable, corresponding to the direction of propagation of the plane wave. Indeed, the SOHPR-L being invariant under rotations, the plane-wave analysis is independent of the choice of the direction of propagation. We let $\Omega_0 = (\cos\theta, \sin\theta)$. The constraint (2.5.57) translates into $\Omega_0 \cdot \tilde{\Omega} = 0$, i.e. $\tilde{\Omega} = \tilde{\sigma}(-\sin\theta, \cos\theta)$ with $\tilde{\sigma} \in \mathbb{R}$. Inserting (2.5.60) into (2.5.58), (2.5.59), we get (again, omitting the tildes on ρ_W and Ω for the sake of clarity):

$$\left(-\mu + \tilde{c}_1\, \xi \cos\theta \right) \rho_W - \tilde{c}_1\, \rho_{0W}\, \xi \sin\theta\, \sigma = 0, \quad \forall W \in \mathbb{R}, \tag{2.5.61}$$

$$\begin{aligned} &\left(-\mu\, m_1 + m_2\, \xi \cos\theta - (m_3 + m_4)\, \xi \sin\theta \right) \sigma \\ &\qquad - \xi \sin\theta\, m_5[\rho_W] + \xi \cos\theta\, m_6[\rho_W] = 0. \end{aligned} \tag{2.5.62}$$

From (2.5.61), we get:

$$\rho_W = \frac{\tilde{c}_1\, \rho_{0W}}{-\mu + \tilde{c}_1\, \xi \cos\theta}\, \xi \sin\theta\, \sigma, \quad \forall W \in \mathbb{R}. \tag{2.5.63}$$

Therefore,

$$m_k[\rho_W] = m_k\left[\frac{\tilde{c}_1\, \rho_{0W}}{\mu - \tilde{c}_1\, \xi \cos\theta} \right] \xi \sin\theta\, \sigma, \quad k = 5, 6. \tag{2.5.64}$$

Inserting (2.5.64) into (2.5.62), we get a non-trivial solution σ if and only if the following dispersion relation is satisfied:

$$\begin{aligned} &\mu\, m_1 + m_2\, \xi \cos\theta - (m_3 + m_4)\, \xi \sin\theta \\ &\quad - m_5\left[\frac{\tilde{c}_1\, \rho_{0W}}{-\mu + \tilde{c}_1\, \xi \cos\theta} \right] \xi^2 \sin^2\theta + m_6\left[\frac{\tilde{c}_1\, \rho_{0W}}{-\mu + \tilde{c}_1\, \xi \cos\theta} \right] \xi^2 \cos\theta \sin\theta = 0. \end{aligned} \tag{2.5.65}$$

Next, we seek some simplifications in the case where the function $W \in \mathbb{R} \mapsto \rho_{0W}$ is even. For this purpose, we will need the following lemma about the evenness/oddness of the coefficients a_k, $k = 1, \ldots, 6$ of the corresponding moments m_k.

Lemma 2.5.1. *(i) We have:*

$$\Phi_{-W}(\theta) = \Phi_W(-\theta), \qquad X_{-W}(\theta) = X_W(-\theta), \tag{2.5.66}$$

where Φ_W is defined by (2.4.43) and X_W by (2.6.130).

(ii) The following functions of W are even: $\tilde{c}_1$, λ, a_1, a_2, a_5 (see (2.4.47), (2.6.128), (2.6.131), (2.6.132), (2.6.135) for the definitions of these functions).

(iii) The following functions of W are odd: C, ψ, a_3, a_4, a_6 (see (2.6.103), (2.6.107), (2.6.133), (2.6.134), (2.6.136) for the definitions of these functions).

Proof. (i) We form Eqs. (2.4.43) and (2.6.130) for $\Phi_W(-\theta)$ and $X_W(-\theta)$. By changing W into $-W$, we recover the same equations for $\Phi_{-W}(\theta)$ and $-X_{-W}(\theta)$ respectively, which shows (2.5.66). (ii) and (iii) By (2.4.47) $\tilde{c}_1$ is clearly even. By writing (2.6.103) at $-\theta$ and for $-W$ and using the first equation of (2.5.66), we get that C is odd. Now, using the first equation of (2.5.66) into (2.6.106) and changing θ into $-\theta$, we get that $\Psi_\omega(-W)$ is the symmetric of $\Psi_\omega(W)$ about the line spanned by ω. As an immediate consequence, ψ is even. Changing θ into $-\theta$ in (2.6.128) and using the first equation of (2.5.66), the evenness of $\tilde{c}_1$ and the oddness of ψ, we get that λ is even. By similar considerations, we get that a_1, a_2, a_5 are even and a_3, a_4 and a_6 are odd.

Now, we assume that ρ_{0W} is even with respect to W. Then, $\frac{\tilde{c}_1 \rho_{0W}}{-\mu + i\tilde{c}_1 \xi \cos\theta}$ is also even with respect to W. Therefore, the coefficients m_3, m_4 and $m_6\left[-\frac{\tilde{c}_1 \rho_{0W}}{\mu + i\tilde{c}_1 \xi \cos\theta}\right]$ vanish in (2.5.65), as the result of the integration of an odd coefficient of W against the even function ρ_{0W}. The resulting dispersion relation is written:

$$\mu m_1 + m_2 \xi \cos\theta - m_5 \left[\frac{\tilde{c}_1 \rho_{0W}}{\mu + i\tilde{c}_1 \xi \cos\theta}\right] \xi^2 \sin^2\theta = 0. \tag{2.5.67}$$

We now show that for all $\xi \in \mathbb{R}$ and $\theta \in [0, 2\pi]$, the roots μ of (2.5.67) can only be real, which proves the linearized stability of the system. Indeed, suppose that $\mu = \alpha + i\beta$ with $\alpha, \beta \in \mathbb{R}$, taking the imaginary part of (2.5.67), we get

$$-\beta m_1 - \beta m_5 \left[\frac{\tilde{c}_1 \rho_{0W}}{(-\alpha + \tilde{c}_1 \xi \cos\theta)^2 + \beta^2}\right] \xi^2 \sin^2\theta = 0. \tag{2.5.68}$$

If $\beta \neq 0$, we deduce from (2.5.68) that

$$m_1 = -m_5 \left[\frac{\tilde{c}_1 \rho_{0W}}{(-\alpha + \tilde{c}_1 \xi \cos\theta)^2 + \beta^2}\right] \xi^2 \sin^2\theta. \tag{2.5.69}$$

Numerically, we realize below that the coefficients a_1 and a_5 are non negative (see 2.6). Since we know that $\tilde{c}_1$ is also non negative, (2.5.69) cannot have any root. Thus, $\beta = 0$. We summarize this in the following result.

Proposition 2.5.2. *Consider a uniform steady-state (ρ_{0W}, Ω_0) where $\rho_{0W} \geq 0$ is such that $(1 + |W|)^k \rho_{0W}$ is integrable for k large enough, and where $|\Omega_0| = 1$. We assume that the coefficient a_1 and a_5 given by (2.6.131) and (2.6.135) are positive (and this is verified numerically). If ρ_{0W} is even with respect to W, the SOHPR-L model (2.4.54), (2.4.55) is linearly stable about this steady-state.*

This linear stability result is a first step towards a local-in-time existence result for the full SOHPR-L system. Proving such an existence result is outside the scope of the present paper.

Remark 2.5.1. *in the special cases $\theta = 0$ (the plane-wave perturbation propagates in the same direction as the unperturbed velocity field Ω_0) or $\theta = \frac{\pi}{2}$ (the propagation direction is perpendicular to it), the dispersion relation (2.5.67) can be solved explicitly:*

(i) Case $\theta = 0$. Then the dispersion relation reduces to

$$\mu = \frac{m_2}{m_1}\,\xi.$$

This corresponds to a pure convection wave of Ω in the x-direction. It comes from the convection operator:

$$m_1[\rho_W]\,\Omega_t + m_2[\rho_W]\,(\Omega \cdot \nabla_x)\Omega.$$

(ii) Case $\theta = \frac{\pi}{2}$. Then, the dispersion relation reads:

$$\mu = \left(\frac{m_5[\tilde{c}_1 \rho_{0\Omega}]}{m_1}\right)^{1/2} |\xi$$

This corresponds to acoustic waves propagating symmetrically in both the positive and negative directions. They come from the acoustic operator:

$$m_1[\rho_W]\,\Omega_t + \Omega^{-}\,(\Omega^{\perp} \cdot \nabla_x)\,m_5[\rho_W].$$

2.5.2 Small angular velocity limit of the SOHPR-L model

In this section, we study the asymptotics of the SOHPR-L model (2.4.54), (2.4.55) when the angular velocity is small. For this purpose, we change the scaling $\eta = \varepsilon$ which was made at the beginning of section 2.4 into $\eta = \varepsilon/\zeta$. We first keep $\zeta = \mathcal{O}(1)$ when performing the limit $\varepsilon \to 0$. The resulting model is the SOHPR-L model (2.4.54), (2.4.55), where now, the moments $m_k[\rho_W]$ (see (2.6.137)) and the associated coefficients a_k (see (2.6.131) to (2.6.136)) depend on the parameter ζ. In a second step, we investigate the limit $\zeta \to 0$ in this SOHPR-L model with ζ-dependent coefficients.

First step: limit $\varepsilon \to 0$. Derivation of the SOHPR-L model with ζ-dependent coefficients. Introducing the parameter ζ transforms (2.4.37) into

$$\partial_t f^\varepsilon + \nabla_x \cdot (v f^\varepsilon) - \frac{1}{\zeta}\Big(- \nabla_v \cdot (P_{v^\perp} \omega_{f^\varepsilon}(W)\, f^\varepsilon) \quad \zeta W \nabla_v \cdot (v^\perp f^\varepsilon) + d\Delta_v f^\varepsilon \Big). \tag{2.5.70}$$

It is an easy matter to show that the associated equilibria are of the form $\rho_W \tilde{M}_{\omega_\Omega}(v, \zeta W)$ where ρ_W and Ω are arbitrary and $\tilde{M}_{\omega_\Omega}(v, W)$ is the GVM defined at Definition 2.4.3. In particular, we can write

$$\tilde{M}_{\omega_\Omega}(v, \zeta W) = \Phi_{\zeta W}(\theta), \quad \text{with} \quad \theta = (\widetilde{\omega_\Omega(\zeta W)}\ \tilde{v}). \tag{2.5.71}$$

Similarly, the GCI are of the form $\beta \tilde{\chi}_\Omega(v, \zeta W) + \phi(W)$, where β and ϕ are arbitrary and $\tilde{\chi}_\Omega(v, W)$ is the GCI defined in Prop. 2.6.10. Thus,

$$\tilde{\chi}_\Omega(v, \zeta W) = X_{\zeta W}(\theta), \tag{2.5.72}$$

with the same definition of θ. It follows that $f^0 = \lim_{\varepsilon \to 0} f^\varepsilon$ where f^ε is the solution of (2.5.70) is given by

$$f^0(x, v, W, t) = \rho_W(x, t)\, \tilde{M}_{\omega^\zeta_{\Omega(x,t)}}(v, \zeta W)$$

where

$$\omega_\Omega^\zeta(W) = \omega_\Omega(\zeta W). \tag{2.5.73}$$

The functions $\rho_W(x,t)$ and $\Omega(x,t)$ satisfy the system (2.4.54), (2.4.55), with coefficients c_1^ζ, $m_k^\zeta[\rho_W]$ such that

$$c_1^\zeta(W) = c_1(\zeta W), \quad m_k^\zeta[\rho_W] = \int_{\mathbb{R}^3} a_k(\zeta W)\,\rho_W\,dW, \quad k = 1, \ldots, 6. \tag{2.5.74}$$

Second step: limit $\zeta \to 0$ in the SOHPR-L model with ζ-dependent coefficients. We can now state the following proposition, whose proof can be found in 2.6:

Proposition 2.5.3. *The formal small angular velocity limit $\zeta \to 0$ of the SOHPR-L model (2.4.54), (2.4.55) with ζ-dependent coefficients is the model*

$$\partial_t \rho_W + \nabla_x \cdot (c_1 \rho_W \Omega) = 0, \quad \forall W \in \mathbb{R}, \tag{2.5.75}$$

$$\rho\left(\partial_t \Omega + c_2\,(\Omega \cdot \nabla_x)\Omega\right) + c_5\,P_{\Omega^\perp}\,\nabla_x \rho = 0, \tag{2.5.76}$$

with ρ given by (2.3.29), c_2 by (2.6.100) and c_5 by

$$c_5 = \frac{\int_0^{2\pi} e^{\frac{\cos\theta}{d}} \sin^2\theta\,d\theta}{\int_0^{2\pi} e^{\frac{\cos\theta}{d}} \cos\theta\,d\theta} = \frac{1}{2}\,\frac{I_0\left(\frac{1}{d}\right) - I_2\left(\frac{1}{d}\right)}{I_1\left(\frac{1}{d}\right)} \tag{2.5.77}$$

The same study can be performed in the small angular velocity case. Replacing W by ζW in the kinetic equation (2.3.21) and performing the limit $\varepsilon \to 0$ keeping ζ fixed leads to the SOHPR-S system (2.3.27), (2.3.28) with a factor ζ multiplying the term $Y\Omega^\perp$ in (2.3.28). Therefore, the limit $\zeta \to 0$ in the SOHPR-S system with ζ-dependent parameters is immediate and leads to the system:

$$\partial_t \rho_W + \nabla_x \cdot (c_1 \rho_W \Omega) = 0, \quad \forall W \in \mathbb{R}, \tag{2.5.78}$$

$$\rho\left(\partial_t \Omega + c_2\,(\Omega \cdot \nabla_x)\Omega\right) + d\,P_{\Omega^\perp}\nabla_x \rho = 0, \tag{2.5.79}$$

we see that the structure of this system is the same as that of (2.5.75), (2.5.76). However, the coefficients of the pressure term $P_{\Omega^\perp}\nabla_x\rho$ of the two systems are different. While it is simply the noise coefficient d in the SOHPR-S case, it is equal to a new coefficient c_5 in the SOHPR-L case. Therefore, even for very small angular velocities, the two systems do not coincide. This is due to the different ways of computing the interaction force.

Like in the case of the SOHPR-S model, the density equations (2.5.75) or (2.5.78) can be integrated with respect to W, since c_1 does not depend on W. In both cases, the resulting system is nothing but the standard SOH model (2.3.34), (2.3.35) (see section 2.3). However, again, the coefficients of the pressure term $P_{\Omega^\perp}\nabla_x\rho$ in the velocity eq. (2.3.35) differ. It is indeed equal to d in the case of the SOHPR-S model (2.5.78), (2.5.79), while it is equal to c_5 in the case of the SOHPR-L model (2.5.75), (2.5.76).

Approximation up to $\mathcal{O}(\zeta^2)$ of the SOHPR-L model in the limit $\zeta \to 0$. Proposition 2.5.3 shows that the small angular velocity limit of the SOHPR-L model leads to the standard SOH Model (with slightly modified coefficients) for the total density ρ and velocity direction Ω. Therefore, information about the self-rotation of the particles is lost. Indeed, since the SOH model also describes particles with no self-rotation [29], one cannot distinguish any influence of the particle self-rotation by looking at it. In order to retain some of the influence of the self-rotation of the particles in this limit, it is interesting to compute the first-order correction terms in $\mathcal{O}(\zeta)$. In this way, we will get the corrections to the SOH model induced by the self-rotation. The resulting model is stated in the following proposition, whose proof is sketched in 2.6:

Proposition 2.5.4. *The $\mathcal{O}(\zeta^2)$ approximation of the SOHPR-L model (2.4.54), (2.4.55) with ζ-dependent coefficients, in the limit $\zeta \to 0$, is the model*

$$\partial_t \rho_W + \nabla_x \cdot (c_1 \rho_W \Omega) = 0, \quad \forall W \in \mathbb{R}, \tag{2.5.80}$$

$$\rho \left(\partial_t \Omega + c_2 (\Omega \cdot \nabla_x)\Omega\right) + c_5 P_{\Omega^\perp} \nabla_x \rho + \zeta \rho Y \left(c_3 (\Omega^\perp \cdot \nabla_x)\Omega + c_4 (\nabla_x \cdot \Omega)\Omega^\perp\right) + \zeta c_6 (\Omega \cdot \nabla_x)(\rho Y)\, \Omega^\perp = 0. \tag{2.5.81}$$

with ρ and ρY given by (2.3.29), c_2 by (2.6.100), c_5 by (2.5.77) and $c_k = \frac{a_k^1}{a_1(0)}$, $k = 3, 4, 6$, $a_1(0)$ being given by (2.6.142).

Here, compared to the SOHPR-S system (2.3.27), (2.3.28), the particle self-rotation introduces structurally different terms. In the SOHPR-S system, self-rotation is taken into account through the source term $-Y\Omega^\perp$ in the velocity direction equation (2.3.28). This term corresponds to an acceleration in the direction of the average self-rotation and proportional to it. In the system issued from the SOHPR-L model (2.5.80), (2.5.81), self-rotation introduces differential terms. The first two ones (those multiplied by c_3 and c_4) are proportional to both, the average self-rotation Y and differential terms acting on the velocity direction Ω (namely $(\Omega^\perp \cdot \nabla_x)\Omega$ and $(\nabla_x \cdot \Omega)$). So, in the case of a uniform vector field Ω, these two terms would not induce any acceleration, by contrast to what happens in the SOHPR-S system. The operator $(\Omega^\perp \cdot \nabla_x)\Omega$ produces an acceleration if the vector fields varies in the direction normal to itself. Regions of compression or rarefaction also give rise to an acceleration due to the term $(\nabla_x \cdot \Omega)$. The last term (multiplied by c_6) is proportional to the gradient of the average angular momentum ρY in the direction of Ω. Therefore, variations of the average angular momentum in the direction of the flow produce an acceleration term as well. Again, in the case where ρY is uniform, this acceleration term vanishes, by contrast to what happens in the case of the SOHPR-S system.

One can interpret this difference as follows. In the kinetic equation leading to the SOHPR-L system (2.4.37), the particle acceleration $P_{v^\perp}\omega_{\Omega_f}$ is modified compared to that used in the kinetic equation leading to the SOHPR-S system (2.3.21), namely $P_{v^\perp}\Omega_f$. The use of ω_{Ω_f} instead of Ω_f introduces some kind of compensation for the self rotation $Wv^\perp$ and reduces its influence. This is why, in the hydrodynamic model (2.5.80), (2.5.81), self-rotation appears through differential terms instead of source terms like in the SOHPR-S model. In a spatially homogeneous situation, where ρ and Ω are uniform, the compensation of self-rotation by the use of ω_{Ω_f} in the acceleration is total, and there is no influence of self-rotation in the hydrodynamic model. By contrast, in the SOHPR-S case, even in the spatially homogeneous situation, there cannot be any compensation, and the influence of self-rotation in the hydrodynamic model persists.

2.6 Conclusion and perspectives

In this chapter, we have derived hydrodynamic models for a system of noisy self-propelled particles moving in a plane. The particles are subject to proper rotation on the one hand and interactions with their neighbors through local alignment on the other hand. Two regimes have been investigated. In the small angular velocity regime, the hydrodynamic model consist of a slight modification of the previously obtained Self-Organized Hydrodynamic (SOH) model, including a source term to account for a net average angular velocity. In the large angular velocity regime, after modifying the interaction force to preserve the particle propensity to locally align with their neighbors, the resulting hydrodynamic model involves additional terms accounting for such effects as transport in the normal direction to the velocity and off-diagonal pressure tensor terms. A linearized stability analysis has been performed showing the stability of the model in some particular case. Perspectives include a deeper analytical study of the models, such as proving linearized stability in the general case and local well-posedness of smooth solutions. Numerical simulations will be performed with two purposes. The first one is to validate the hydrodynamic model by comparison to simulations

of the IBM. The second one is to explore what new structures and features are exhibited by these models.

Appendix A Small angular velocity case

In this appendix we shall give a proof of Theorem 2.3.1 involving three steps which are developed in the following sections.

A1 Determination of the equilibria

Thanks to (2.3.21), we have $Q(f^\varepsilon) = \mathcal{O}(\varepsilon)$. Taking the limit $\varepsilon \to 0$ implies $Q(f^0) = 0$. Therefore, f^0 is a so-called equilibrium, i.e. a solution of $Q(f) = 0$. Since Q only operates on the (v, W) variables, we first ignore the spatio-temporal dependence.

Let $\Omega \in \mathbb{S}^1$ be given and define the linear operator

$$\mathcal{Q}_\Omega(f)(v, W) = d\,\nabla_v \cdot \left[M_\Omega(v) \nabla_v \left(\frac{f(v, W)}{M_\Omega(v)} \right) \right].$$

Easy computations[29] show that:

$$Q(f) = \mathcal{Q}_{\Omega_f}(f).$$

We now introduce the functional setting. Let f and g be smooth functions of (v, W) with fast decay when $W \to \pm\infty$. We define the duality products:

$$\langle f, g \rangle_{0,\Omega} := \int_{(v,W)\in\mathbb{S}^1\times\mathbb{R}} f(v, W)\, g(v, W)\, \frac{1}{M_\Omega(v)}\, dv\, dW,$$

$$\langle f, g \rangle_{1,\Omega} = \int_{(v,W)\in\mathbb{S}^1\times\mathbb{R}} \nabla_v \left(\frac{f(v, W)}{M_\Omega(v)} \right) \cdot \nabla_v \left(\frac{g(v, W)}{M_\Omega(v)} \right) M_\Omega(v)\, dv\, dW.$$

Then, $\langle f, g \rangle_{0,\Omega}$ defines a duality (i.e. a continuous bilinear form) between $f \in L^1(\mathbb{R}, L^2(\mathbb{S}^1))$ and $f \in L^\infty(\mathbb{R}, L^2(\mathbb{S}^1))$. Similarly, $\langle f, g \rangle_{1,\Omega}$ defines a duality between $f \in L^1(\mathbb{R}, H^1(\mathbb{S}^1))$ and $f \in L^\infty(\mathbb{R}, H^1(\mathbb{S}^1))$. Thanks to Green's formula applied with smooth functions, we have

$$-\langle \mathcal{Q}_\Omega(f), g \rangle_{0,\Omega} = d \langle f, g \rangle_{1,\Omega} \tag{2.6.82}$$

Therefore, for $f \in L^\infty(\mathbb{R}, L^2(\mathbb{S}^1))$, we define $\mathcal{Q}_\Omega(f)$ as a linear form on $L^\infty(\mathbb{R}, L^2(\mathbb{S}^1))$. Actually, since this linear form is defined and continuous on $C_0^0(\mathbb{R}, L^2(\mathbb{S}^1))$, where C_0^0 denotes the space of continuous functions tending to zero at infinity, $\mathcal{Q}_\Omega(f)$ is a bounded measure on $\mathbb{R}$ with values in $H^1(\mathbb{S}^1)$ but we will not use this characterization. We now define the set of equilibria:

Definition 2.6.1. *The set $\mathcal{E}$ of equilibria of Q is given by*

$$\mathcal{E} = \{ f \in L^1(\mathbb{R}, H^1(\mathbb{S}^1)) \ ; \ f \geq 0 \text{ and } \mathcal{Q}_{\Omega_f}(f) = 0 \}.$$

The characterization of $\mathcal{E}$ is given in the following lemma.

Lemma 2.6.2. *The set $\mathcal{E}$ of equilibria is the set of all functions of the form*

$$v \mapsto \rho_W\, M_\Omega(v), \tag{2.6.83}$$

where the function $W \mapsto \rho_W \in \mathbb{R}_+$ and the vector Ω are arbitrary in the sets $L^1(\mathbb{R})$ and $\mathbb{S}^1$ respectively.

Proof. First, suppose that $f \in \mathcal{E}$. Then, thanks to (2.6.82), we have $0 = -\langle \mathcal{Q}_{\Omega_f}(f), f \rangle_{0,\Omega_f} = d \langle f, f \rangle_{1,\Omega_f}$. It follows that $\nabla_v \left(\frac{f(v,W)}{M_{\Omega_f}} \right) = 0$, i.e. there exists $\rho_W \in \mathbb{R}$, independent of v, such that $f(v, W) = \rho_W\, M_{\Omega_f}$. Additionally, that $f \in L^1(\mathbb{R}, H^1(\mathbb{S}^1))$ and $f > 0$ implies that $\rho_W > 0$ and that the function $W \in \mathbb{R} \to \rho_W \in \mathbb{R}_+$ belongs to $L^1(\mathbb{R})$. Therefore, f is of the form (2.6.83).

Conversely, suppose that f is of the form (2.6.83) with ρ_W as regular as in the lemma. Then, the results follow obviously if we can show that $\Omega_f = \Omega$. But, thanks to (2.3.25), we have $J_{\rho_W M_\Omega} = \int_{W\in\mathbb{R}} \rho_W\, dW\, c_1\, \Omega$, and since $c_1 > 0$ and $\rho_W > 0$, we have $\Omega_{\rho_W M_\Omega} = \Omega$, which shows the result.

From this lemma, and the fact that f^0 is an equilibrium, we deduce that f^0 is given by (2.3.26). Now, $\rho_W = \rho_W(x,t)$ and $\Omega = \Omega(x,t)$ are a priori arbitrary functions of (x,t). Indeed, Q only acts on the (v,W) variables. Hence, the fact that $Q(f^0) = 0$ does not impose any condition on the dependence of f^0 on (x,t). In order to determine how ρ_W and Ω depend on (x,t), we need the second step of the proof, developed in the following section.

A2 Generalized Collision Invariants (GCI)

We first recall the concept of a Collision Invariant.

Definition 2.6.3. *A collision invariant (CI) is a function $\psi \in L^\infty(\mathbb{R}, H^1(\mathbb{S}^1))$ such that for all functions $f \in L^1(\mathbb{R}, H^1(\mathbb{S}^1))$, we have*

$$-\int_{(v,W)\in\mathbb{S}^1\times\mathbb{R}} Q(f)\,\psi\,dv\,dW := d\langle \psi M_{\Omega_f}, f\rangle_{1,\Omega_f} = 0. \tag{2.6.84}$$

We denote by $\mathcal{C}$ the set of CI. The set $\mathcal{C}$ is a vector space.

We first have the obvious result:

Proposition 2.6.4. *Any function $\phi: W \in \mathbb{R} \to \phi(W) \in \mathbb{R}$ belonging to $L^\infty(\mathbb{R})$ is a CI.*

Proof. Let $\phi \in L^\infty(\mathbb{R})$ and $f \in L^1(\mathbb{R}, H^1(\mathbb{S}^1))$. Then, obviously $\phi M_{\Omega_f} \in L^\infty(\mathbb{R}, H^1(\mathbb{S}^1))$ and since ϕ does not depend on v, it satisfies (2.6.84).

We will see that this set of CI does not suffice to provide the spatio-temporal evolution of ρ_W and Ω in the hydrodynamic limit. In the absence of other obvious CI, we introduce a weaker concept, that of 'Generalized Collision Invariant' (GCI). The rationale for introducing this concept is discussed in details in [25, 29].

Definition 2.6.5. *Let $\Omega \in \mathbb{S}^1$ be given. A Generalized Collision Invariant (GCI) associated to Ω is a function $\psi \in L^\infty(\mathbb{R}, H^1(\mathbb{S}^1))$ which satisfies the following property: for all functions $f(v,W)$ such that $f \in L^1(\mathbb{R}, H^1(\mathbb{S}^1))$ and that $P_{\Omega^\perp}\Omega_f = 0$, we have*

$$-\int_{(v,W)\in\mathbb{S}^1\times\mathbb{R}} Q_\Omega(f)\,\psi\,dv\,dW := d\langle \psi M_\Omega, f\rangle_{1,\Omega} = 0 \tag{2.6.85}$$

We denote by $\mathcal{G}_\Omega$ the set of GCI associated to Ω. It is a vector space.

Of course, if $\psi \in L^\infty(\mathbb{R}, H^1(\mathbb{S}^1))$, so does ψM_Ω and (2.6.85) is well-defined. Before determining $\mathcal{G}_\Omega$, we introduce an appropriate functional setting for functions of v only. We consider the space $V_0 = \{\varphi \in H^1(\mathbb{S}^1),\ \int_{v\in\mathbb{S}^1} \varphi(v)\,dv = 0\}$. Let $\Omega \in \mathbb{S}^1$ be given. We define the following norms or semi-norms on $L^2(\mathbb{S}^1)$ and $H^1(\mathbb{S}^1)$ respectively, by:

$$|f|^2_{0,\Omega} := \int_{v\in\mathbb{S}^1} |f(v)|^2 \frac{1}{M_\Omega(v)}\,dv, \qquad |f|^2_{1,\Omega} = \int_{v\in\mathbb{S}^1} \left|\nabla_v\left(\frac{f(v)}{M_\Omega(v)}\right)\right|^2 M_\Omega(v)\,dv.$$

Of course, these two semi-norms are respectively equivalent to the classical L^2 norm and H^1 semi-norm on $L^2(\mathbb{S}^1)$ and $H^1(\mathbb{S}^1)$. We have the following Poincaré inequality:

$$|\varphi|^2_{1,\Omega} \geq C|\varphi|^2_{0,\Omega}, \qquad \forall \varphi \in V_0, \tag{2.6.86}$$

with a positive constant C. We denote by $(f,g)_{0,\Omega}$ and $(f,g)_{1,\Omega}$ the associated bilinear forms.

Proposition 2.6.6. *We have*

$$\mathcal{G}_\Omega = \left\{\beta\chi_\Omega(v) + \phi(W),\quad \beta\in\mathbb{R},\quad \phi\in L^\infty(\mathbb{R})\right\},$$

where $\varphi_\Omega = \chi_\Omega M_\Omega$ is the unique solution in V_0 of the variational formulation

$$\text{Find } \varphi\in V_0 \text{ such that } (\varphi,f)_{1,\Omega} = (\Omega^\perp\cdot v\, M_\Omega, f)_{0,\Omega},\ \forall f\in H^1(\mathbb{S}^1). \tag{2.6.87}$$

Proof. The existence of a unique solution $\varphi_\Omega\in V_0$ of the variational problem (2.6.87) is an easy consequence of Lax-Milgram's theorem and the Poincaré inequality (2.6.86). We refer the reader to [20, 13].

Now, let $\Omega\in\mathbb{S}^1$ be given, $\psi\in\mathcal{G}_\Omega$ and $f\in L^1(\mathbb{R},H^1(\mathbb{S}^1))$. First we note that the condition $P_{\Omega^\perp}J_f = 0$ is equivalent to $P_{\Omega^\perp}J_f = 0$ and can be written

$$\int_{(v,W)\in\mathbb{S}^1\times\mathbb{R}} f\,\Omega^\perp\cdot v\,dv\,dW = 0.$$

or equivalently, $\langle\Omega^\perp\cdot v\, M_\Omega, f\rangle_{0,\Omega} = 0$. Then, by (2.6.85), ψ is a GCI if and only if $\psi\in L^\infty(\mathbb{R},H^1(\mathbb{S}^1))$ and the following implication holds: for all $f\in L^1(\mathbb{R},H^1(\mathbb{S}^1))$,

$$\langle\Omega^\perp\cdot v\, M_\Omega, f\rangle_{0,\Omega} = 0 \qquad\Longrightarrow\qquad \langle f,\psi M_\Omega\rangle_{1,\Omega} = 0.$$

By a standard functional analytic argument, this means that there exists a real number β such that

$$\langle\psi M_\Omega, f\rangle_{1,\Omega} = \beta\,\langle\Omega^\perp\cdot v\, M_\Omega, f\rangle_{0,\Omega},\qquad \forall f\in L^1(\mathbb{R},H^1(\mathbb{S}^1)). \tag{2.6.88}$$

Therefore, ψ is the solution of an elliptic variational problem.

Now, we remark that the function $(v,W)\to\beta\chi_\Omega(v)+\phi(W)$, with $\phi\in L^\infty(\mathbb{R})$ belongs to $L^\infty(\mathbb{R},H^1(\mathbb{S}^1))$ and satisfies the variational problem (2.6.88). These are the only ones. Indeed, by linearity, the difference ψ of two such solutions is an element of $L^\infty(\mathbb{R},H^1(\mathbb{S}^1))$ and satisfies

$$\langle\psi M_\Omega, f\rangle_{1,\Omega} = 0.\qquad \forall f\in L^1(\mathbb{R},H^1(\mathbb{S}^1)).$$

Then, introducing the indicator function $\zeta_A(W)$ of the interval $[-A,A]$, with $A>0$ and taking $f = \psi M_\Omega\zeta_A$ as a test function in $L^1(\mathbb{R},H^1(\mathbb{S}^1))$, we get

$$\int_{(v,W)\in\mathbb{S}^1\times[-A,A]} |\nabla_v\psi|^2\,M_\Omega\,dv\,dW = 0,$$

which implies that ψ does not depend on v and is therefore of the form $\psi(W)$ with $\psi\in L^\infty(\mathbb{R})$. This concludes the proof.

Interpreting the variational problem (2.6.87) in the distributional sense, we see that χ_Ω is a solution of the following elliptic problem:

$$-\nabla_v\cdot(M_\Omega\nabla_v\chi_\Omega) = v\cdot\Omega^\perp M_\Omega,\qquad \int_{v\in\mathbb{S}^1}\chi_\Omega(v)\,M_\Omega(v)\,dv = 0. \tag{2.6.89}$$

Additionally, we can write[43] $\chi_\Omega(v) = g(\theta)$, where $\theta = \widehat{(\Omega,v)}$ and g is the odd 2π-periodic function in $H^1_{\mathrm{loc}}(\mathbb{R})$ (which can be identified to $H^1_0(0,\pi)$) which uniquely solves the problem

$$\frac{d}{d\theta}\left(e^{\frac{\cos\theta}{J}}\,\frac{dg}{d\theta}(\theta)\right) = -\sin\theta\, e^{\frac{\cos\theta}{J}}. \tag{2.6.90}$$

A closed formula for g can be obtained[13]:

$$g(\theta) = d\theta \quad d\pi \frac{\int_0^\theta e^{-\frac{\cos\varphi}{d}}\, d\varphi}{\int_0^\pi e^{-\frac{\cos\varphi}{d}}\, d\varphi}. \tag{2.6.91}$$

Since the function $\frac{g(\theta)}{\sin\theta}$ is even and 2π-periodic, it can be expressed as a function of $\cos\theta$. Thus, we introduce the function h defined on $[-1,1]$ such that

$$h(\cos\theta) = \frac{g(\theta)}{\sin\theta}. \tag{2.6.92}$$

Then, we can write

$$\chi_\Omega(v) = h(\Omega \cdot v)\, \Omega^\perp \cdot v, \tag{2.6.93}$$

and the function h is bounded. We are now well equipped to derive the hydrodynamic limit $\varepsilon \to 0$ of (2.3.21). This is done in the next section.

A3 Hydrodynamic limit $\varepsilon \to 0$

This section is devoted to the proof of Theorem 2.3.1.

Proof of Theorem 2.3.1. We recall that, as a consequence of Lemma 2.6.2 and the fact that $f^0 = \lim_{\varepsilon\to 0} f^\varepsilon$ is an equilibrium, f^0 is given by (2.3.26). In the remainder of the proof, we omit the superscript 0 for the sake of clarity.

We first prove (2.3.27). Taking an arbitrary function $\phi \in L^\infty(\mathbb{R})$, multiplying (2.3.21) by ϕ, integrating with respect to $(v, W) \in \mathbb{S}^1 \times \mathbb{R}$, using the fact that ϕ is a GCI thanks to Proposition 2.6.6 and taking the limit $\varepsilon \to 0$, we get:

$$\int_{W\in\mathbb{R}} \left(\partial_t \rho_W + \nabla_x \cdot (c_1 \rho_W \Omega)\right) \phi(W)\, dW = 0.$$

In the second term, we have used (2.3.25), as well as the definition (2.3.29). Since this equation is valid for any $\phi \in L^\infty(\mathbb{R})$, we immediately deduce (2.3.27).

We now prove (2.3.28). We multiply (2.3.21) by $\chi_{\Omega_{f^\varepsilon}}$ and integrate with respect to v. Since $\chi_{\Omega_{f^\varepsilon}}$ is a GCI associated to Ω_{f^ε} and since f^ε has precisely mean direction Ω_{f^ε}, we have

$$\int_{(v,W)\in\mathbb{S}^1\times\mathbb{R}} Q(f^\varepsilon)\, \chi_{\Omega_{f^\varepsilon}}\, dv\, dW = 0.$$

Then we get

$$\int_{(v,W)\in\mathbb{S}^1\times\mathbb{R}} (\mathcal{T}^1 f^\varepsilon + \mathcal{T}^2 f^\varepsilon)\, \chi_{\Omega_{f^\varepsilon}}\, dv\, dW = 0. \tag{2.6.94}$$

where $\mathcal{T}^k$, $k = 1, 2$ are the following operators:

$$\mathcal{T}^1 f = \partial_t f + \nabla_x \cdot (vf), \qquad \mathcal{T}^2 f = -W \nabla_x \cdot (v^\perp f).$$

Taking the limit $\varepsilon \to 0$ in (2.6.94) and using the fact that $f^\varepsilon \to \rho_W M_\Omega$ we get,

$$\int_{(v,W)\in\mathbb{S}^1\times\mathbb{R}} (\mathcal{T}^1(\rho_W M_\Omega) + \mathcal{T}^2(\rho_W M_\Omega))\, \chi_\Omega\, dv\, dW := T_1 + T_2 = 0, \tag{2.6.95}$$

The contribution of the first term of (2.6.95) has been computed in [32, 43]. Using the expression (2.6.93) of χ_Ω, it leads to

$$T_1 = \Omega^\perp \cdot \int_{W\in\mathbb{R}} \left[\rho_W \left(\frac{\alpha}{d}\, \partial_t \Omega + \gamma(\Omega \cdot \nabla_x)\Omega\right) - \alpha P_{\Omega^\perp} \nabla_x \rho_W\right] dW. \tag{2.6.96}$$

with

$$\alpha = \int_{v\in\mathbb{S}^1} M_\Omega(v)\left(1-(v\cdot\Omega)^2\right)h(v\cdot\Omega)\,dv,$$
$$\gamma = \frac{1}{d}\int_{v\in\mathbb{S}^1} M_\Omega(v)\left(1-(v\cdot\Omega)^2\right)h(v\cdot\Omega)\,\cos(v\cdot\Omega)\,dv.$$

Since α and γ do not depend on W, we can integrate the variable W out and (2.6.96) leads to:

$$T_1 = \Omega^\perp\cdot\Big[\rho\Big(\frac{\alpha}{d}\,\partial_t\Omega+\gamma(\Omega\cdot\nabla_x)\Omega\Big)-\alpha P_{\Omega^\perp}\nabla_x\rho\Big]. \tag{2.6.97}$$

We now turn towards the second term. We have

$$T_2 = \int_{(v,W)\in\mathbb{S}^1\times\mathbb{R}} W\,\nabla_v\cdot\left(v^\perp\rho_W M_\Omega\right)(v\cdot\Omega^\perp)\,h(v\cdot\Omega)\,dv\,dW.$$

Owing to the fact that $\nabla_v\cdot\left(v^\perp M_\Omega\right) = -\frac{v\cdot\Omega^\perp}{d}M_\Omega$, we get

$$T_2 = -\frac{1}{d}\int_{W\in\mathbb{R}} W\,\rho_W\,dW\int_{v\in\mathbb{S}^1} M_\Omega\,(v\cdot\Omega^\perp)^2\,h(v\cdot\Omega)\,dv \tag{2.6.98}$$
$$= \frac{\alpha}{d}V. \tag{2.6.99}$$

Now, collecting (2.6.97) and (2.6.99) and multiplying by $\frac{d}{\alpha}$, we get (2.3.28) with $c_2 = \frac{\gamma d}{\alpha}$, i.e.

$$c_2 = \frac{\int_{v\in\mathbb{S}^1} M_\Omega(v)\left(1-(v\cdot\Omega)^2\right)h(v\cdot\Omega)\,\cos(v\cdot\Omega)\,dv}{\int_{v\in\mathbb{S}^1} M_\Omega(v)\left(1-(v\cdot\Omega)^2\right)h(v\cdot\Omega)\,dv}, \tag{2.6.100}$$
$$= \frac{\int_0^\pi e^{\frac{\cos\theta}{d}}\sin^2\theta\;h(\cos\theta)\,\cos\theta\,d\theta}{\int_0^\pi e^{\frac{\cos\theta}{d}}\sin^2\theta\;h(\cos\theta)\,d\theta}, \tag{2.6.101}$$
$$= \frac{\int_0^\pi e^{\frac{\cos\theta}{d}}\,g(\theta)\,\sin\theta\,\cos\theta\,d\theta}{\int_0^\pi e^{\frac{\cos\theta}{d}}\,g(\theta)\,\sin\theta\,d\theta}, \tag{2.6.102}$$

where we use (2.6.92) in the last equality.

Appendix B Large angular velocity case

This appendix is devoted for the proof of Theorem 2.4.9 which is divided into the same three steps as that of Theorem 2.3.1. However, there are substantial differences and new difficulties which justify why we develop this proof in full detail below.

B1 Determination of the equilibria

We first prove Lemmas 2.4.2 to 2.4.7.

Proof of Lemma 2.4.2. We show the existence and uniqueness of Φ_W. For simplicity, we omit the index W. Defining $G(\theta) = \frac{1}{d}(W-\sin\theta)$, (2.4.43) can be rewritten

$$\Phi' - G\Phi = C, \tag{2.6.103}$$

where C is a constant. This equation can be integrated elementarily on the interval $[0,2\pi[$ and leads to

$$\Phi(\theta) = e^{H(\theta)}\Big(C\int_0^\theta e^{-H(s)}\,ds - D\Big), \quad \theta\in[0,2\pi[,$$

where D is another constant and H is the antiderivative of G which vanishes at 0: $H(\theta) = \frac{1}{d}(W\theta + \cos\theta - 1)$. The constants C and D are determined from the requirement that, on the one hand Φ is 2π-periodic and smooth, hence leading to $\Phi(0) = \Phi(2\pi)$ and on the other hand it is normalized to unity, i.e. $\int_0^{2\pi} \Phi(\theta)\, d\theta = 1$. These two conditions lead to the following linear system for C and D:

$$\begin{cases} e^{H(2\pi)} \int_0^{2\pi} e^{-H(s)}\, ds\ C - \left(e^{H(2\pi)} - 1\right) D = 0, \\ \int_0^{2\pi} e^{H(\theta)} \int_0^{\theta} e^{-H(s)}\, ds\, d\theta\ C + \int_0^{2\pi} e^{H(\theta)}\, d\theta\ D = 1. \end{cases}$$

The determinant Δ of this system can be written

$$\Delta = e^{H(2\pi)} \int_0^{2\pi} e^{H(\theta)} \int_\theta^{2\pi} e^{-H(s)}\, ds\, d\theta + \int_0^{2\pi} e^{H(\theta)} \int_0^{\theta} e^{-H(s)}\, ds\, d\theta,$$

and is clearly strictly positive. Therefore, there exists a unique pair of constants (C, D) which satisfies the required conditions. These constants can be computed readily and are given by:

$$C = \frac{1}{\Delta}\left(e^{H(2\pi)} - 1\right), \qquad D = \frac{1}{\Delta} e^{H(2\pi)} \int_0^{2\pi} e^{-H(s)}\, ds.$$

Then, the solution can finally be written:

$$\Phi(\theta) = \frac{e^{H(\theta)}}{\Delta}\left(e^{H(2\pi)} \int_0^{2\pi} e^{-H(s)}\, ds + \int_0^{\theta} e^{-H(s)}\, ds\right), \quad \theta \in [0, 2\pi[, \tag{2.6.104}$$

and is again, clearly positive. Finally, (2.6.104) shows that the function Φ is smooth, except may be at the cut point $\theta = 0$. However, by using the equation recursively, it is easy to see that $\Phi^{(k)}(2\pi) = \Phi^{(k)}(0)$, showing that Φ defines a function of $C^\infty(\mathbb{S}^1)$. This concludes the proof.

Proof of Lemma 2.4.4. Let $f(v, W)$ be such that $\bar{Q}_\omega f = 0$. Using the angular coordinate $\theta = \widehat{(\omega, v)}$, and writing $f(v, W) = \rho_W \psi_W(\theta)$, with $\rho_W = \int_{v \in \mathbb{S}^1} f(v, W)\, dv$, we find that ψ_W satisfies (2.4.43). Hence, by the uniqueness of the solution of (2.4.43), ψ_W must be equal to Φ_W, leading to the expression (2.4.45). The converse is obvious.

Proof of Lemma 2.4.6. Let $\theta = \widehat{(\omega(W), v)}$. Then, we have:

$$\tilde{c}_1 \omega(W) = \left| \int_0^{2\pi} \Phi_W(\theta)(\cos\theta, \sin\theta)^T\, d\theta \right|, \tag{2.6.105}$$

and is clearly independent of $\omega(W)$.

Proof of Lemma 2.4.7. We compute the components of $\Psi_\omega(W)$ in the basis $(\omega, \omega^\perp)$. We get:

$$\Psi_\omega(W) = \frac{1}{\tilde{c}_1(W)} \int_0^{2\pi} \Phi_W(\theta)(\cos\theta, \sin\theta)^T\, d\theta. \tag{2.6.106}$$

where the exponent 'T' denotes the transpose of a vector or matrix. This expression shows that the angle

$$\psi(W) = \widehat{(\omega(W), \Psi_\omega(W))}, \tag{2.6.107}$$

does not depend on ω and can be computed a priori from the knowledge of Φ_W. Thus, given Ω, if we choose ω such that $\widehat{(\omega(W), \Omega)} = \psi(W)$, $\forall W \in \mathbb{R}$, we get that $\Psi_\omega(W) = \Omega$ and that this is the unique choice of ω which realizes this equality.

Now, we recall that $\tilde{Q}(f)$ is defined by (2.4.40). We turn to the definition and determination of the equilibria of $\tilde{Q}$.

Definition 2.6.7. *The set $\tilde{\mathcal{E}}$ of equilibria of $\tilde{Q}$ is defined by*

$$\tilde{\mathcal{E}} = \left\{ f \in L^1(\mathbb{R}, C^2(\mathbb{S}^1)) \quad f \geq 0 \ \text{ and } \ \tilde{Q}(f) = 0 \right\}.$$

The following proposition characterizes the elements of $\tilde{\mathcal{E}}$:

Proposition 2.6.8. *The set $\tilde{\mathcal{E}}$ is the set of all functions of the form*

$$(v, W) \mapsto \rho_W \tilde{M}_{\omega_\Omega}(v, W), \tag{2.6.108}$$

where the function $W \mapsto \rho_W \in \mathbb{R}_+$ and the vector Ω are arbitrary in $L^1(\mathbb{R})$ and $\mathbb{S}^1$ respectively.

Proof. We first show that all equilibria are necessarily of the form (2.6.108). Indeed, let $f(v, W)$ be such that $\tilde{Q}(f) = 0$. Then, it satisfies $\tilde{\mathcal{Q}}_{\omega_f}(f) = 0$ and is therefore an element of $\tilde{\mathcal{E}}_{\omega_f}$. From Lemma 2.4.4, there exists $\rho_W \geq 0$ such that $f = \rho_W \tilde{M}_{\omega_f}$. But, by Definition 2.1.8, $\omega_f = \omega_{\Omega_f}$. Therefore, there exist Ω (namely Ω_f) such that f is of the form (2.6.108).

Conversely, suppose that f is of the form (2.6.108). By Lemma 2.1.1, $f \in \tilde{\mathcal{E}}_{\omega_\Omega}$. By (2.4.40) Definition 2.4.1 and Definition 2.6.7, we have the equivalence:

$$f \in \tilde{\mathcal{E}} \quad \Longleftrightarrow \quad f \in \tilde{\mathcal{E}}_{\omega_f}.$$

Therefore, to prove that $f \subset \tilde{\mathcal{E}}$, it is sufficient to prove that $\omega_f = \omega_\Omega$. But from (2.6.108), we have

$$J_f = \int_{W \in \mathbb{R}} \rho_W \, c_1(W) \, \Psi_{\omega_\Omega}(W) \, dW.$$

But, with (2.4.48), we deduce that

$$J_f = \int_{W \in \mathbb{R}} \rho_W \, c_1(W) \, dW \, \Omega.$$

and that

$$\Omega_f = \frac{J_f}{|J_f|} = \Omega.$$

Therefore, by (2.4.49), we have $\omega_f = \omega_{\Omega_f} = \omega_\Omega$. This concludes the proof.

B2 Generalized collision invariants

We define the notion of a GCI for the collision operator $\tilde{Q}$:

Definition 2.6.9. *Let $\Omega \in \mathbb{S}^1$ be given. A Generalized Collision Invariant (GCI) associated to Ω is a function $\psi \in L^\infty_{loc}(\mathbb{R}, H^1(\mathbb{S}^1))$ which satisfies the following property:*

$$\int_{(v,W) \in \mathbb{S}^1 \times \mathbb{R}^2} \tilde{\mathcal{Q}}_{\omega_\Omega}(f) \, \psi \, dv \, dW = 0. \quad \forall f \ \text{ such that } \ P_{\Omega^\perp} \Omega_f = 0, \tag{2.6.109}$$

where the integral is understood in the distributional sense. We denote by $\tilde{\mathcal{G}}_\Omega$ the set of GCI associated to Ω. It is a vector space.

The determination of $\tilde{\mathcal{G}}_\Omega$ is performed in the next proposition. We introduce $H^1_0(\mathbb{S}^1) = \{\phi \in H^1(\mathbb{S}^1) \mid \int_{v \in \mathbb{S}^1} \phi(v) \, dv = 0\}$.

Proposition 2.6.10. *We have*

$$\tilde{\mathcal{G}}_\Omega = \{\beta \tilde{\chi}_\Omega(v, W) + \phi(W), \quad \beta \in \mathbb{R}, \quad \phi \in L^\infty_{loc}(\mathbb{R})\}.$$

where for each $W \in \mathbb{R}$, the function $v \in \mathbb{S}^1 \mapsto \tilde{\chi}_\Omega(v, W)$ is the unique solution in $H^1_0(\mathbb{S}^1)$ of the problem

$$d\Delta_v \chi \quad (P_v \omega_\Omega(W) + W v^\perp) \cdot \nabla_v \chi = \Omega^\perp \cdot v. \tag{2.6.110}$$

Proof. The proof starts like that of Prop. 2.6.6. Let $\Omega \in \mathbb{S}^1$ be given. The constraint $P_{\Omega^\perp} \Omega_f = 0$ is a linear constraint on f, which can be written $\int_{(v,W)\in\mathbb{S}^1\times\mathbb{R}} f\, \Omega^\perp \cdot v \, dv\, dW = 0$. By Definition 2.6.9, ψ is a GCI if and only if the following implication holds:

$$\int_{(v,W)\in\mathbb{S}^1\times\mathbb{R}} f\, \Omega^\perp \cdot v \, dv\, dW = 0 \quad \Longrightarrow \quad -\int_{(v,W)\in\mathbb{S}^1\times\mathbb{R}} \tilde{\mathcal{Q}}_{\omega_\Omega}(f)\, \psi \, dv\, dW = 0.$$

which is equivalent to the existence of a real number β such that

$$\int_{(v,W)\in\mathbb{S}^1\times\mathbb{R}} \tilde{\mathcal{Q}}_{\omega_\Omega}(f)\, \psi \, dv\, dW = \beta \int_{(v,W)\in\mathbb{S}^1\times\mathbb{R}} f\, \Omega^\perp \cdot v \, dv\, dW,$$

for all functions f. By introducing the formal L^2 adjoint $\tilde{\mathcal{Q}}^*_{\omega_\Omega}$ of $\tilde{\mathcal{Q}}_{\omega_\Omega}$, this is again equivalent to the problem.

$$\tilde{\mathcal{Q}}^*_{\omega_\Omega} \psi = \beta\, \Omega^\perp \cdot v, \tag{2.6.111}$$

which is nothing but the elliptic problem (2.6.110). We note that the different values of W are decoupled in problem (2.6.110) and that, for any given $W \in \mathbb{R}$, it can be solved as a function of v only. Therefore, from now on, we omit the dependence of ω_Ω in W and simply write it ω

We solve this equation in the space $H^1(\mathbb{S}^1)$ by using a variational formulation. For $\psi, \varphi \in H^1(\mathbb{S}^1)$, we denote by $\ell(\psi, \varphi)$ the bilinear form associated to (2.6.110), i.e.

$$\ell(\psi, \varphi) \quad d \int_{v\in\mathbb{S}^1} \nabla_v \psi \cdot \nabla_v \varphi \, dv \quad \int_{v\in\mathbb{S}^1} \left((\omega + W v^\perp) \cdot \nabla_v \psi\right) \varphi \, dv.$$

The bilinear form ℓ in continuous on $H^1(\mathbb{S}^1)$. By Young's inequality applied to the second term, we have

$$\ell(\varphi, \varphi) \geq \frac{d}{2} \int_{v\in\mathbb{S}^1} \nabla_v \varphi_i{}^2 \, dv - C \int_{v\in\mathbb{S}^1} |\varphi|^2 \, dv,$$

for all $\varphi \in H^1(\mathbb{S}^1)$. Therefore, there exists λ large enough such that the bilinear form

$$a(\psi, \varphi) = \ell(\psi, \varphi) + \lambda \int_{v\in\mathbb{S}^1} \psi\, \varphi \, dv.$$

is coercive on $H^1(\mathbb{S}^1)$. Then, by Lax-Milgram theorem, for all $\zeta \in L^2(\mathbb{S}^1)$ there exists a unique solution $\psi \in H^1(\mathbb{S}^1)$ such that

$$a(\psi, \varphi) = \int_{v\in\mathbb{S}^1} \zeta\, \varphi \, dv, \quad \forall \varphi \in H^1(\mathbb{S}^1). \tag{2.6.112}$$

and the mapping T^λ which to each $\zeta \in L^2(\mathbb{S}^1)$ associates this solution $\psi \in H^1(\mathbb{S}^1)$ is a bounded linear operator. By the compact embedding of $H^1(\mathbb{S}^1)$ into $L^2(\mathbb{S}^1)$, the mapping T^λ is a compact operator of $L^2(\mathbb{S}^1)$.

Now, we specify $\zeta = \zeta_0 := \beta v \cdot \Omega^\perp$. ζ_0 is a function of $L^2(\mathbb{S}^1)$. The variational solution ψ of (2.6.111) can be written:

$$a(\psi, \varphi) = \int_{v \in \mathbb{S}^1} (\zeta_0 + \lambda\psi)\, \varphi \, dv, \quad \forall \varphi \in H^1(\mathbb{S}^1),$$

or equivalently

$$\psi = T^\lambda(\zeta_0 + \lambda\psi).$$

This is a fixed point equation. Changing unknown to $\xi = \zeta_0 + \lambda\psi$, the equation is transformed into

$$(\mathrm{Id} - \lambda T^\lambda)\xi = \zeta_0 \tag{2.6.113}$$

We denote by $\mathrm{Im}(\mathrm{Id} - \lambda T^\lambda)$ and $\mathrm{Ker}(\mathrm{Id} - \lambda T^{\lambda *})$ the image of $\mathrm{Id} - \lambda T^\lambda$ and the kernel of its adjoint respectively (where $T^{\lambda *}$ denotes the adjoint of T^λ). Eq (2.6.113) has a solution if and only if $\zeta_0 \in \mathrm{Im}(\mathrm{Id} - \lambda T^\lambda)$. Since T^λ is compact, we can apply the Fredholm alternative and this condition is equivalent to $\zeta_0 \in \left(\mathrm{Ker}(\mathrm{Id} - \lambda T^{\lambda *})\right)^\perp$.

We show that $\mathrm{Ker}(\mathrm{Id} - \lambda T^{\lambda *}) = \mathrm{Span}\{\tilde{M}_\omega\}$, where, by abuse of notation, we denote by $\tilde{M}_\omega$ the function $v \to \tilde{M}_{\omega_\Omega}(v, W)$, for the considered particular value of W. First, $T^{\lambda *}$ is defined as follows: let $\zeta \in L^2(\mathbb{R})$. Then, $\psi = T^{\lambda *}\zeta$ if and only if ψ is the solution of the variational formulation:

$$a(\varphi, \psi) = \int_{v \in \mathbb{S}^1} \zeta\, \varphi \, dv, \quad \forall \varphi \in H^1(\mathbb{S}^1),$$

or equivalently, using Green's formula:

$$d \int_{v \in \mathbb{S}^1} \nabla_v \psi \cdot \nabla_v \varphi \, dv + \int_{v \in \mathbb{S}^1} \nabla_v \cdot \left((\omega + Wv^\perp)\psi\right) \varphi \, dv + \lambda \int_{v \in \mathbb{S}^1} \psi\, \varphi \, dv = - \int_{v \in \mathbb{S}^1} \zeta\, \varphi \, dv, \quad \forall \varphi \in H^1(\mathbb{S}^1). \tag{2.6.114}$$

When $\zeta = \tilde{M}_\omega$, we see that this variational formulation is solved with $\psi = \frac{1}{\lambda}\tilde{M}_\omega$. This is due to the fact that, by construction, $\tilde{M}_\omega$ cancels the first two terms of (2.6.114). Therefore, $T^{\lambda *}\tilde{M}_\omega = \frac{1}{\lambda}\tilde{M}_\omega$, or $(\mathrm{Id} - \lambda T^{\lambda *})\tilde{M}_\omega = 0$. Thus $\mathrm{Span}\{\tilde{M}_\omega\} \subset \mathrm{Ker}(\mathrm{Id} - \lambda T^{\lambda *})$. Reciprocally, let $\mu \in \mathrm{Ker}(\mathrm{Id} - \lambda T^{\lambda *})$. Then $T^{\lambda *}\mu = \frac{1}{\lambda}\mu$. Inserting $\psi = \frac{1}{\lambda}\mu$ and $\zeta = \mu$ in (2.6.114), we see that μ satisfies

$$d \int_{v \in \mathbb{S}^1} \nabla_v \mu \cdot \nabla_v \varphi \, dv + \int_{v \in \mathbb{S}^1} \nabla_v \cdot \left((\omega + Wv^\perp)\mu\right) \varphi \, dv = 0, \quad \forall \varphi \in H^1(\mathbb{S}^1),$$

which is the weak formulation of:

$$d\Delta_v \mu - \nabla_v \cdot \left((P_{v^\perp} \cdot \omega_\Omega(W) + Wv^\perp)\mu\right) = 0.$$

By Lemma 2.4.4, we know that the only solutions to this equation are proportional to $\tilde{M}_\omega$. This shows that $\mathrm{Ker}(\mathrm{Id} - \lambda T^{\lambda *}) \subset \mathrm{Span}\{\tilde{M}_\omega\}$ and finally proves the identity of these two spaces.

Now, (2.6.113) has a solution if and only if $\zeta_0 \in \left(\mathrm{Span}\{\tilde{M}_\omega\}\right)^\perp$. We compute:

$$\begin{aligned} \int_{v \in \mathbb{S}^1} \zeta_0(v)\, \tilde{M}_\omega(v)\, dv &= \beta\, \Omega^\perp \cdot \int_{v \in \mathbb{S}^1} v M_{\omega_\Omega}(v, W)\, dv \\ &= \beta\, \tilde{c}_1(W)\, \Omega^\perp \Psi_{\omega_\Omega}(W) \\ &= 0, \end{aligned}$$

by virtue of (2.4.48). Consequently, there exists a solution in $H^1(\mathbb{S}^1)$ to (2.6.113).

Now, the Fredholm theory also tells that $\dim(\mathrm{Ker}(\mathrm{Id} - \lambda T^\lambda)) = \dim(\mathrm{Ker}(\mathrm{Id} - \lambda T^{\lambda *})) = 1$, where dim stands for the dimension of a space. But, we easily see that the constants belong to

$\mathrm{Ker}(\mathrm{Id} - \lambda T^\lambda)$. Indeed, $\psi = \frac{1}{\lambda}$ solves the variational formulation (2.6.112) for $\zeta = 1$. Therefore, $T^\lambda 1 = \frac{1}{\lambda}$ and $(\mathrm{Id} - \lambda T^\lambda)1 = 0$. It follows that $\mathrm{Ker}(\mathrm{Id} - \lambda T^\lambda) = \mathrm{Span}\{1\}$. Therefore, the general solution of (2.6.113) is obtained from any particular solution by adding an arbitrary constant. We can select a unique solution, denoted by ψ_β by imposing the extra constraint that $\int_{v\in\mathbb{S}^1} \psi_\beta\, dv = 0$. We realize that $\psi_\beta = \beta\psi_1$ (which follows easily from the uniqueness).

Now, we construct the function $\tilde\chi_\Omega(v, W)$ such that for all $W \in \mathbb{R}$, the function $v \mapsto \tilde\chi_\Omega(v, W)$ coincides with the function ψ_1 obtained by the construction above for the considered value of W. This function is a solution of (2.6.111) with $\beta = 1$. We obtain a solution of (2.6.111) for an arbitrary β by taking $\beta\tilde\chi_\Omega(v, W)$. Now, suppose that there are two solutions of (2.6.111) for the same value of β. The difference is a solution of (2.6.111) for $\beta = 0$. We obtain such solutions by following the same steps above, except that the right-hand side ζ_0 is now equal to 0. The corresponding changed unknown ξ solves the homogeneous version of (2.6.113), i.e. is an element of $\mathrm{Ker}(\mathrm{Id} - \lambda T^\lambda)$. Therefore, ξ is a constant in v, and so is ψ. When restoring the dependence in W, this means that the solutions of (2.6.111) for $\beta = 0$ consist of the functions of W only. Therefore, any solution of (2.6.111) is written $\beta\tilde\chi_\Omega(v, W) + \phi(W)$, with an arbitrary function $\phi(W)$. Since β is any real number, the set of GCI is spanned by such elements when $\beta \in \mathbb{R}$ and the function $\phi(W)$ are arbitrary. This is what is stated in Proposition 2.6.10, and ends the proof.

B3 Hydrodynamic limit $\varepsilon \to 0$

This section is devoted to the proof of Theorem 2.4.9.

Proof of Theorem 2.4.9. The beginning of the proof is analogous to that of Theorem 2.3.1. Let f^ε be a solution of (2.4.37) with ω_{f^ε} given by (2.4.19). Thanks to Proposition 2.6.8, there exist two functions $\rho_W(x,t)$ and $\Omega(x,t)$ where, for fixed (x,t), the function $W \to \rho_W(x,t)$ and the vector $\Omega(x,t)$ belong to $L^1(\mathbb{R})$ and $\mathbb{S}^1$ respectively, such that (2.4.53) holds. The derivation of (2.1.54) is also similar as in the proof of Theorem 2.3.1.

We concentrate on the proof of (2.4.55). We omit the superscript 0 on f^0 for the sake of clarity. Again, the beginning of the proof is similar and we end up getting

$$\int_{(v,W)\in\mathbb{S}^1\times\mathbb{R}} \mathcal{T}(\rho_W \tilde M_{\omega_\Omega})\, \tilde\chi_\Omega\, dv\, dW = 0, \tag{2.6.115}$$

with $\mathcal{T} = \partial_t + v\cdot\nabla_x$. We compute:

$$\mathcal{T}(\rho_W \tilde M_{\omega_\Omega}) = \tilde M_{\omega_\Omega}\{A_\rho + \rho_W A_\Omega\}. \tag{2.6.116}$$

where, using (2.1.54),

$$\begin{aligned} A_\rho &= \mathcal{T}\rho_W = (\partial_t + \tilde c_1\Omega\cdot\nabla_x)\rho_W + (v - \tilde c_1\Omega)\cdot\nabla_x\rho_W \\ &= -\tilde c_1\rho_W(\nabla_x\cdot\Omega) + (v - \tilde c_1\Omega)\cdot\nabla_x\rho_W, \end{aligned} \tag{2.6.117}$$

and $A_\Omega = \mathcal{T}\ln\tilde M_{\omega_\Omega}$ i.e.

$$A_\Omega(x,t) = \left.\frac{\partial \ln\tilde M_{\omega_\Omega}}{\partial\Omega}\right|_{\Omega(x,t)} \mathcal{T}\Omega(x,t). \tag{2.6.118}$$

The quantity $\frac{\partial\ln\tilde M_{\omega_\Omega}}{\partial\Omega}|_\Omega$ is a linear form acting on the tangent line to $\mathbb{S}^1$ at Ω. By the chain rule:

$$\left.\frac{\partial \ln\tilde M_{\omega_\Omega}}{\partial\Omega}\right|_\Omega = \left.\frac{\partial \ln\tilde M_\omega}{\partial\omega}\right|_{\omega_\Omega} \left.\frac{\partial\omega_\Omega}{\partial\Omega}\right|_\Omega, \tag{2.6.119}$$

where $\frac{\partial\ln\tilde M_\omega}{\partial\omega}_{\omega_\Omega}$ is a linear form acting on the tangent line to $\mathbb{S}^1$ at ω_Ω and $\frac{\partial\omega_\Omega}{\partial\Omega}|_\Omega$ is a linear application from the tangent line to $\mathbb{S}^1$ at Ω into the tangent line to $\mathbb{S}^1$ at ω_Ω. We compute the

first factor. Since $\ln \tilde{M}_\omega = \ln \Phi_W(\theta)$ with $\theta = \widehat{(\omega, v)}$ and Φ_W given at Lemma 2.4.2, we can write, thanks to (2.6.103):

$$\begin{aligned} \frac{\partial \ln \tilde{M}_\omega}{\partial \omega}\Big|_\omega \tau &= \frac{\partial \ln \Phi_W}{\partial \theta}\Big|_{\widehat{(\omega,v)}} \frac{\partial \widehat{(\omega, v)}}{\partial \omega}\Big|_\omega \tau \\ &= \Big(\frac{1}{d}(\omega^\perp \cdot v - W) - \frac{C}{\tilde{M}_\omega} \Big)\, \omega^\perp \cdot \tau, \end{aligned} \tag{2.6.120}$$

for all tangent vectors τ to $\mathbb{S}^1$ at ω. We now compute the second factor. We differentiate relation (2.4.48) with respect to Ω and we get that

$$\frac{\partial \omega_\Omega}{\partial \Omega}\Big|_\Omega = \Big(\frac{\partial \Psi_\omega}{\partial \omega}\Big|_{\omega_\Omega} \Big)^{-1}. \tag{2.6.121}$$

Let τ be a tangent vector to $\mathbb{S}^1$ at ω. We have, using Lemma 2.4.6 and Eqs. (2.4.46), (2.6.120),

$$\begin{aligned} \frac{\partial \Psi_\omega}{\partial \omega}\Big|_\omega \tau &= \frac{1}{\tilde{c}_1} \frac{\partial u_\omega}{\partial \omega}\Big|_\omega \tau \\ &= \frac{1}{\tilde{c}_1} \int_{v \in \mathbb{S}^1} \Big(\frac{\partial \tilde{M}_\omega}{\partial \omega}\Big|_\omega \tau \Big)\, v\, dv \\ &= \frac{1}{\tilde{c}_1} \int_{v \in \mathbb{S}^1} \Big(\frac{1}{d}(\omega^\perp \cdot v - W)\, \tilde{M}_\omega - C \Big)\, v\, dv\, \omega^\perp \cdot \tau \\ &= \frac{1}{d\,\tilde{c}_1} \int_{v \in \mathbb{S}^1} (\omega^\perp \cdot v - W)\, \tilde{M}_\omega\, v\, dv\, \omega^\perp \cdot \tau, \end{aligned} \tag{2.6.122}$$

where the term in factor of C vanishes by oddness considerations. Now, we note that

$$\int_{v \in \mathbb{S}^1} (\omega^\perp \cdot v - W)\, \tilde{M}_\omega\, v \cdot \Psi_\omega\, dv = 0. \tag{2.6.123}$$

Indeed, differentiating the equation $|u_\omega| = \tilde{c}_1$ with respect to ω, we get

$$\begin{aligned} 0 = \frac{\partial |u_\omega|}{\partial \omega}\Big|_\omega \tau &= \Psi_\omega \cdot \frac{\partial u_\omega}{\partial \omega}\Big|_\omega \tau \\ &= \Psi_\omega \cdot \int_{v \in \mathbb{S}^1} \Big(\frac{\partial \tilde{M}_\omega}{\partial \omega}\Big|_\omega \tau \Big)\, v\, dv \\ &= \frac{1}{d} \int_{v \in \mathbb{S}^1} (\omega^\perp \cdot v - W)\, \tilde{M}_\omega\, (v \cdot \Psi_\omega)\, dv\, \omega^\perp \cdot \tau, \end{aligned}$$

which implies (2.6.123). Then, decomposing $v = (v \cdot \Psi_\omega)\Psi_\omega + (v \cdot \Psi_\omega^\perp)\Psi_\omega^\perp$, (2.6.122) leads to

$$\frac{\partial \Psi_\omega}{\partial \omega}\Big|_\omega \tau = \frac{1}{d\,\tilde{c}_1} \int_{v \in \mathbb{S}^1} (\omega^\perp \cdot v - W)\, \tilde{M}_\omega\, (v \cdot \Psi_\omega)\, dv\, (\omega^\perp \cdot \tau)\, \Psi_\omega^\perp \tag{2.6.124}$$

$$= \lambda\, (\omega^\perp \cdot \tau)\, \Psi_\omega^\perp, \tag{2.6.125}$$

with

$$\lambda = \frac{1}{d\,\tilde{c}_1} \int_{v \in \mathbb{S}^1} (\omega^\perp \cdot v)\, (\Psi_\omega^\perp \cdot v)\, \tilde{M}_\omega\, dv,$$

using that the second term in (2.6.124) vanishes, thanks to the definition of Ψ_ω. Now, using (2.6.121) and (2.6.125), we get, for all tangent vector $\bar{\tau}$ to $\mathbb{S}^1$ at Ω

$$\frac{\partial \omega_\Omega}{\partial \Omega}\Big|_\Omega \bar{\tau} = \frac{1}{\lambda} (\Omega^\perp \cdot \bar{\tau})\, \omega^\perp. \tag{2.6.126}$$

Then, inserting (2.6.120) and (2.6.126) into (2.6.119), we get, for all tangent vector $\bar{\tau}$ to $\mathbb{S}^1$ at Ω

$$\frac{\partial \ln \tilde{M}_{\omega_\Omega}}{\partial \Omega}\Big|_\Omega \bar{\tau} = \frac{1}{\lambda}\Big(\frac{1}{d}(\omega_\Omega^{\perp}\cdot v - W) - \frac{C}{\tilde{M}_{\omega_\Omega}}\Big)\Omega^{\perp}\cdot\bar{\tau}, \tag{2.6.127}$$

with

$$\lambda = \frac{1}{d\tilde{c}_1}\int_{v\in\mathbb{S}^1}(\omega_\Omega^{\perp}\cdot v)(\Omega^{\perp}\cdot v)\tilde{M}_{\omega_\Omega}\,dv.$$

We note that $\lambda = \lambda(W)$ only depends on W. Indeed, introducing $\theta = \widehat{(\omega_\Omega, v)}$ and $\psi(W) = \widehat{(\omega_\Omega, \Omega)}$, we can write

$$\lambda(W) = \frac{1}{d\tilde{c}_1(W)}\int_0^{2\pi}\sin\theta\,\sin(\theta-\psi(W))\,\Phi_W(\theta)\,d\theta, \tag{2.6.128}$$

which clearly defines a function of W only.

Inserting (2.6.127) into (2.6.118) and collecting it with (2.6.117) to insert it into (2.6.116), we get

$$\begin{aligned}\mathcal{T}(\rho_W\tilde{M}_\Omega) = \tilde{M}_{\omega_\Omega}\Big\{&-\tilde{c}_1(W)\,\rho_W\,(\nabla_x\cdot\Omega) + (v-\tilde{c}_1(W)\,\Omega)\cdot\nabla_x\rho_W\\ &+\frac{\rho_W}{\lambda(W)}\Big(\frac{1}{d}(\omega_\Omega^{\perp}\cdot v - W) - \frac{C(W)}{\tilde{M}_{\omega_\Omega}}\Big)\,\Omega^{\perp}\cdot(\partial_t + v\cdot\nabla_x)\Omega\Big\}\end{aligned}$$

which can be rewritten, by decomposing $v = (v\cdot\Omega)\Omega + (v\cdot\Omega^{\perp})\Omega^{\perp}$:

$$\begin{aligned}\mathcal{T}(\rho_W\tilde{M}_\Omega) = &-\tilde{c}_1(W)\,\rho_W\,\tilde{M}_{\omega_\Omega}\;\nabla_x\cdot\Omega + (v\cdot\Omega-\tilde{c}_1(W))\,\tilde{M}_{\omega_\Omega}\;\Omega\cdot\nabla_x\rho_W\\ &+(v\cdot\Omega^{\perp})\,\tilde{M}_{\omega_\Omega}\;\Omega^{\perp}\cdot\nabla_x\rho_W + \frac{\rho_W}{\lambda(W)}\Big(\frac{1}{d}(\omega_\Omega^{\perp}\cdot v - W)\,\tilde{M}_{\omega_\Omega} - C(W)\Big)\;\partial_t\Omega\cdot\Omega^{\perp}\\ &+\frac{\rho_W}{\lambda(W)}\Big(\frac{1}{d}(\omega_\Omega^{\perp}\cdot v - W)\,\tilde{M}_{\omega_\Omega} - C(W)\Big)(v\cdot\Omega)\;(\Omega\cdot\nabla_x)\Omega\cdot\Omega^{\perp}\\ &+\frac{\rho_W}{\lambda(W)}\Big(\frac{1}{d}(\omega_\Omega^{\perp}\cdot v - W)\,\tilde{M}_{\omega_\Omega} - C(W)\Big)(v\cdot\Omega^{\perp})\;(\Omega^{\perp}\cdot\nabla_x)\Omega\cdot\Omega^{\perp}\end{aligned} \tag{2.6.129}$$

Now, we define the following quantities:

$$\begin{aligned}a_1 &= \frac{1}{\lambda(W)\,d}\int_{v\in\mathbb{S}^1}(\omega_\Omega^{\perp}\cdot v - W)\,\tilde{M}_{\omega_\Omega}\,\tilde{\chi}_\Omega(v,W)\,dv,\\ a_2 &= \frac{1}{\lambda(W)\,d}\int_{v\in\mathbb{S}^1}(\omega_\Omega^{\perp}\cdot v - W)(v\cdot\Omega)\,\tilde{M}_{\omega_\Omega}\,\tilde{\chi}_\Omega(v,W)\,dv\\ &\qquad -\frac{C(W)}{\lambda(W)}\int_{v\in\mathbb{S}^1}(v\cdot\Omega)\,\tilde{\chi}_\Omega(v,W)\,dv,\\ a_3 &= \frac{1}{\lambda(W)\,d}\int_{v\in\mathbb{S}^1}(\omega_\Omega^{\perp}\cdot v - W)(v\cdot\Omega^{\perp})\,\tilde{M}_{\omega_\Omega}\,\tilde{\chi}_\Omega(v,W)\,dv\\ &\qquad -\frac{C(W)}{\lambda(W)}\int_{v\in\mathbb{S}^1}(v\cdot\Omega^{\perp})\,\tilde{\chi}_\Omega(v,W)\,dv,\\ a_4 &= \tilde{c}_1(W)\int_{v\in\mathbb{S}^1}\tilde{M}_{\omega_\Omega}(v,W)\,\tilde{\chi}_\Omega(v,W)\,dv,\\ a_5 &= \int_{v\in\mathbb{S}^1}(v\cdot\Omega^{\perp})\,\tilde{M}_{\omega_\Omega}\,\tilde{\chi}_\Omega(v,W)\,dv,\\ a_6 &= \int_{v\in\mathbb{S}^1}(v\cdot\Omega - \tilde{c}_1(W))\,\tilde{M}_{\omega_\Omega}\,\tilde{\chi}_\Omega(v,W)\,dv.\end{aligned}$$

From (2.6.110), the function $\tilde{\chi}_\Omega(v,W)$ can be written $\tilde{\chi}_\Omega(v,W) = X_W(\theta)$, with $\theta = \widehat{(\omega_\Omega, v)}$ and X_W the unique 2π-periodic solution of

$$-X''_W + (\sin\theta - W)X'_W - \sin(\theta - \psi(W)), \qquad \int_0^{2\pi} X_W(\theta)\,d\theta = 0, \tag{2.6.130}$$

with $\psi(W) = \widehat{(\omega_\Omega, \Omega)}$. Therefore, the quantities a_1 through a_6 can be written:

$$a_1 = \frac{1}{\lambda(W)\,d}\int_0^{2\pi} (\sin\theta - W)\,\Phi_W(\theta)\,X_W(\theta)\,d\theta. \tag{2.6.131}$$

$$a_2 = \frac{1}{\lambda(W)\,d}\int_0^{2\pi} (\sin\theta - W)\cos(\theta - \psi(W))\,\Phi_W(\theta)\,X_W(\theta)\,d\theta, \\ -\frac{C(W)}{\lambda(W)}\int_0^{2\pi} \cos(\theta - \psi(W))\,X_W(\theta)\,d\theta. \tag{2.6.132}$$

$$a_3 = \frac{1}{\lambda(W)\,d}\int_0^{2\pi} (\sin\theta - W)\sin(\theta - \psi(W))\,\Phi_W(\theta)\,X_W(\theta)\,d\theta, \\ -\frac{C(W)}{\lambda(W)}\int_0^{2\pi} \sin(\theta - \psi(W))\,X_W(\theta)\,d\theta, \tag{2.6.133}$$

$$a_4 = -\tilde{c}_1(W)\int_0^{2\pi} \Phi_W(\theta)\,X_W(\theta)\,d\theta. \tag{2.6.134}$$

$$a_5 = \int_0^{2\pi} \sin(\theta - \psi(W))\,\Phi_W(\theta)\,X_W(\theta)\,d\theta, \tag{2.6.135}$$

$$a_6 = \int_0^{2\pi} \Big(\cos(\theta - \psi(W)) - \tilde{c}_1(W)\Big)\Phi_W(\theta)\,X_W(\theta)\,d\theta. \tag{2.6.136}$$

We notice that they depend only on W and we shall denote them by $a_k(W)$, $k = 1,\dots,6$. We now define the following moments of ρ_W:

$$m_k[\rho_W] = \int_{w\in\mathbb{R}} a_k(W)\,\rho_W\,dW, \quad k = 1,\dots,6. \tag{2.6.137}$$

With these definitions, we can multiply (2.6.129) by $\chi_\Omega\Omega^-$ and integrate the resulting expression on $(v,W)\in\mathbb{S}^1\times\mathbb{R}$. Thanks to (2.6.115), we get (2.4.55), which ends the proof of Theorem 2.4.9.

Appendix C Small angular velocity limit of the SOHPR-L model. Proofs

C1 Proof of Proposition 2.5.3

We first need to let $\zeta > 0$ in the coefficients (2.5.74) of the SOHPR-L model. For this, we need the following lemma:

Lemma 2.6.11. *(i) For fixed W, the functions Φ_W and X_W respectively given by (2.4.43) and (2.6.130) are such that*

$$\Phi_{\zeta W}(\theta) = \Phi_0(\theta) + \zeta W\Phi_1(\theta) + \mathcal{O}(\zeta^2),\ X_{\zeta W}(\theta) = X_0(\theta) + \zeta W X_1(\theta) + \mathcal{O}(\zeta^2), \tag{2.6.138}$$

where Φ_0, X_1 are even and X_0, Φ_1 are odd functions of θ. Furthermore, we have

$$\Phi_0(\theta) = M_\Omega(v) = \frac{1}{Z_d}e^{\frac{\tau v\cdot\ell}{\eta}}, \qquad X_0(\theta) = \chi_\Omega(v) = g(\theta), \tag{2.6.139}$$

where $\theta = \widehat{(\Omega, v)}$, $M_\Omega(v)$ *and* $\chi_\Omega(v)$ *are the VMF distribution (2.3.24) and the GCI (2.6.89) associated to the small angular velocity case,* g *is given by (2.6.90) or (2.6.91) and* Z_d *is the normalization factor (2.3.24) .*

(ii) We have

$$\tilde{c}_1(\zeta W) = \tilde{c}_1(0) + \mathcal{O}(\zeta^2), \quad \tilde{c}_1(0) = \int_0^{2\pi} \Phi_0(\theta) \cos\theta \, d\theta = c_1. \tag{2.6.140}$$

$$\lambda(\zeta W) = \lambda(0) + \mathcal{O}(\zeta^2), \quad \lambda(0) = \frac{1}{d\, c_1} \int_0^{2\pi} \Phi_0(\theta) \sin^2\theta \, d\theta, \tag{2.6.141}$$

$$a_1(\zeta W) = a_1(0) + \mathcal{O}(\zeta^2), \quad a_1(0) = \frac{1}{d\,\lambda(0)} \int_0^{2\pi} \Phi_0(\theta)\, X_0(\theta) \sin\theta \, d\theta, \tag{2.6.142}$$

$$a_2(\zeta W) = a_2(0) - \mathcal{O}(\zeta^2), \quad a_2(0) = \frac{1}{d\,\lambda(0)} \int_0^{2\pi} \Phi_0(\theta)\, X_0(\theta) \cos\theta \sin\theta \, d\theta, \tag{2.6.143}$$

$$a_5(\zeta W) = a_5(0) + \mathcal{O}(\zeta^2), \quad a_5(0) = d\,\lambda(0) a_1(0). \tag{2.6.144}$$

where c_1 *is the order parameter of the VMF distribution in the small angular case, given by (2.3.25).*

Proof of Lemma 2.6.11. Changing W into ζW into (2.5.66) and inserting expansions (2.6.138), we immediately get that Φ_0, X_1 are even and X_0, Φ_1 are odd functions of θ.

Now, changing W into ζW into (2.4.43) and again inserting the expansion (2.6.138), we get that Φ_0 is a smooth periodic solution of

$$\Phi_0'' + \frac{1}{d}(\sin\theta\, \Phi_0)' = 0, \qquad \int_0^{2\pi} \Phi_0(\theta)\, d\theta = 1.$$

Such a solution is unique and given by the first eq. (2.6.139). Inserting expansion (2.6.138) into (2.6.105) gives (2.6.140).

Before expanding $X_W(\theta)$, we need to expand $\psi(\zeta W) = \widehat{(\omega_\Omega^\zeta(W), \Omega)}$. We have, by (2.5.73) and (2.4.48),

$$\psi(\zeta W) = \widehat{(\omega_\Omega(\zeta W), \Omega)} = \widehat{(\omega_\Omega(\zeta W), \Psi_{\omega_\Omega}(\zeta W))} = \widehat{(\omega, \Psi_\omega(\zeta W))}.$$

The last equality comes from the fact that $\psi(W)$ does not depend on the particular choice of $\omega(W)$. Then, inserting expansion (2.6.138) into (2.6.106) and using the evenness of Φ_0 and the oddness of Φ_1, we get

$$\Psi_\omega(\zeta W) = \omega + \frac{\beta}{c_1} \zeta W \omega^\perp + \mathcal{O}(\zeta^2), \qquad \beta = \int_0^{2\pi} \Phi_1(\theta) \sin\theta \, d\theta.$$

It follows that

$$\psi(\zeta W) = \frac{\beta}{c_1} \zeta W + \mathcal{O}(\zeta^2). \tag{2.6.145}$$

We deduce that the right-hand side of (2.6.130) (with W changed into ζW) can be expanded into:

$$\sin(\theta + \psi(\zeta W)) - \sin\theta = \frac{\beta}{c_1} \zeta W \cos\theta + \mathcal{O}(\zeta^2). \tag{2.6.146}$$

Now, inserting (2.6.138) into (2.6.130) (with W changed into ζW), we find that $X_0(\theta)$ is a smooth periodic solution of

$$-X_0'' + \frac{1}{d} \sin\theta\, X_0' = \sin\theta, \qquad \int_0^{2\pi} X_0(\theta)\, d\theta = 0.$$

Now, by comparing with (2.6.89), we realize that the second relation (2.6.139) holds.

Now, inserting the expansions (2.6.138), (2.6.140) and (2.6.145) successively into (2.6.128) and (2.6.131), (2.6.132), (2.6.135), we get (2.6.141), (2.6.142), (2.6.143), (2.6.144), which ends the proof of the Lemma.

End of proof of Proposition 2.5.3. Since a_3, a_4 and a_6 are even functions of W, the expansion $a_k(\zeta W) = \mathcal{O}(\zeta)$ for $k = 3, 4, 6$, when $\zeta \to 0$ holds. Therefore, in this limit, $m_k^\zeta[\rho_W] \to 0$ for $k = 3, 4, 6$. Now, using (2.6.142), (2.6.143), (2.6.144), we have $m_k^\zeta[\rho_W] \to a_k(0)\,\rho$, with ρ given by (2.3.29). This leads to:

$$\rho\, a_1(0)\partial_t\Omega + \rho\, a_2(0)\,(\Omega\cdot\nabla_x)\Omega + a_5(0)\,P_{\Omega^\perp}\nabla_x\rho = 0.$$

Dividing by $a_1(0)$, we get (2.5.76) with the coefficients c_2 and c_5 given by:

$$c_2 = \frac{a_2(0)}{a_1(0)}, \qquad c_5 = \frac{a_5(0)}{a_1(0)}. \tag{2.6.147}$$

Now, using (2.6.142), (2.6.143), (2.6.144) together with (2.6.139), we notice that the first eq. (2.6.147) is nothing but (2.6.100), while the second eq. (2.6.147) can be recast into (2.5.77). Finally, Eq. (2.5.75) directly follows from (2.4.54) and (2.6.140). This ends the proof of Proposition 2.5.3.

C2 Proof of Proposition 2.5.4

To compute the order $\mathcal{O}(\zeta)$ terms in the expansion of the SOHPR-L model when $\zeta \to 0$, we need to complement Lemma 2.6.11 by information about the first-order corrections to the terms a_3, a_4 and a_6 (see (2.6.133), (2.6.134), (2.6.136)). This is the purpose of the following lemma:

Lemma 2.6.12. *(i) The perturbations Φ_1 and X_1 are the unique smooth 2π periodic solutions to the problems*

$$\Phi_1'' + \frac{1}{d}(\sin\theta\,\Phi_1)' = \frac{1}{d}\Phi_0', \qquad \int_0^{2\pi}\Phi_1(\theta)\,d\theta = 0, \tag{2.6.148}$$

$$X_1'' - \frac{1}{d}\sin\theta\,X_1' = -\frac{X_0'}{d} - \frac{\beta}{c_1}\cos\theta, \qquad \int_0^{2\pi}\Phi_1(\theta)\,d\theta = 0. \tag{2.6.149}$$

We have the expansions:

$$a_3(\zeta W) = a_3^1\,\zeta\,W + \mathcal{O}(\zeta^3),$$

$$a_3^1 = \frac{1}{d\,\lambda(0)}\int_0^{2\pi}\Big[-\sin\theta\,\Phi_0\,X_0\big(1+\frac{\beta}{c_1}\big) + \sin^2\theta\,(\Phi_0 X_1 + \Phi_1 X_0)\Big]\,d\theta \tag{2.6.150}$$

$$a_4(\zeta W) = a_4^1\,\zeta\,W + \mathcal{O}(\zeta^3), \quad a_4^1 = c_1\int_0^{2\pi}(\Phi_0 X_1 + \Phi_1 X_0)\,d\theta, \tag{2.6.151}$$

$$a_6(\zeta W) = a_6^1\,\zeta\,W + \mathcal{O}(\zeta^3), \quad a_6^1 = \int_0^{2\pi}(\cos\theta - c_1)\,(\Phi_0 X_1 + \Phi_1 X_0)\,d\theta, \tag{2.6.152}$$

Proof of Lemma 2.6.12. Eqs. (2.6.148) and (2.6.149) follow easily from (2.4.43) and (2.6.130) (changing W into ζW and expanding up to second order in ζ). Then, from (2.6.103) and (2.5.66), we find that the constant $C(W)$ is odd with respect to W. Therefore, $C(\zeta W)$ is expanded in ζ according to $C(W) = C_1\,\zeta\,W$, where the expression of the constant C_1 can be obtained from Φ_0, Φ_1 but will not be needed. Indeed, in the expansion of $a_3(\zeta W)$, the term containing C has non contribution by oddness with respect to θ. The other term can be expanding using the auxiliary computations already done in the proof of Lemma 2.6.11. They lead to the expressions (2.6.150), (2.6.151), (2.6.152).

Once Lemma 2.6.12 is proved, the proof of Proposition 2.5.4 is straighforward and left to the reader.

Appendix D Graphical representations

In this appendix, we provide some graphical representations of the equilibrium GVM distribution, of the GCI and of the coefficients $a_1 \ldots a_6$ of the large angular rotation case. Fig. 2.1 provides the Generalized von Mises-Fisher (GVM) distribution $M_\omega(v, W)$ (2.4.44) as a function of the angle $\theta = (\widehat{\omega_\Omega, v})$, i.e. the function $\Phi_W(\theta)$ defined at Def. 2.4.2. Fig. 2.2 provides the Generalized Collision Invariant (GCI) $\chi_\Omega(v, W)$ defined at Prop. 2.6.10 as a function of the angle $\theta = (\widehat{\omega_\Omega, v})$, i.e. the function $X_W(\theta)$ defined by (2.6.130). The GCI have been scaled to present similar maxima and be more easily compared (in other words, the function represented is $\beta X_W(\theta)$ for some value of the scaling parameter β ; we notice that the final SOHPR-L model is independent of the use of $\beta X_W(\theta)$ instead of $X_W(\theta)$, as the GCI form a vector space). The GVM and GCI are represented for three values of the noise parameter: $d = 0.2$ (Fig. 2.1a and 2.2a), $d = 1$ (Fig. 2.1b and 2.2b) and $d = 5$ (Fig. 2.1c and 2.2c). In each figure, four values of the angular velocity W are represented: $W = 0$ (blue curve), $W = 1$ (red curve), $W = 5$ (green curve) and $W = 20$ (magenta curve).

On Fig. 2.1, we observe that the GVM have Gaussian shapes which become more uneven with maxima drifting towards the right when the angular velocity W increases. As W becomes large (see the magenta curves corresponding to $W = 20$), the GVM becomes close to a uniform distribution, and the difference to the uniform distribution seems close to an odd function. The influence of W is stronger when the noise parameter d is small. Indeed, comparing the blue and red curves respectively corresponding to $W = 0$ and $W = 1$, we observe a fairly large difference in the case $d = 0.2$ (Fig. 2.1a) while the difference is tiny in the case $d = 5$ (Fig. 2.1c). In particular, we observe that the position of the peak is strongly drifted towards the right in the case $d = 0.2$ (Fig. 2.1a) and to a lesser extent, in the case $d = 1$ (Fig. 2.1b). The drift of the peak towards the right shows that the angle $\vartheta(W) = (\widehat{\omega_\Omega(W), \Omega})$ can be significant. For instance, here, in the case $d = 0.2$ (Fig. 2.1a), we see that this angle is about 1 radian (if we estimate it as the position of the peak). As expected, the width of the peak increases with the noise parameter d.

On Fig. 2.2, we notice that the GCI are close to odd functions of θ and are rigorously odd functions in the case $W = 0$. The influence of increasing values of W is similar as for the GVM, with a deformation of the GCI towards the right (compare the cases $W = 0$ (blue curve) and $W = 1$ (red curve) for the noise parameter $d = 0.2$ (Fig. 2.2a)). The influence of W is less pronounced for increasing values of d, with almost no difference between the cases $W = 0$ (blue curve) and $W = 1$ (red curve) for the noise parameter $d = 5$ (Fig. 2.2c). When both W and d are small, the GCI have sharp variations around $\theta = +\pi$ and smoother variation around $\theta = 0$ (see the cases $W = 0$ (blue curve) for $d = 0.2$ (Fig. 2.2a)). When either d or W increases, the GCI becomes closer and closer to the sine function.

Finally, on Fig. 2.3, the coefficients a_1 through a_6 as functions of W in the range $W \in [0, 10]$ are represented. Again, three values of the noise parameter d are investigated: $d = 0.2$ (red dots), $d = 1$ (blue stars), $d = 5$ (black diamonds). As announced in Prop. 2.5.2, we realize that a_1 and a_3 are positive. We also observe that a_1 through a_4 are quite small for large values of d (see the case $d = 5$) and that a_1, a_3 and a_5 seem to converge to 0 as $W \to \infty$. By contrast, a_2 and a_4 seem to have a linear behavior as $W \to \infty$, while a_6 seems to converge to a non-zero value. Finally, as expected, the range of variation of the parameters as a function of W is narrower in the low noise case ($d = 0.2$) than in the large noise case ($d = 5$). All these observations need to be confirmed by theoretical investigations, which will be developed in future work.

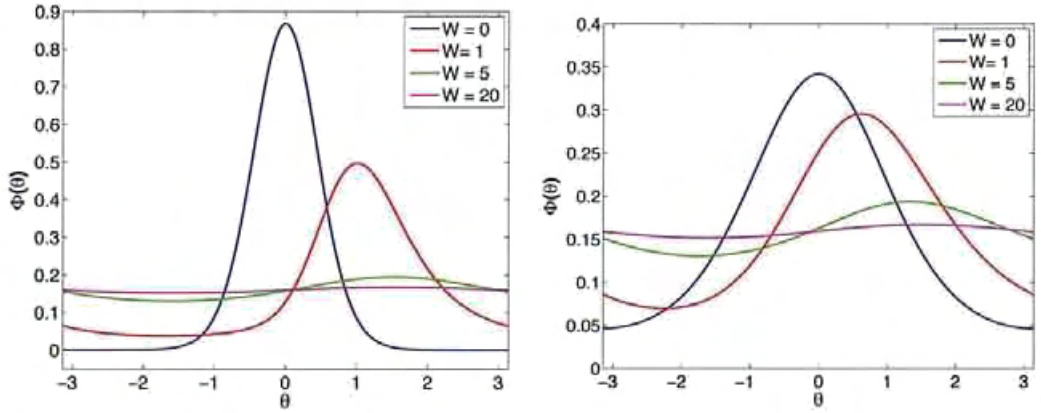

(a) d=0.2 (b) d=1

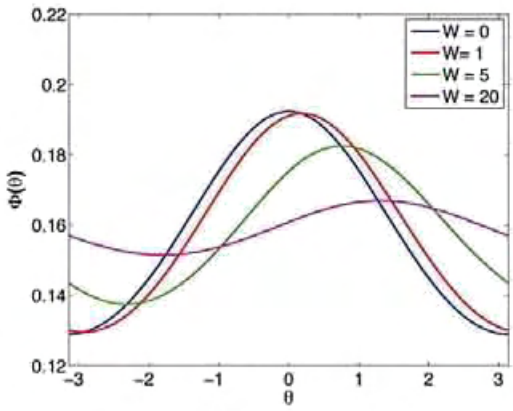

(c) d=5

Figure 2.1: (Color online) The Generalized von Mises-Fisher (GVM) $\Phi_W(\theta)$ as a function of θ for three values of the noise parameter: $d = 0.2$ (Fig. 2.1a), $d = 1$ (Fig. 2.1b) and $d = 5$ (Fig. 2.1c). In each figure, four values of the angular velocity W are represented: $W = 0$ (blue curve), $W = 1$ (red curve), $W = 5$ (green curve) and $W = 20$ (magenta curve).

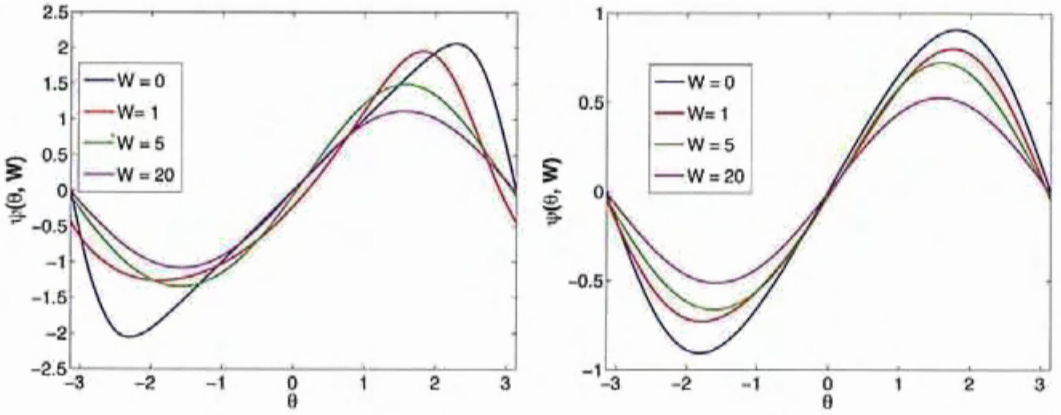

(a) d=0.2

(b) d=1

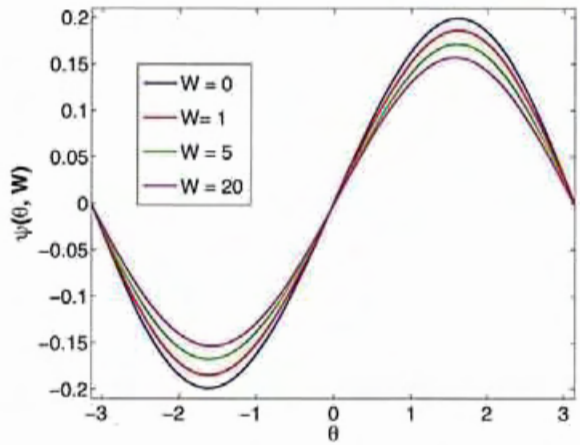

(c) d=5

Figure 2.2: (Color online) The generalized collision invariant $\beta X_W(\theta)$ as a function of θ for three values of the noise parameter: $d = 0.2$ (Fig. 2.2a), $d = 1$ (Fig. 2.2b) and $d = 5$ (Fig. 2.2c). In each figure, four values of the angular velocity W are represented: $W = 0$ (blue curve), $W = 1$ (red curve), $W = 5$ (green curve) and $W = 20$ (magenta curve). The scaling parameter β is adjusted in such a way that the maxima of the various curves have similar orders of magnitude, for an easier comparison.

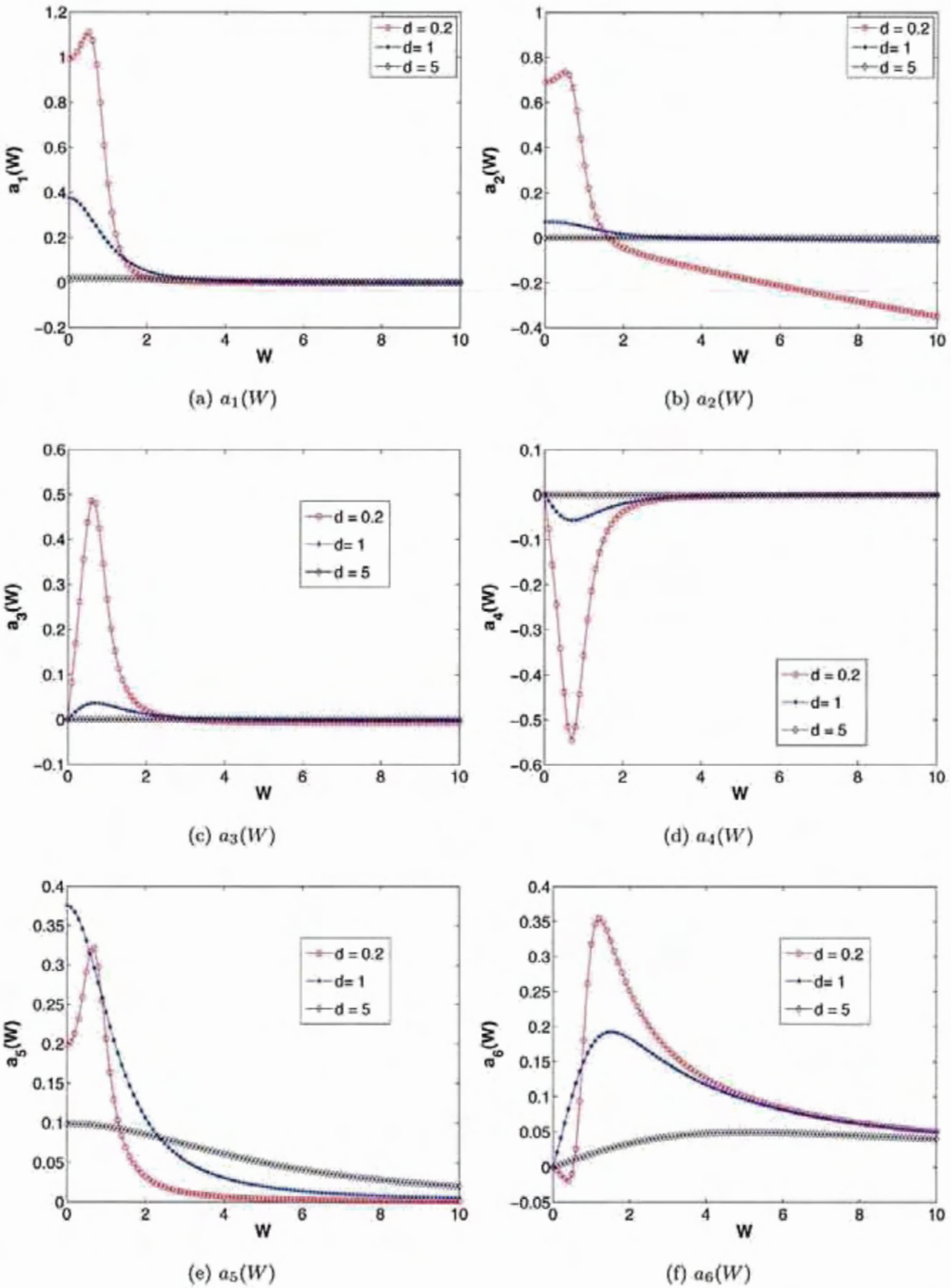

(a) $a_1(W)$ (b) $a_2(W)$

(c) $a_3(W)$ (d) $a_4(W)$

(e) $a_5(W)$ (f) $a_6(W)$

Figure 2.3: (Color online) The coefficients a_1 (Fig. 2.3a), a_2 (Fig. 2.3b), a_3 (Fig. 2.3c), a_4 (Fig. 2.3d), a_5 (Fig. 2.3e), a_6 (Fig. 2.3f) as functions of the angular velocity W. Three values of the noise parameter d are shown: $d = 0.2$ (red dots), $d = 1$ (blue stars), $d = 5$ (black diamonds).

Part II: The Vicsek Model with Repulsion

Chapter 3

A macroscopic model for a system of self-propelled particles with alignment and repulsion

This chapter is a joint work with P. Degond, G. Dimarco, N. Wang. The paper has been accepted to be published on Communications in Mathematical Sciences (CMS). The idea of constructing the model is due to Pr. Degond. I was in charge of the passage from microscopic model to macroscopic model while Wang took care of numerical simulations for the particle model. Thank to constant help from Pr Degond and Pr. Dimarco, Wang and I have also been working together on the code for the macroscopic model. By using these codes, I have done numerical tests in section 3.4 (of course with helps from Degond and Giacomo)

3.1 Introduction

The study of collective motion in systems consisting of a large number of agents, such as bird flocks, fish schools, suspensions of active swimmers (bacteria, sperm cells), etc has triggered an intense literature in the recent years. We refer to [94, 63] for recent reviews on the subject. Many of such studies rely on a particle model or Individual Based Model (IBM) that describes the motion of each individual separately (see e.g in [3, 16, 19, 20, 21, 58, 69, 72, 87]).

In this work, we aim to describe dense suspensions of elongated self-propelled particles in a fluid, such as sperm In such dense suspensions, steric repulsion is an essential ingredient of the dynamics. A large part of the literature is concerned with dilute suspensions [59, 63, 74, 82, 96]. In these approaches, the Stokes equation for the fluid is coupled to the orientational distribution function of the self-propelled particles. However, these approaches are of "mean-field type" i.e. assume that particle interactions are mediated by the fluid through some kinds of averages. These approaches do not deal easily with short-range interactions such as steric repulsion or interactions mediated by lubrication forces. Additionally, these models assume a rather simple geometry of the swimmers, which are reduced to a force dipole, while the true geometry and motion of an actual swimmer, like a sperm cell, is considerably more complex

In a recent work [75], Peruani et al showed that, for dense systems of elongated self-propelled particles, the steric interaction results in alignment. Relying on this work, and owing to the fact that the description of swimmers interactions from first physical principles is by far too complex, we choose to replace the fluid-mediated interaction by a simple alignment interaction of the Vicsek type [93]. In the Vicsek model, the agents move with constant speed and attempt to align with their neighbors up to some noise. Many aspects of the Vicsek model have been studied, such as phase

transitions [2, 16, 24, 27, 52, 93], numerical simulations [71], derivation of macroscopic models [9, 29].

The alignment interaction acting alone may trigger the formation of high particle concentrations. However, in dense suspensions, volume exclusion prevent such high densities to occur. When distances between particles become too small, repulsive forces are generated by the fluid or by the direct reaction of the bodies one to each other. These forces contribute to repel the particles and to prevent further contacts. To model this behavior, we must add a repulsive force to the Vicsek alignment model. Inspired by [6, 58, 87] we consider the possibility that the particle orientations (i.e the directions of the self-propulsion force) and the particle velocities may be different. Indeed, steric interaction may push the particles in a direction different from that of their self-propulsion force.

We consider an overdamped regime in which the velocity is proportional to the force through a mobility coefficient. The overdamped limit is justified by the fact that the background fluid is viscous and thus the forces due to friction are very large compared to those due to motion. Indeed, for micro size particles, the Reynolds number is very small ($\sim 10^{-4}$) and thus the effect of inertia can be neglected. Finally, differently from [6, 58, 87] we consider an additional term describing the relaxation of the particle orientation towards the direction of the particle velocity. We also take into account a Brownian noise in the orientation dynamics of the particles. This noise may take into account the fluid turbulence for instance. Therefore, the particle dynamics results from an interplay between relaxation towards the mean orientation of the surrounding particles, relaxation towards the direction of the velocity vector and Brownian noise. From now on we refer to the above described model as the Vicsek model with repulsion.

Starting from the above described microscopic dynamical system we successively derive mean-field equations and hydrodynamic equations. Mean field equations are valid when the number of particles is large and describe the evolution of the one-particle distribution, i.e. the probability for a particle to have a given orientation and position at a given instant of time. Expressing that the spatio-temporal scales of interest are large compared to the agents' scales leads to a singular perturbation problem in the kinetic equation. Taking the hydrodynamic limit, (i.e. the limit of the singular perturbation parameter to zero) leads to the hydrodynamic model. Hydrodynamic models are particularly well-suited to systems consisting of a large number of agents and to the observation of the system's large scale structures. Indeed, the computational cost of IBM increases dramatically with the number of agents, while that of hydrodynamic models is independent of it. With IBM, it is also sometimes quite cumbersome to access observables such as order parameters, while these quantities are usually directly encoded into the hydrodynamic equations.

The derivation of hydrodynamic models has been intensely studied by many authors. Many of these models are based on phenomenological considerations [91] or derived from moment approaches and ad-hoc closure relations [6, 9, 79]. The first mathematical derivation of a hydrodynamic system for the Vicsek model has been proposed in [29]. We refer to this model to as the Self-Organized Hydrodynamic (SOH) model. One of the main contributions of [29] is the concept of "Generalized Collision Invariants" (GCI) which permits the derivation of macroscopic equations for a particle system in spite of its lack of momentum conservation. The SOH model has been further refined in [32, 43].

Performing the hydrodynamic limit in the kinetic equations associated to the Vicsek model with repulsion leads to the so-called "Self-Organized Hydrodynamics with Repulsion" (SOHR) system. The SOHR model consists of a continuity equation for the density ρ and an evolution equation for the average orientation $\Omega \in \mathbb{S}^{n-1}$ where n indicates the spatial dimension. The average orientation of the fluid at (x,t) represents the total sum of the particles orientations in a small volume around x at time t, normalized to unit norm. More precisely, the model reads

$$\partial_t \rho + \nabla_x \cdot (\rho U) = 0, \tag{3.1.1}$$

$$\rho \partial_t \Omega + \rho (V \cdot \nabla_x)\Omega - P_{\Omega^\perp} \nabla_x p(\rho) = \gamma P_{\Omega^\perp} \Delta_x (\rho \Omega), \tag{3.1.2}$$

$$|\Omega| = 1. \tag{3.1.3}$$

where

$$U - c_1 v_0 \Omega \quad \mu\Phi_0 \nabla_x \rho, \quad V = c_2 v_0 \Omega \cdot \mu\Phi_0 \nabla_\perp \rho, \tag{3.1.4}$$

$$p(\rho) \text{ -- } v_0 d\rho \text{ I } \alpha\mu\Phi_0\big((n-1)d + c_2\big)\frac{\rho^2}{2}, \quad \gamma = k_0\big((n \quad 1)d \text{ I } c_2\big). \tag{3.1.5}$$

The coefficients c_1, c_2, v_0, μ, Φ_0, d, α, k_0 are associated to the microscopic dynamics and will be defined later on. The symbol $P_{\Omega^\perp}$ stands for the projection matrix

$$P_{\Omega^\perp} = \mathrm{Id} - \Omega \otimes \Omega.$$

of $\mathbb{R}^n$ on the hyperplane $\Omega^\perp$. The SOHR model is similar to the SOH model obtained in [32], but with several additional terms which are consequences of the repulsive force at the particle level. The repulsive force intensity is characterized by the parameter $\mu\Phi_0$. In the case $\mu\Phi_0 = 0$, the SOHR system is reduced to the SOH one.

We first briefly describe the original SOH model. Inserting (3.1.4), (3.1.5) with $\mu\Phi_0 = 0$ into (3.1.1), (3.1.2) leads to

$$\partial_t \rho + c_1 v_0 \nabla_x \cdot (\rho\Omega) = 0, \tag{3.1.6}$$

$$\rho\partial_t \Omega + c_2 v_0 \rho(\Omega \cdot \nabla_x)\Omega \text{ I } v_0 d P_{\Omega^\perp} \nabla_x \rho = \gamma P_{\Omega^\perp} \Delta_x(\rho\Omega), \tag{3.1.7}$$

together with (3.1.3). This model shares similarities with the isothermal compressible Navier-Stokes (NS) equations. Both models consist of a non linear hyperbolic part supplemented by a diffusion term. Eq. (3.1.6) expresses conservation of mass, while Eq. (3.1.7) is an equation for the mean orientation of the particles. It is not conservative, contrary to the corresponding momentum conservation equation in NS. The two equations are supplemented by the geometric constraint (3.1.3). This constraint is satisfied at all times, as soon as it is satisfied initially. Indeed, owing to the presence of the projection operator $P_{\Omega^\perp}$, dotting (1.7) with Ω, we get (provided that $\rho \neq 0$)

$$\partial_t |\Omega|^2 \text{ I } c_2 v_0 (\Omega \cdot \nabla_x)\,\Omega|^2 \quad \cdot 0,$$

showing that $|\Omega|^2(x,t) - 1$ for all times as soon as $\Omega|^2(x,0) = 1$ for all x. A second important difference between the SOH model and NS equations is that the convection velocities for the density and the orientation, $v_0 c_1$ and $v_0 c_2$ respectively are different while for NS they are equal. That $c_1 \neq c_2$ is a consequence of the lack of Galilean invariance of the model (there is a preferred frame, which is that of the fluid). The main consequence is that the propagation of sound waves is anisotropic for this type of fluids [91].

The first main difference between the SOH and the SOHR system is the presence of the terms $\mu\Phi_0\nabla_x\rho$ in the expressions of the velocities U and V. Inserting this term in the density Eq. (3.1.1) results in a diffusion-like term $-\mu\Phi_0 \nabla_x \cdot (\rho(\nabla_x \rho))$ which avoids the formation of high particle concentrations. This term shows similarities with the non-linear diffusion term in porous media models. Similarly, inserting the term $\mu\Phi_0\nabla_x\rho$ in the orientation Eq. (3.1.2) results in a convection term in the direction of the gradient of the density. Its effect is to force particles to change direction and move towards regions of lower concentration. The second main difference is the replacement of the linear (with respect to ρ) pressure term $v_0 d P_{\Omega^\perp} \nabla_x \rho$ by a nonlinear pressure $p(\rho)$ in the orientation Eq. (3.1.2). The nonlinear part of the pressure enhances the effects of the repulsion forces when concentrations become high.

To further establish the validity of the SOHR model (3.1.1)-(3.1.5), we perform numerical simulations and compare them to those of the underlying IBM. To numerically solve the SOHR model, we adapt the relaxation method of [71]. In this method, the unit norm constraint (3.1.3) is abandonned and replaced by a fully conservative hyperbolic model in which Ω is supposed to be in $\mathbb{R}^n$. However, at the end of each time step of this conservative model, the vector Ω is normalized. Motsch and Navoret showed that the relaxation method provides numerical solutions of the SOH model which are consistent with those of the particle model. The resolution of the conservative model

can take advantage of the huge literature on the numerical resolution of hyperbolic conservation laws (here specifically, we use [34]). We adapt the technique of [71] to include the diffusion fluxes. Using these approximations, we numerically demonstrate the good convergence of the scheme for smooth initial data and the consistency of the solutions with those of the particle Vicsek model with repulsion.

The outline of the paper is as follows. In section 3.2, we introduce the particle model, its mean field limit, the scaling and the hydrodynamic limit. In Section 3.3, we present the numerical discretization of the SOHR model, while in Section 3.4 we present several numerical tests for the macroscopic model and a comparison between the microscopic and macroscopic models. Section 3.5 is devoted to draw a conclusion. Some technical proofs will be given in the Appendices.

3.2 Model hierarchy and main results

3.2.1 The individual based model and the mean field limit

We consider a system of N-particles each of which is described by its position $X_k(t) \in \mathbb{R}^n$, its velocity $v_k(t) \in \mathbb{R}^n$, and its direction $\omega_k(t) \in \mathbb{S}^{n-1}$, where $k \in \{1, \cdots, N\}$, n is the spatial dimension and $\mathbb{S}^{n-1}$ denotes the unit sphere. The particle ensemble satisfies the following stochastic differential equations

$$\frac{dX_k}{dt} = v_k, \tag{3.2.8}$$

$$v_k = v_0\,\omega_k - \mu\,\nabla_x \Phi(X_k(t), t), \tag{3.2.9}$$

$$d\omega_k = P_{\omega_k^\perp} \circ (\nu\,\bar{\omega}(X_k(t), t)\,dt + \alpha\,v_k\,dt + \sqrt{2D}\,dB_t^k). \tag{3.2.10}$$

Eq. (3.2.8) simply expresses the spatial motion of a particle of velocity v_k. Eq (3.2.9) shows that the velocity v_k is composed of two components: a self-propulsion velocity of constant magnitude v_0 in direction ω_k and a repulsive force proportional to the gradient of a potential $\Phi(x,t)$ with mobility coefficient μ. Equation (3.2.10) describes the time evolution of the orientation. The first term models the relaxation of the particle orientation towards the average orientation $\bar{\omega}(X_k(t),t)$ of its neighbors with rate ν. The second term models the relaxation of the particle orientation towards the direction of the particle velocity v_k with rate α. Finally, the last term describes standard independent white noises dB_t^k of intensity $\sqrt{2D}$. The symbol $\circ$ reminds that the equation has to be understood in the Stratonovich sense. Under this condition and thanks to the presence of $P_{\omega^\perp}$, the orthogonal projection onto the plane orthogonal to ω (i.e $P_{\omega^\perp} = (\mathrm{Id} - \omega \otimes \omega)$, where $\otimes$ denotes the tensor product of two vectors and Id is the identity matrix), the orientation ω_k remains on the unit sphere. We assume that v_0, μ, ν α, D are strictly positive constants.

The repulsive potential $\Phi(x,t)$ is the resultant of binary interactions mediated by the binary interaction potential ϕ. It is given by:

$$\Phi(x,t) = \frac{1}{N}\sum_{i=1}^{N} \phi\Big(\frac{|x - X_i|}{r}\Big) \tag{3.2.11}$$

where the binary repulsion potential $\phi(|x|)$ only depends on the distance. We suppose that $x \mapsto \phi(|x|)$ is smooth (in particular implying that $\phi'(0) = 0$ where the prime denotes the derivative with respect to $|x|$). We also suppose that

$$\phi \geq 0, \qquad \int_{\mathbb{R}^n} \phi(|x|)\,dx < \infty,$$

in particular implying that $\phi(|x|) \to 0$ as $|x| \to \infty$. The quantity r denotes the typical range of ϕ. We consider repulsive potentials i.e.such that $\phi' < 0$. Since $\phi \to 0$ as $|x| \to \infty$, this implies

that $\phi \geq 0$ and that $\Phi_0 = \int \phi(|x|)\,dx > 0$. In the numerical test Section, we will propose precise expressions for this potential force.

The mean orientation $\bar{\omega}(x,t)$ is defined by

$$\bar{\omega}(x,t) = \frac{\mathcal{J}(x,t)}{|\mathcal{J}(x,t)|}, \qquad \mathcal{J}(x,t) = \frac{1}{N}\sum_{i=1}^{N} K\Big(\frac{|x - X_i|}{R}\Big)\omega_i. \tag{3.2.12}$$

It is constructed as the normalization of the vector $\mathcal{J}(x,t)$ which sums up all orientation vectors ω_i of all the particles which belong to the range of the "influence kernel" $K(|x|)$. The quantity $R > 0$ is the typical range of the influence kernel $K(|x|/R)$, which is supposed to depend only on the distance. It measures how the mean orientation at the origin is influenced by particles at position x. Here, we assume that $x \mapsto K(|x|)$ is smooth at the origin and compactly supported. For instance, if K is the indicator function of the ball of radius 1, the quantity $\bar{\omega}(x,t)$ computes the mean direction of the particles which lie in the sphere of radius R centered at x at time t.

Remark 3.2.1. *(i) In the absence of repulsive force (i.e. $\mu = 0$), the system reduces to the time continuous version of the Vicsek model proposed in [29].*
(ii) The model presented is the so called overdamped limit of the model consisting of (3.2.8) and (3.2.10) and where (3.2.9) is replaced by:

$$\epsilon\frac{dv_k}{dt} = \lambda_1(v_0\omega_k - v_k) - \lambda_2\nabla_x\Phi(X_k(t), t). \tag{3.2.13}$$

with $\mu = \lambda_2/\lambda_1$. Taking the limit $\epsilon \to 0$ in (3.2.13), we obtain (3.2.9). As already mentioned in the Introduction, for microscopic swimmers, this limit is justified by the very small Reynolds number and the very small inertia of the particles.

We now introduce the mean field kinetic equation which describes the time evolution of the particle system in the large N limit. The unknown here is the one particle distribution function $f(x,\omega,t)$ which depends on the position $x \in \mathbb{R}^n$, orientation $\omega \in \mathbb{S}^{n-1}$ and time t. The evolution of f is governed by the following system

$$\partial_t f + \nabla_x \cdot (v_f f) + \nu\nabla_\omega \cdot (P_{\omega^\perp}\bar{\omega}_f f) - \alpha\nabla_\omega \cdot (P_{\omega^\perp} v_f f) - D\Delta_\omega f = 0, \tag{3.2.14}$$

$$v_f(x,t) = v_0\omega - \mu\nabla_x\Phi_f(x,t). \tag{3.2.15}$$

where the repulsive potential and the average orientation are given by

$$\Phi_f(x,t) = \int_{\mathbb{S}^{n-1}\times\mathbb{R}^n} \phi\Big(\frac{x-y}{r}\Big)\, f(y,w,t)\,dw\,dy, \tag{3.2.16}$$

$$\bar{\omega}_f(x,\omega,t) = \frac{\mathcal{J}_f(x,t)}{|\mathcal{J}_f(x,t)|}, \tag{3.2.17}$$

$$\mathcal{J}_f(x,t) = \int_{\mathbb{S}^{n-1}\times\mathbb{R}^n} K\Big(\frac{x-y}{R}\Big)\, f(y,w,t)\,w\,dw\,dy \tag{3.2.18}$$

Equation (3.2.14) is a Fokker-Planck type equation. The second term at the left-hand side of (3.2.14) describes particle transport in physical space with velocity v_f and is the kinetic counterpart of Eq. (3.2.8). The third, fourth and fifth terms describe transport in orientation space and are the kinetic counterpart of Eq. (3.2.10). The alignment interaction is expressed by the third term, while the relaxation force towards the velocity v_f is expressed by the fourth term. The fifth term represents the diffusion due to the Brownian noise in orientation space. The projection $P_{\omega^\perp}$ insures that the force terms are normal to ω. The symbols $\nabla_\omega\cdot$ and Δ_ω respectively stand for the divergence of tangent vector fields to $\mathbb{S}^{n-1}$ and the Laplace-Beltrami operator on $\mathbb{S}^{n-1}$. Eq. (3.2.15) is the direct counterpart of (3.2.9).

Eq. (3.2.16) is the continuous counterpart of Eq. (3.2.11). Indeed, letting f be the empirical measure

$$f = \frac{1}{N}\sum_{i=1}^{N} \delta_{(x_i(t),\omega_i(t))}(x,\omega),$$

in (3.2.16) (where $\delta_{(x_i(t),\omega_i(t))}(x,\omega)$ is the Dirac delta at $(x_i(t),\omega_i(t))$) leads to (3.2.11). Similarly, Eqs. (3.2.17), (3.2.18) are the continuous counterparts of (3.2.12) (by the same kind of argument). The rigorous convergence of the particle system to the above Fokker-Planck equation (3.2.14) is an open problem. We recall however that, the derivation of the kinetic equation for the Vicsek model without repulsion has been done in [12] in a slightly modified context.

3.2.2 Scaling

In order to highlight the role of the various terms, we first write the system in dimensionless form. We chose t_0 as unit of time and choose

$$x_0 = v_0 t_0, \qquad f_0 = \frac{1}{x_0^n}, \qquad \phi_0 = \frac{v_0^2 t_0}{\mu},$$

as units of space, distribution function and potential. We introduce the dimensionless variables:

$$\tilde{x} = \frac{x}{x_0}, \qquad \tilde{t} = \frac{t}{t_0}, \qquad \tilde{f} = \frac{f}{f_0}, \qquad \tilde{\phi} = \frac{\phi}{\phi_0}.$$

and the dimensionless parameters

$$\tilde{R} = \frac{R}{x_0}, \qquad \tilde{r} = \frac{r}{x_0}, \qquad \tilde{D} = t_0 D, \qquad \tilde{\nu} = t_0 \nu, \qquad \tilde{\alpha} = \alpha x_0.$$

In the new set of variables $(\tilde{x},\tilde{t})$, Eq. (3.2.15) becomes (dropping the tildes and the $\tilde{}$ for simplicity):

$$v_f = \omega - \nabla_x \Phi_f(x,t),$$

while f, Φ_f, $\bar{\omega}_f$, $\mathcal{J}_f$ are still given by (3.2.15), (3.2.16), (3.2.17), (3.2.18) (now written in the new variables).

We now define the regime we are interested in. We assume that the ranges R and r of the interaction kernels K and ϕ are both small but with R much larger than r. More specifically, we assume the existence of a small parameter $\varepsilon \ll 1$ such that:

$$R = \sqrt{\varepsilon}\hat{R}, \qquad r = \varepsilon \hat{r} \qquad \text{with} \qquad \hat{R}, \hat{r} = \mathcal{O}(1)$$

We also assume that the diffusion coefficient D and the relaxation rate to the mean orientation ν are large and of the same orders of magnitude (i.e. $d = D/\nu = \mathcal{O}(1)$), while the relaxation to the velocity α stays of order 1, i.e.

$$\nu = \frac{1}{\varepsilon}, \qquad d = \frac{D}{\nu} = \mathcal{O}(1), \qquad \alpha = \mathcal{O}(1).$$

With these new notations, dropping all 'hats', the distribution function $f^\varepsilon(x,\omega,t)$ (where the superscript ε now higlights the dependence of f upon the small parameter ε) satisfies the following Fokker-Plank equation

$$\varepsilon\Big(\partial_t f^\varepsilon + \nabla_x \cdot (v_{f^\varepsilon} f^\varepsilon)\Big) - \nabla_\omega \cdot (P_\omega \bar{\omega}_{f^\varepsilon} f^\varepsilon) + \varepsilon\alpha \nabla_\omega \cdot (P_\omega v_{f^\varepsilon} f^\varepsilon) - d\Delta_\omega f^\varepsilon = 0, \tag{3.2.19}$$

$$v_f^\varepsilon = \omega - \nabla_x \Phi_f^\varepsilon(x,t), \tag{3.2.20}$$

where the repulsive potential and the average orientation are now given by

$$\Phi_f^\varepsilon(x,t) = \int_{\mathbb{S}^{n-1}\times\mathbb{R}^n} \phi\Big(\frac{|x-y|}{\varepsilon R}\Big) f^\varepsilon(y,w,t)\,dw\,dy,$$
$$\bar\omega_f^\varepsilon = \frac{\mathcal{J}_f^\varepsilon(x,t)}{|\mathcal{J}_f^\varepsilon(x,t)|}, \quad \mathcal{J}_f^\varepsilon(x,t) = \int_{\mathbb{S}^{n-1}\times\mathbb{R}^n} K\Big(\frac{|x-y|}{\sqrt{\varepsilon}R}\Big) f^\varepsilon(y,w,t)\,w\,dw\,dy$$

Now, by Taylor expansion and the fact that the kernels K, ϕ only depend on $|x|$, we obtain (provided that K is normalized to 1 i.e. $\int_{\mathbb{R}} K(|x|)\,dx = 1$) :

$$v_f^\varepsilon(x,t) = \omega - \Phi_0 \nabla_x \rho_f^\varepsilon + \mathcal{O}(\varepsilon^2), \tag{3.2.21}$$
$$\bar\omega_f^\varepsilon(x,t) = G_f^0(x,t) + \varepsilon G_f^1(x,t) + \mathcal{O}(\varepsilon^2). \tag{3.2.22}$$
$$G_f^0(x,t) = \Omega_f(x,t), \quad G_f^1(x,t) = \frac{k_0}{|J_f|} P_{\Omega_f^\perp} \Delta_x J_f,$$

where the coefficients k_0, Φ_0 are given by

$$k_0 = \frac{R^2}{2n}\int_{x\in\mathbb{R}^n} K(|x|)|x|^2 dx, \quad \Phi_0 = \int_{x\in\mathbb{R}^n} \phi(x)dx. \tag{3.2.23}$$

For example, if K is the indicator function of the ball of radius 1, then $k_0 = |\mathbb{S}^{n-1}|/2n(n-2)$, where $|\mathbb{S}^{n-1}|$ is the volume of the sphere $\mathbb{S}^{n-1}$. In the cases $d=2$ and $d=3$, we respectively get $k_0 = \pi/8$ and $k_0 = 2\pi/15$. The local density ρ_f, the local current density J_f and local average orientation Ω_f are defined by

$$\rho_f(x,t) = \int_{\mathbb{S}^{n-1}} f(x,w,t)\,dw, \tag{3.2.24}$$
$$J_f(x,t) = \int_{\omega\in\mathbb{S}^{n-1}} f(x,w,t)\,w\,dw, \quad \Omega_f(x,t) = \frac{J_f(x,t)}{|J_f(x,t)|}. \tag{3.2.25}$$

More details about this Taylor expansion are given in Appendix A. Let us observe that this scaling, first proposed in [32] is different from the one used in [29] and results in the appearance of the viscosity term at the right-hand side of Eq. (3.1.2).

Finally, if we neglect the terms of order ε^2 and we define the so-called collision operator $Q(f)$ by

$$Q(f) = -\nabla_\omega \cdot (P_{\omega^\perp}\Omega_f f) + d\Delta_\omega f,$$

the rescaled system (3.2.19), (3.2.20) can be rewritten as follows

$$\varepsilon\Big(\partial_t f^\varepsilon + \nabla_x\cdot(v_f^\varepsilon f^\varepsilon) + \alpha\nabla_\omega\cdot(P_{\omega^\perp} v_f^\varepsilon f^\varepsilon) + \nabla_\omega\cdot(P_{\omega^\perp} G_f^1 f^\varepsilon)\Big) = Q(f^\varepsilon), \tag{3.2.26}$$
$$v_{f^\varepsilon}(x,\omega,t) = \omega - \Phi_0\nabla_x\rho_{f^\varepsilon}, \quad G_{f^\varepsilon}^1(x,t) = \frac{k_0}{|J_{f^\varepsilon}|} P_{\Omega_f^\perp}\Delta_x J_{f^\varepsilon} \tag{3.2.27}$$

3.2.3 Hydrodynamic limit

The aim is now to derive a hydrodynamic model by taking the limit $\varepsilon \to 0$ of system (3.2.26), (3.2.27) where the local density ρ_f, the local current J_f and the local average orientation Ω_f are defined by (3.2.24), (3.2.25).

We first introduce the von Mises-Fisher (VMF) probability distribution $M_\Omega(\omega)$ of orientation $\Omega \in \mathbb{S}^{n-1}$ defined for $\omega \in \mathbb{S}^{n-1}$ by:

$$M_\Omega(\omega) = Z^{-1}\exp\Big(\frac{\omega\cdot\Omega}{d}\Big), \qquad Z = \int_{\omega\in\mathbb{S}^{n-1}} \exp\Big(\frac{\omega\cdot\Omega}{d}\Big)\,d\omega$$

An important parameter will be the flux of the VMF distribution, i.e. $\int_{\omega\in\mathbb{S}^{n-1}} M_\Omega(\omega)\omega d\omega$. By obvious symmetry consideration, we have

$$\int_{\omega\in\mathbb{S}^{n-1}} M_\Omega(\omega)\,\omega\,d\omega = c_1\Omega,$$

where the quantity $c_1 = c_1(d)$ does not depend on Ω, is such that $0 \le c_1(d) \le 1$ and is given by

$$c_1(d) = \int_{\omega\in\mathbb{S}^{n-1}} M_\Omega(\omega)\,(\omega\cdot\Omega)\,d\omega. \tag{3.2.28}$$

When d is small, M_Ω is close to a Dirac delta δ_Ω and represents a distribution of perfectly aligned particles in the direction of Ω. When d is large, M_Ω is close to a uniform distribution on the sphere and represents a distribution of almost totally disordered orientations. The function $d \in \mathbb{R}_+ \mapsto c_1(d) \subset [0,1]$ is strictly decreasing with $\lim_{d\to 0} c_1(d) = 1$, $\lim_{d\to\infty} c_1(d) = 0$. Therefore, $c_1(d)$ represents an order parameter, which corresponds to perfect disorder when it is close to 0 and perfect alignment order when it is close to 1.

We have following theorem:

Theorem 3.2.1. *Let f^ε be the solution of (3.2.26), (3.2.27). Assume that there exists f such that*

$$f^\varepsilon \to f \quad as \quad \varepsilon \to 0, \tag{3.2.29}$$

pointwise as well as all its derivatives. Then, there exist $\rho(x,t)$ and $\Omega(x,t)$ such that

$$f(x,\omega,t) = \rho(x,t)M_{\Omega(x,t)}(\omega), \tag{3.2.30}$$

Moreover, the functions $\rho(x,t), \Omega(x,t)$ satisfy the following equations

$$\partial_t\rho + \nabla_x\cdot(\rho U) = 0, \tag{3.2.31}$$

$$\rho\big(\partial_t\Omega - (V\cdot\nabla_x)\Omega\big) + P_{\Omega^\perp}\nabla_x p(\rho) = \gamma P_{\Omega^\perp}\Delta_x(\rho\Omega), \tag{3.2.32}$$

where

$$U = c_1\Omega - \Phi_0\nabla_x\rho, \quad V = c_2\Omega - \Phi_0\nabla_x\rho. \tag{3.2.33}$$

$$p(\rho) = d\rho + \alpha\Phi_0\big((n-1)d + c_2\big)\frac{\rho^2}{2}, \quad \gamma = k_0\big((n-1)d + c_2\big). \tag{3.2.34}$$

and the coefficients c_1, c_2 will be defined in formulas (3.2.28), (3.2.42) below.

Going back to unscaled variables, we find the model (3.1.1)-(3.1.5) presented in the Introduction.

Proof: The proof of this theorem is divided into three steps: (i) determination of the equilibrium states ; (ii) determination of the Generalized Collision Invariants ; (iii) hydrodynamic limit. We give a sketch of the proof for each step.

Step (i): determination of the equilibrium states We define the equilibria as the elements of the null space of Q, considered as an operator acting on functions of ω only.

Definition 3.2.2. *The set $\mathcal{E}$ of equilibria of Q is defined by*

$$\mathcal{E} = \big\{f \in H^1(\mathbb{S}^{n-1}) \mid f \ge 0 \text{ and } Q(f) = 0\big\}.$$

We have the following:

Lemma 3.2.3. *The set $\mathcal{E}$ is given by*

$$\mathcal{E} = \Big\{\rho M_\Omega(\omega) \mid \rho \in \mathbb{R}_-,\ \Omega \in \mathbb{S}^{n-1}\Big\}$$

For a proof of this lemma, see [29]. The proof relies on writing the collision operator as

$$Q(f) = \nabla_\omega \cdot \Big(M_{\Omega_f} \nabla_\omega \big(\frac{f}{M_{\Omega_f}} \big) \Big).$$

Step (ii): Generalized Collision Invariants (GCI). We begin with the definition of a collision invariant.

Definition 3.2.4. *A collision invariant (CI) is a function $\psi(\omega)$ such that for all functions $f(\omega)$ with sufficient regularity we have*

$$\int_{\omega \in \mathbb{S}^{n-1}} Q(f)\, \psi \, d\omega = 0.$$

We denote by $\mathcal{C}$ the set of CI. The set $\mathcal{C}$ is a vector space.

As seen in [29], the space of CI is one dimensional and spanned by the constants. Physically, this corresponds to conservation of mass during particle interactions. Since energy and momentum are not conserved, we cannot hope for more physical conservations. Thus the set of CI is not large enough to allow us to derive the evolution of the macroscopic quantities ρ and Ω. To overcome this difficulty, a weaker concept of collision invariant, the so-called "Generalized collisional invariant" (GCI) has been introduced in [29]. To introduce this concept, we first define the operator $Q(\Omega, f)$, which, for a given $\Omega \in \mathbb{S}^{n-1}$, is given by

$$Q(\Omega, f) = \nabla_\omega \cdot \Big(M_\Omega \nabla_\omega \big(\frac{f}{M_\Omega} \big) \Big).$$

We note that

$$Q(f) = Q(\Omega_f, f), \tag{3.2.35}$$

and that for a given $\Omega \in \mathbb{S}^{n-1}$, the operator $f \mapsto Q(\Omega, f)$ is a linear operator. Then we have the

Definition 3.2.5. *Let $\Omega \in \mathbb{S}^{n-1}$ be given. A Generalized Collision Invariant (GCI) associated to Ω is a function $\psi \in H^1(\mathbb{S}^{n-1})$ which satisfies:*

$$\int_{\omega \in \mathbb{S}^{n-1}} Q(\Omega, f)\, \psi(\omega)\, d\omega = 0, \quad \forall f \in H^1(\mathbb{S}^{n-1}) \quad \text{such that} \quad P_{\Omega^\perp} \Omega_f = 0. \tag{3.2.36}$$

We denote by $\mathcal{G}_\Omega$ the set of GCI associated to Ω

The following Lemma characterizes the set of generalized collision invariants.

Lemma 3.2.6. *There exists a positive function $h : [-1, 1] \to \mathbb{R}$ such that*

$$\mathcal{G}_\Omega = \{ C + h(\omega \cdot \Omega)\beta \cdot \omega \text{ with arbitrary } C \in \mathbb{R} \text{ and } \beta \in \mathbb{R}^n \text{ such that } \beta \cdot \Omega = 0 \}.$$

The function h is such that $h(\cos\theta) = \frac{g(\theta)}{\sin\theta}$ and $g(\theta)$ is the unique solution in the space V defined by

$$V = \{ g \mid (n-2)(\sin\theta)^{\frac{n}{2}-2} g \in L^2(0,\pi), \quad (\sin\theta)^{\frac{n}{2}-1} g \in H_0^1(0,\pi) \}.$$

(denoting by $H_0^1(0,\pi)$ the Sobolev space of functions which are square integrable as well as their derivative and vanish at the boundary) of the problem

$$-\sin^{2-n}\theta\, e^{-\frac{\cos\theta}{d}} \frac{d}{d\theta}\Big(\sin^{n-2}\theta\, e^{\frac{\cos\theta}{d}} \frac{dg}{d\theta}(\theta) \Big) + \frac{n-2}{\sin^2\theta}\, g(\theta) = \sin\theta.$$

The set $\mathcal{G}_\Omega$ is a n-dimensional vector space.

For a proof we refer to [29] for $n = 3$ and to [43] for general $n > 2$. We denote by ψ_Ω the vector GCI

$$\psi_\Omega = h(\omega \cdot \Omega)\, P_{\Omega^\perp}\omega. \tag{3.2.37}$$

We note that, thanks to (3.2.35) and (3.2.36), we have

$$\int_{\omega\in\mathbb{S}^{n-1}} Q(f)\,\psi_{\Omega_f}(\omega)\,d\omega = 0, \quad \forall f \in H^1(\mathbb{S}^{n-1}). \tag{3.2.38}$$

Step (iii): Hydrodynamic limit $\varepsilon \to 0$. In the limit $\varepsilon \to 0$, we assume that (3.2.29) holds. Then, thanks to (3.2.26), we have $Q(f) = 0$. In view of Lemma 3.2.3, this implies that f has the form (3.2.30). We now need to determine the equations satisfied by ρ and Ω.

For this purpose, we divide Eq. (3.2.26) by ε and integrate it with respect to ω. Writing (3.2.26) as

$$(\mathcal{T}_1 + \mathcal{T}_2 + \mathcal{T}_3) f^\varepsilon = \frac{1}{\varepsilon} Q(f^\varepsilon), \tag{3.2.39}$$

where

$$\mathcal{T}_1 f = \partial_t f - \nabla_x \cdot (v_f f), \quad \mathcal{T}_2 f = \alpha \nabla_\omega \cdot (P_{\omega^\perp} v_f\, f), \quad \mathcal{T}_3 f = \nabla_\omega \cdot (P_{\omega^\perp} G_f^1\, f), \tag{3.2.40}$$

we observe that the integral of $\mathcal{T}_2 f^\varepsilon$ and $\mathcal{T}_3 f^\varepsilon$ over ω is zero since it is in divergence form and the integral of the right-hand side of (3.2.39) is zero since 1 is a CI. The integral of $\mathcal{T}_1 f^\varepsilon$ gives

$$\partial_t \rho_{f^\varepsilon} + \nabla_x \cdot \Big(\int_{\mathbb{S}^{n-1}} f^\varepsilon(x,\omega,t)\, v_{f^\varepsilon}(x,\omega,t)\,d\omega \Big) = 0.$$

We take the limit $\varepsilon \to 0$ and use (3.2.29) to get Eq. (3.2.31) with

$$U = \int_{\mathbb{S}^{n-1}} \rho(x,t)\, M_{\Omega(x,t)}(\omega)\, v_{\rho M_\Omega}(x,\omega,t)\,d\omega.$$

Using (3.2.27), we get $v_{\rho M_\Omega}(x,\omega,t) = \omega - \Phi_0 \nabla_x \rho(x,t)$. With (3.2.28), this leads to the first equation (3.2.33).

Multiplying (3.2.39) by $\psi_{\Omega_{f^\varepsilon}}$, integrating with respect to ω and using (3.2.38), we get

$$\int_{\mathbb{S}^{n-1}} (\mathcal{T}_1 + \mathcal{T}_2 + \mathcal{T}_3) f^\varepsilon(x,\omega,t)\, \psi_{\Omega_{f^\varepsilon}}(x,\omega,t)\,d\omega = 0,$$

and taking the limit $\varepsilon \to 0$, we get

$$\int_{\mathbb{S}^{n-1}} ((\mathcal{T}_1 + \mathcal{T}_2 + \mathcal{T}_3)(\rho M_\Omega))(x,\omega,t)\, \psi_{\Omega(x,t)}(\omega)\,d\omega = 0. \tag{3.2.41}$$

This equation describes the evolution of the mean direction Ω. The computations which lead to (3.2.32) are proved in Appendix B. The coefficient c_2 in (3.2.32) is defined by

$$c_2(u) = \frac{\langle \sin^2\theta \cos\theta\, h \rangle_{M_\Omega}}{\langle \sin^2\theta\, h \rangle_{M_\Omega}} = \frac{\int_0^\pi \sin^n\theta \cos\theta\, M_\Omega\, h\,d\theta}{\int_0^\pi \sin^n\theta\, M_\Omega\, h\,d\theta}, \tag{3.2.42}$$

where for any function $g(\cos\theta)$, we denote $\langle g \rangle$ by

$$\langle g \rangle_{M_\Omega} = \int_{\omega\in\mathbb{S}^{n-1}} M_\Omega(\omega)\, g(\omega\cdot\Omega)\,d\omega = \frac{\int_0^\pi g(\cos\theta)\, e^{\frac{\cos\theta}{u}} \sin^{n-2}\theta\,d\theta}{\int_0^\pi e^{\frac{\cos\theta}{u}} \sin^{n-2}\theta\,d\theta}.$$

Remark 3.2.2. *The SOHR model (3.2.31), (3.2.32) can be rewritten as follows*

$$\partial_t \rho + c_1 \nabla_x \cdot (\rho \Omega) = \Phi_0 \Delta_x \left(\frac{\rho^2}{2} \right),$$
$$\partial_t \Omega + (V \cdot \nabla_x)\Omega + P_{\Omega^\perp} \nabla_x h(\rho) \quad \gamma P_{\Omega^-} \Delta_x \Omega,$$

where the vectors $\bar{V}$ and the function $h(\rho)$ are defined by

$$\bar{V} = c_2 \Omega \quad (\Phi_0 + 2\gamma)\nabla_x \rho, \quad h'(\rho) = \frac{1}{\rho} p'(\rho),$$

and where the primes denote derivatives with respect to ρ. This writing displays this system in the form of coupled nonlinear advection-diffusion equations.

3.3 Numerical discretization of the SOHR model

In this section, we develop the numerical approximation of the system (3.2.31)-(3.2.34) in the two dimensional case. As mentioned above, this system is not conservative because of the geometric constraint $|\Omega| = 1$. Weak solutions of non-conservative systems are not unique because jump relations across discontinuities are not uniquely defined. This indeterminacy cannot be waived by means of an entropy inequality, by contrast to the case of conservative systems. In [71] the authors address this problem for the SOH model. They show that the model is a zero-relaxation limit of a conservative system where the velocity Ω is non-constrained (i.e. belongs to $\mathbb{R}^n$). Additionally, they show that the numerical solutions build from the relaxation system are consistent with those of the underlying particle model, while other numerical solutions built directly from the SOH model are not. Here we extend this idea to the SOHR model. More precisely, we introduce the following relaxation model (in dimension $n \quad 2$).

$$\partial_t \rho^\eta - \nabla_x \cdot (\rho^\eta U^\eta) = 0, \tag{3.3.43}$$
$$\partial_t (\rho^\eta \Omega^\eta) + \nabla_x \cdot (\rho^\eta V^\eta \otimes \Omega^\eta) + \nabla_x p(\rho^\eta) - \gamma \Delta_x (\rho^\eta \Omega^\eta) = \frac{\rho^\eta}{\eta}(1 - |\Omega^\eta|^2)\Omega^\eta, \tag{3.3.44}$$
$$U^\eta = c_1 \Omega^\eta \quad \Phi_0 \nabla_x \rho^\eta \quad V^\eta = c_2 \Omega^\eta - \Phi_0 \nabla_x \rho^\eta, \tag{3.3.45}$$
$$p(\rho^\eta) - d\rho^\eta + a\Phi_0 (d + c_2) \frac{(\rho^\eta)^2}{2}, \quad \gamma = k_0 (d + c_2). \tag{3.3.46}$$

The left-hand sides form a conservative system. We get the following proposition:

Proposition 3.3.1. *The relaxation model (4.3.33)-(3.3.46) converges to the SOHR model (3.2.31)-(3.2.34) as η goes to zero.*

The proof of proposition 3.3.1 is given in Appendix C. This allows us to use well-established numerical techniques for solving the conservative system (i.e. the left-hand side of (4.3.33), (4.3.34)). The scheme we propose relies on a time splitting of step Δt between the conservative part

$$\partial_t \rho^\eta + \nabla_x \cdot (\rho^\eta U^\eta) = 0, \tag{3.3.47}$$
$$\partial_t (\rho^\eta \Omega^\eta) + \nabla_x \cdot (\rho^\eta V^\eta \otimes \Omega) + \nabla_x p(\rho^\eta) - \gamma \Delta_x (\rho^\eta \Omega^\eta) = 0, \tag{3.3.48}$$

and the relaxation part

$$\partial_t \rho^\eta = 0, \tag{3.3.49}$$
$$\partial_t (\rho^\eta \Omega^\eta) = \frac{\rho^\eta}{\eta}(1 \quad |\Omega^\eta|^2)\Omega^\eta. \tag{3.3.50}$$

System (3.3.47-3.3.48) can be rewritten in the following form (we omit the superscript η for simplicity)

$$Q_t + (F(Q, Q_x))_x + (G(Q, Q_y))_y = 0,$$

where

$$Q = \begin{pmatrix} \rho \\ \rho\Omega_1 \\ \rho\Omega_2 \end{pmatrix}, \quad F(Q, Q_x) = \begin{pmatrix} \rho U_1 \\ \rho\Omega_1 V_1 + p(\rho) - \gamma\partial_x(\rho\Omega_1). \\ \rho\Omega_1 V_2 \quad \gamma\partial_x(\rho\Omega_2) \end{pmatrix}.$$

$$G(Q, Q_y) = \begin{pmatrix} \rho U_2 \\ \rho\Omega_2 V_1 - \gamma\partial_y(\rho\Omega_1) \\ \rho\Omega_2 V_2 \cdot p(\rho) \quad \gamma\partial_y(\rho\Omega_2) \end{pmatrix}.$$

We consider now the following numerical scheme where we denoted $Q^n_{i,j}$ the approximation of Q at time $t^{n+1} = (n+1)\Delta t$ and position $x_i = i\Delta x, y_j = j\Delta y$:

$$Q^*_{i,j} \quad - \quad Q^n_{i,j} \quad \frac{\Delta t}{\Delta x}\{F^n_{i+1/2,j} \quad F^n_{i-1/2,j}\} \quad \frac{\Delta t}{\Delta y}\{G^n_{i,j+1/2} \quad G^n_{i,j \ 1/2}\},$$

where the numerical flux $F^n_{i-1/2,j}$ is given by

$$F^n_{i+1/2,j} - \frac{F^n(Q^n_{i,j}, Q^n_{xi,j}) + F^n(Q^n_{i+1,j}, Q^n_{x(i+1),j})}{2} - P_2^{t+\frac{1}{2}}\Big(\frac{\partial F}{\partial Q}(\bar{Q}^n_{i,j}, \bar{Q}^n_{xi,j})\Big)(Q^n_{i+1,j} \quad Q^n_{i,j}).$$

with

$$Q^n_{xi,j} = \frac{(Q^n_{i-1,j} - Q^n_{i,j})}{\Delta x}, \quad \bar{Q}^n_{i,j} = \frac{Q^n_{i,j} + Q^n_{i+1,j}}{2}, \quad \bar{Q}^n_{xi,j} = \frac{Q^n_{yi,j} + Q^n_{x(i+1),j}}{2},$$

and the analogous discretization holds for $G^n_{i,j+\frac{1}{2}}$.

In the above formula, $P_2^{t+\frac{1}{2}}$ is a polynomial of matrices of degree 2 calculated with the eigenvalues of the Jacobian matrices $\dfrac{\partial F}{\partial Q}$ at an intermediate state depending on $(Q^n_{i,j}, Q^n_{xi,j})$ and $(Q^n_{i-1,j}, Q^n_{x(i+1),j})$ as detailed in [34]. To ensure stability of the scheme, the time step Δt satisfies a Courant-Friedrichs-Lewy (CFL) condition computed as the minimum of the CFL conditions required for the hyperbolic and diffusive parts of the system.

Once the approximate solution of the conservative system is computed, equations (3.3.49) and (3.3.50) can be solved explicitly. In the limit $\eta \to 0$ they give

$$\rho^{n+1} = \rho^*, \qquad \Omega^{n+1} = \frac{\Omega^*}{|\Omega^*|}$$

where (ρ^*, Ω^*) is the numerical solution of system (3.3.47-3.3.48). This ends one step of the numerical scheme for the system (4.3.33-4.3.34).

3.4 Numerical tests

The goal of this section is to present some numerical solutions of the system (3.2.31)-(3.2.34) which validate the numerical scheme proposed in the previous section. We will first perform a convergence test. We then successively compare the solutions obtained with the SOHR model with those computed by numerically solving the individual based model (3.2.8) in regimes in which the two models should provide similar results. We will finally perform some comparisons between the SOH and the SOHR system to highlight the difference between the two models. We will compare the SOHR model with another way to incorporate repulsion in the SOH Model, the so-called DLMP model of [32].

For all the tests, we use the model in uscaled variables as described in the Introduction (see (3.1.1)-(3.1.5). The potential kernel ϕ is chosen as

$$\phi(x) = \begin{cases} (|x|-1)^2 & \text{if} \quad x^1 \leq 1, \\ 0 & \text{if} \quad |x| > 1. \end{cases} \tag{3.4.51}$$

which gives $\Phi_0 = \frac{\pi}{6}$, while for K, by assumption normalized to 1, we choose the following form

$$K(|z|) = \begin{cases} \frac{1}{\pi} & \text{if} \quad |z| \leq 1, \\ 0 & \text{if} \quad |z| > 1. \end{cases}$$

This leads to $k_0 = \frac{1}{8}$. The other parameters, which are fixed for all simulations if not differently stated, are :

$$\rho_0 = 1, \ \mu = \frac{1}{2}, \ \alpha = 1, \ d = 0.1, \ L_x = 10, \ L_y = 10,$$

which, in dimension $n = 2$, lead to (after numerically computing the GCI and the associated integrals):

$$c_1 = 0.9486, \ c_2 = 0.8486.$$

In the visualization of the results, we will use the angle θ of the vector Ω relative to the x-axis, i.e. $\Omega = (\cos\theta, \sin\theta)$.

3.4.1 Convergence test

The first test is targeted at the validation of the proposed numerical scheme. For this purpose, we investigate the convergence when the space step $(\Delta x, \Delta y)$ tends to $(0,0)$, refining the grid and checking how the error behaves asymptotically. The initial mesh size is $\Delta x = \Delta y = 0.25$ while the time step is $\Delta t = 0.001$. We repeat the computation for $(\frac{\Delta x}{2}, \frac{\Delta y}{2})$, $(\frac{\Delta x}{4}, \frac{\Delta y}{4})$, $(\frac{\Delta x}{8}, \frac{\Delta y}{8})$. The convergence rate is estimated through the measure of the L^1 norm of the error for the vectors $(\rho, \cos\theta)$ by using for each grid the next finer grid as reference solution. The initial data is

$$\rho_0 = 1, \quad \theta_0(x,y) = \begin{cases} \arctan(\frac{y_1}{x_1}) - \frac{\pi}{2} sign(x_1) \text{ if } x_1 \neq 0, \\ \pi \text{ if } x_1 = 0 \text{ and } y_1 > 0. \\ 0 \text{ if } x_1 = 0 \text{ and } y_1 < 0. \end{cases} \tag{3.4.52}$$

where

$$x_1 = x - \frac{L_x}{2}, \quad y_1 = y - \frac{L_y}{2}.$$

The boundary conditions are fixed in time on the four sides of the square : $(\rho^n, \theta^n) = (\rho_0, \theta_0)$. The error curves for the density and for $\cos\theta$ are plotted in figure 3.1 as a function of the space step in log-log scale at time $T = 1s$. The slope of the error curves are compared to a straight line of slope 1. From the figure, we observe the convergence of the scheme with accuracy close to 1.

3.4.2 Comparison between the SOHR and the Vicsek model with repulsion

In this subsection, we validate the SOHR model by comparing it to the Vicsek model with repulsion on two different test cases. We investigate the convergence of the microscopic IBM to the

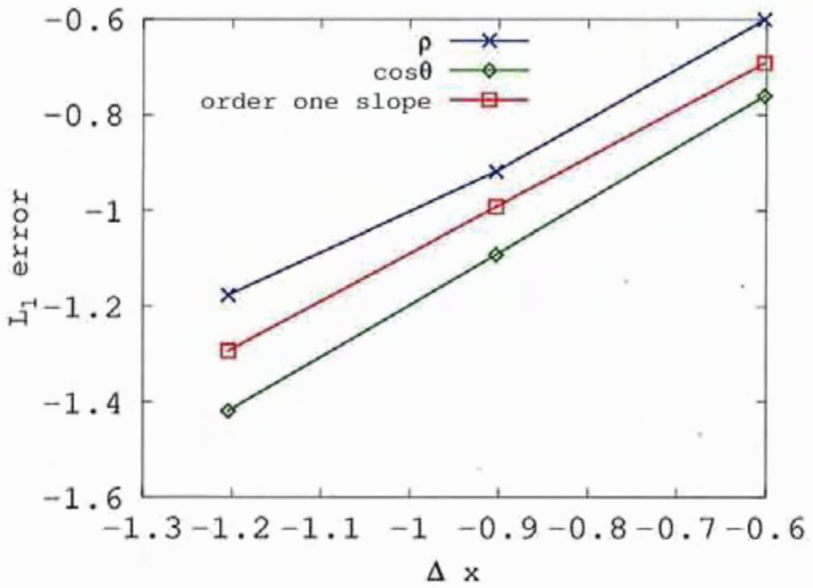

Figure 3.1: L^1-error for the density ρ and the flux direction $\cos\theta$ as a function of Δx in log-log scale. A straight line of slope 1 is plotted for reference. This figure shows that the scheme is numerically of order 1.

macroscopic SOHR model when the scaling parameter ε tend to zero. The scaled IBM is written:

$$\frac{dX_k}{dt} = v_k, \qquad v_k = \omega_k - \nabla_x \Phi(X_k(t), t),$$

$$d\omega_k = P_{\omega_k^\perp} \circ \Big(\frac{1}{\varepsilon} \bar{\omega}(X_k(t), t)\, dt + \alpha\, v_k\, dt + \sqrt{\frac{2d}{\varepsilon}}\, dB_t^k \Big).$$

$$\Phi(x,t) = \frac{1}{\varepsilon^2 N} \sum_{i=1}^{N} \nabla\phi\Big(\frac{|x - X_i|}{\varepsilon\, r} \Big),$$

$$\bar{\omega}(x,t) = \frac{\mathcal{J}(x,t)}{|\mathcal{J}(x,t)|}, \qquad \mathcal{J}(x,t) = \frac{1}{N} \sum_{i=1}^{N} K\Big(\frac{|x - X_i|}{\sqrt{\varepsilon}\, R} \Big) \omega_i.$$

The solution of the individual based model (3.2.8-3.2.10) is computed by averaging different realizations in order to reduce the statistical errors. The coefficient of the IBM are fixed to $r = 0.0625$ for the repulsive range, $R = 0.25$ for the alignment interaction range, while $N = 10^5$ particles are used for each simulation. The details of the particles simulation can be found in [41, 60] for classical particle approaches or in [71] for a direct application to the SOH model.

Riemann problem: The convergence of the two models is measured on a Riemann problem with the following initial data

$$(\rho_l, \theta_l) = (0.0067, 0.7), \quad (\rho_r, \theta_r) = (0.0133, 2.3). \tag{3.4.53}$$

and with periodic boundary condition in x and y. The parameters of the SOHR model are: $\Delta t = 0.01$, $\Delta x = \Delta y = 0.25$. In figure 3.2, we report the relative L^1 norm of the error for the macroscopic quantities (ρ, θ) between the SOHR model and the particle model with respect to the number of averages for different values of $\varepsilon : \varepsilon = 1$ (x-mark), $\varepsilon = 0.5$ (plus), $\varepsilon = 0.1$ (circle), $\varepsilon = 0.05$ (square) at time $T = 1s$. This figure shows, as expected, that the distance between the two solutions goes

to zero when ε goes to zero. It seems however the convergence of the error to 0 as $\varepsilon \to 0$ is rather slow. This is due to the fact that for small ε the IBM becomes very stiff. Simultaneously, accuracy is degraded as the interaction region of a particle shrinks to a point which makes the evaluation of the average direction of the neighbouring particles very noisy. Since our focus is the continuum model we did not address this problem which concerns the IBM and did not try to improve the quality of the tests. Indeed, we consider that obtaining the results shown in Fig. 3.2 is already quite informative as very few fluid models in the literature are compared with the underlying IBM with such a degree of accuracy.

In figure 3.3 we report the density ρ and the flux direction θ for the same Riemann problem along the x-axis for $\varepsilon = 0.05$ at time $T = 1s$, the solution being constant in the y-direction. Again we clearly observe that the two models provide very close solutions, the small differences being due to the different numerical schemes employed for their discretizations.

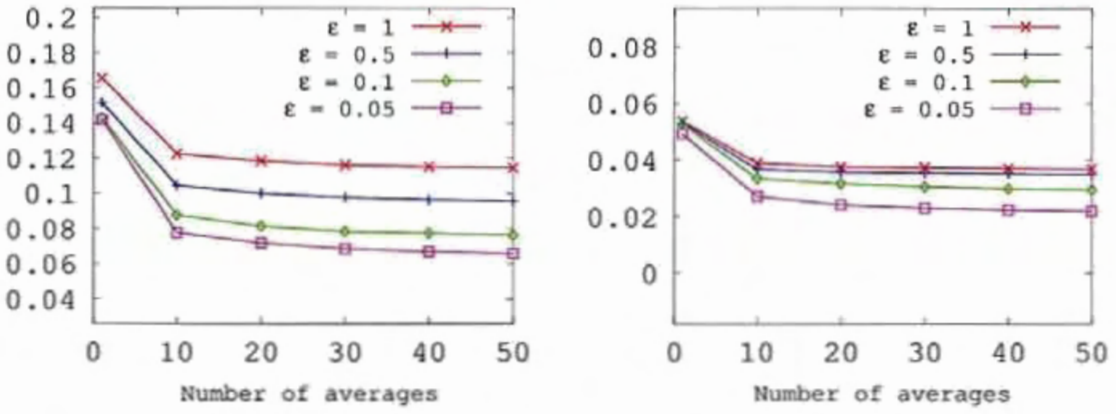

(a) For density ρ (b) For θ

Figure 3.2: Relative error between the macroscopic and the microscopic model for density (a) and θ (b) as a function of the number of averages for different values of ε. The error decreases with both decreasing ε and increasing number of averages, showing that the SOHR model provides a valid approximation of the IBM for ρ and θ.

Taylor-Green vortex problem: In this third test case, we compare the numerical solutions provided by the two models in a more complex case. The initial data are

$$\rho_0 = 0.01, \quad \Omega_0(x,y) = \frac{\tilde{\Omega}_0(x,y)}{|\tilde{\Omega}_0(x,y)|}, \tag{3.4.54}$$

where the vector $\tilde{\Omega}_0 = (\tilde{\Omega}_{01}, \tilde{\Omega}_{02})$ is given by

$$\tilde{\Omega}_{01}(x,y) = \frac{1}{3}\sin(\frac{\pi}{5}x)\cos(\frac{\pi}{5}y) + \frac{1}{3}\sin(\frac{3\pi}{10}x)\cos(\frac{3\pi}{10}y) + \frac{1}{3}\sin(\frac{\pi}{2}x)\cos(\frac{\pi}{2}y),$$
$$\tilde{\Omega}_{02}(x,y) = -\frac{1}{3}\cos(\frac{\pi}{5}x)\sin(\frac{\pi}{5}y) - \frac{1}{3}\cos(\frac{3\pi}{10}x)\sin(\frac{3\pi}{10}y) - \frac{1}{3}\cos(\frac{\pi}{2}x)\sin(\frac{\pi}{2}y).$$

with periodic boundary conditions in both directions. The numerical parameters for the SORH model are : $\Delta x = \Delta y = 0.2$, $\Delta t = 0.01$, while for the particle simulations we choose : $N = 10^5$ particles, $\varepsilon = 0.05$, $r = 0.04$, $R = 0.2$. In figure 3.4 and 3.5, we report the density ρ and the flux direction Ω at time $t = 0.6s$. In both figures, the left picture is for the IBM and the right one for the SOHR model. Again, we find a very good agreement between the two models in spite of the quite complex structure of the solution.

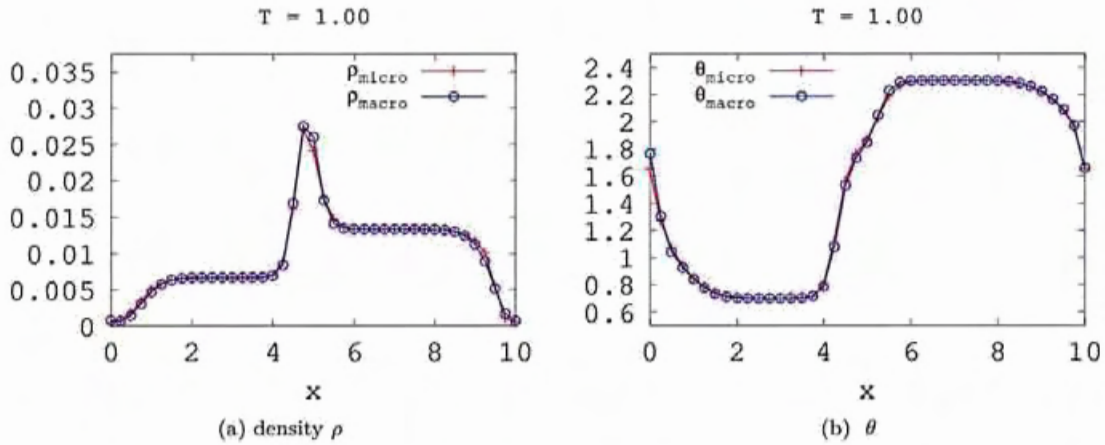

(a) density ρ (b) θ

Figure 3.3: Solution of the Riemann problem (3.4.53) along the x-axis for the SOHR model (blue line) and for the IBM with $\varepsilon = 0.05$ (red line) at $T = 1s$. The agreement between the two models is excellent. For the SOHR model, the mesh size is $\Delta x = \Delta y = 0.0625$.

Due to the large number of particles required and the need for averages over a large number of realizations, the IBM is several orders of magnitude more costly than the SOHR model. Indeed, the statistical noise decays like $\mathcal{O}(1/\sqrt{M})$ with the number M of realizations, which is very slow. Additionally, the amplitude of the statistical noise increases with time. In practice, we have averaged over up to 50 realizations of the IBM according to the test cases. By contrast, only one single simulation of the SOHR model is needed. Here, we have used an explicit discretization of the diffusion operator because the values of the diffusion constant and of the mesh sizes still led to manageable time steps. In other applications, it could be necessary to perform an implicit discretization of the diffusion operators, but this question is outside the scope of the present work.

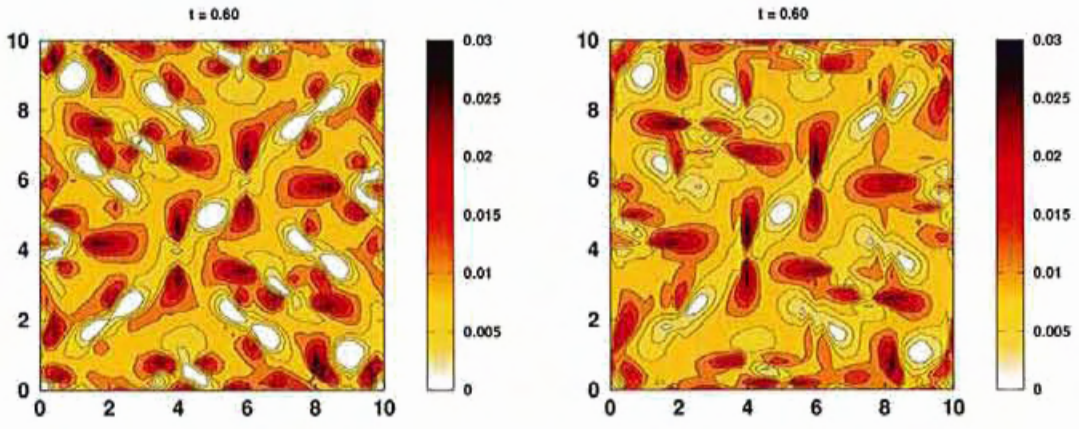

(a) density ρ for the IBM (b) density ρ for the SOHR model

Figure 3.4: Density ρ for Taylor-Green vortex problem 3.4.54 at time $t = 0.6s$. Left: IBM. Right: SOHR model.

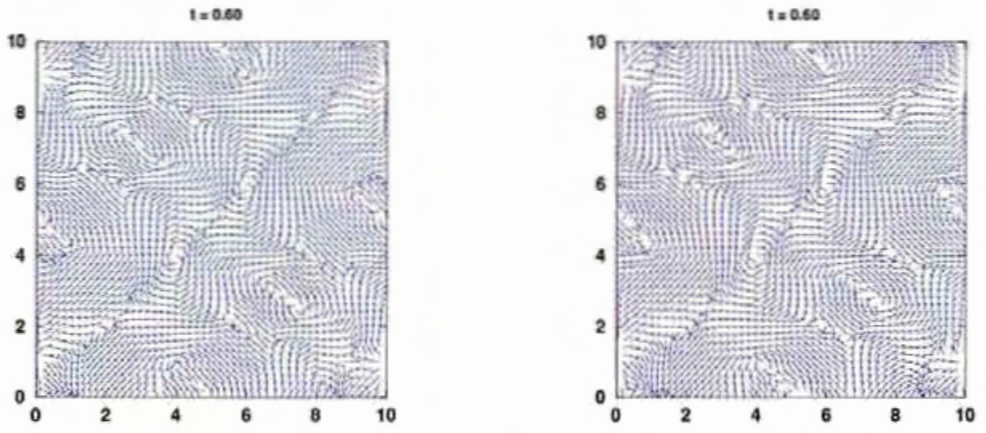

(a) Ω for the IBM

(b) Ω for the SOHR model

Figure 3.5: Mean direction Ω for Taylor-Green vortex problem 3.4.54 at time $t = 0.6s$. Left: IBM. Right: SOHR model.

3.4.3 Comparison between the SOH and the SOHR model

In this part, we show the difference between the SOH system (3.1.6), (3.1.7) and the SOHR one for different values of the repulsive force Φ_0. We recall that the SOHR model reduces to the SOH one in the case in which the repulsive force is set equal to zero. To this aim, we rescale the repulsive force Φ_0 by

$$\Phi_0 = F_0 \int_{x \in \mathbb{R}^2} \phi(x) dx$$

and then we let F_0 vary. The repulsive potential ϕ is still given by (3.4.51), so that $\Phi_0 = F_0\pi/6$. The other numerical parameters are chosen as follows: $d = 0.05$, $\alpha = 0$, $k_0 = 1/8$, $\mu = 1$, $L_x = 10, L_y = 10$, $\Delta x = \Delta y = 0.15$, $\Delta t = 0.001$. The initial data are those of the vortex problem (3.4.52) except that we start with four vortices instead of only one. Periodic boundary conditions in both directions are used.

Figure (3.6) displays the solutions for the SOHR system for the density (left) and for the flux direction (right) at $T = 1.5s$ with $F_0 = 5$. Figure (3.7) displays the solutions for $F_0 = 0.05$. The results are almost undistinguishable to those of the SOH model ($F_0 = 0$) and are not shown for this reason. These figures show that when the repulsive force is large enough, the SOHR model can prevent the formation of high concentrations. By contrast, when this force is small, the SOHR model becomes closer to the SOH one and high concentrations become possible.

3.4.4 Comparison between the SOHR and the DLMP model

In this final part, we want to compare the SOHR system to the hydrodynamic model proposed by Degond, Liu, Motsch and Panferov in [32] (referred to as DLMP model). This model is derived, in a similar fashion as the SOHR model, starting from a system of self-propelled particles which obey to alignment and repulsion. The main difference is that in the DLMP model, the particle velocity is exactly equal to the self propulsion velocity but the particles adjust their orientation to respond to repulsion as well as alignment. The resulting model is of SOH type and is therefore written (3.1.6), (3.1.7), but with an increased coefficient in front of the pressure term $P_{\Omega^\perp}\nabla_x \rho$, this coefficient being equal to $v_0\, d(1 + \frac{d+c_2}{c_1} F_0)$. The initial conditions and numerical parameters are the same as in previous test

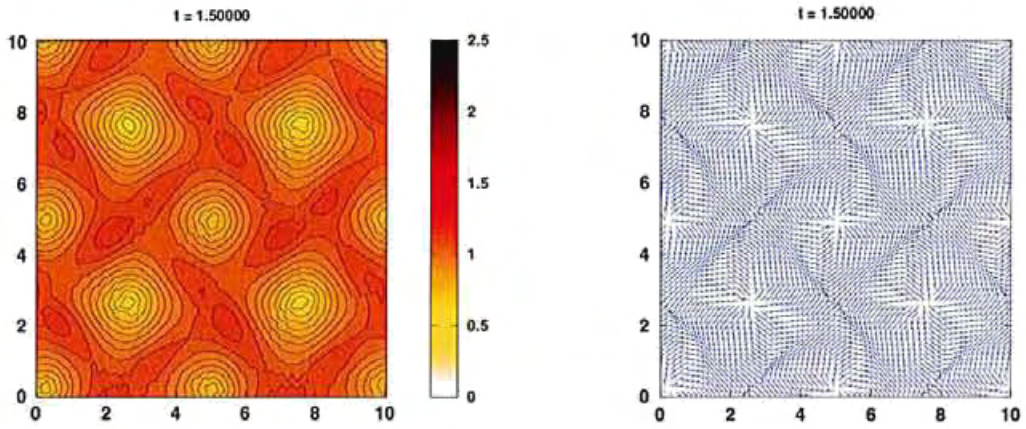

(a) density ρ for $F_0 = 5$ (b) Ω for $F_0 = 5$

Figure 3.6: Solution of the SOHR model for $F_0 = 5$. Density ρ (fig 3.6a), flux direction Ω (fig.3.6b) at $t = 1.5s$.

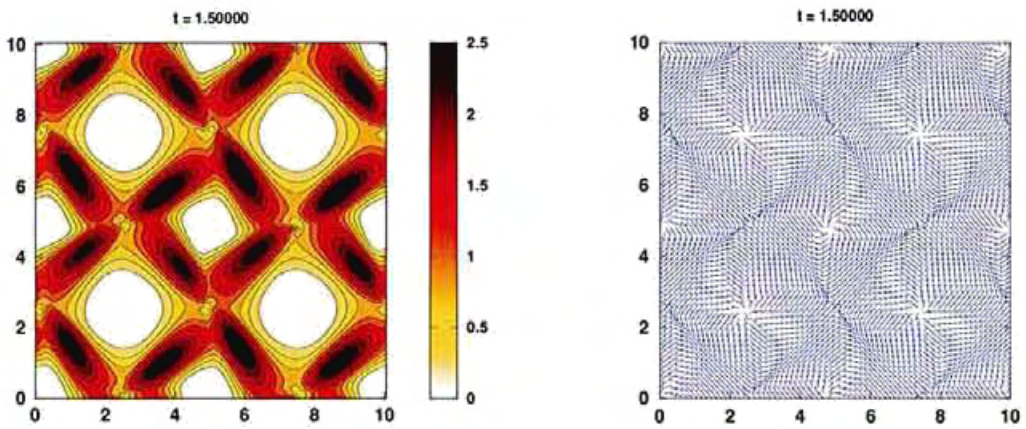

(a) density ρ for $F_0 = 0.05$ (b) Ω for $F_0 = 0.05$

Figure 3.7: Solution of the SOHR model for $F_0 = 0.05$. Density ρ (fig 3.6a), flux direction Ω (fig.3.6b) at $t = 1.5s$.

In figure 3.8, we report the density ρ (left) and the flux direction Ω (right) for $F_0 = 5$ for the DLMP model. Comparing figures 3.6 with figure 3.8, we observe that the solutions of the SOHR and of the DLMP model are different. The homogenization of the density seems more efficient with the SOHR model than with the DLMP model. This can be attributed to the effect of the nonlinear diffusion terms that are included in the SOHR model but not in the DLMP model. Therefore, the way repulsion is included in the models may significantly affect the qualitative behavior of the solution. In practical situations, when the exact nature of the interactions is unknown, some care must be taken to choose the right repulsion mechanism.

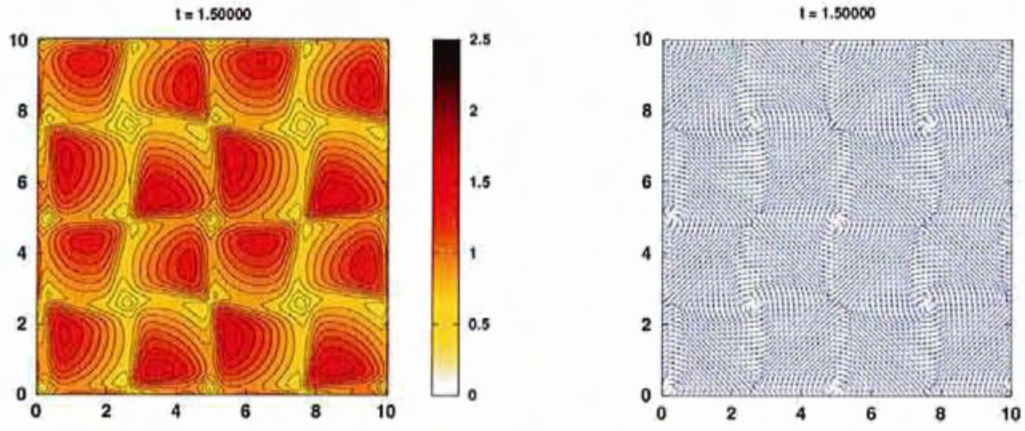

(a) density ρ (b) Ω

Figure 3.8: Solution of the DLMP model for $F_0 = 5$. Density ρ (left) and flux direction Ω (right) at $t = 1.5s$.

3.5 Conclusion

In this paper, we have derived a hydrodynamic model for a system of self-propelled particles which interact through both alignment and repulsion. In the underlying particle model, the actual particle velocity may be different from the self-propulsion velocity as a result of repulsion interactions with the neighbors. Particles update the orientation of their self-propulsion seeking to locally align with their neighbors as in Vicsek alignment dynamics. The corresponding hydrodynamic model is similar to the Self-Organized Hydrodynamic (SOH) system derived from the Vicsek particle model but it contains several additional terms arising from repulsion. These new terms consist principally of gradients of linear or nonlinear functions of the density including a non-linear diffusion similar to porous medium diffusion. This new Self-Organized Hydrodynamic system with Repulsion (SOHR) has been numerically validated by comparisons with the particle model. It appears more efficient to prevent high density concentrations than other approaches based on simply enhancing the pressure force in the SOH model. In future work, this model will be used to explore self-organized motion in collective dynamics. To this effect, it will be calibrated on data based on biological experiments, such as recordings of collective sperm-cell motion.

Appendix A Proof of formulas (3.2.21) and (3.2.22)

By introducing the change of variable $z = -\dfrac{x-y}{\sqrt{\varepsilon}R}$ and using Taylor expansion, we get

$$\begin{aligned}
&\frac{1}{(\sqrt{\varepsilon}R)^n}\int_{\mathbb{S}^{n-1}\times\mathbb{R}^n} K\big(\frac{|x-y|}{\sqrt{\varepsilon}R}\big)\, f^\varepsilon(y,\omega,t)\,\omega\, d\omega\, dy \\
&= \int_{\mathbb{S}^{n-1}\times\mathbb{R}^n} K(|z|)\, f^\varepsilon(x+\sqrt{\varepsilon}Rz,\omega,t)\,\omega\, dz\, d\omega \\
&= \int_{\mathbb{S}^{n-1}\times\mathbb{R}^n} K(|z|)\,\big(f^\varepsilon + \sqrt{\varepsilon}\,R\,\nabla_x f^\varepsilon\cdot z + \frac{\varepsilon R^2}{2} D_x^2 f : (z\otimes z) + O(\sqrt{\varepsilon}^3)\big)(x,\omega,t)\,\omega\, dz\, d\omega \\
&= \big(J(x,t) + \varepsilon\, k_0\, \Delta_x J(x,t) + O(\varepsilon^2)\big),
\end{aligned}$$

where k_0 is given by (3.2.23) and $D_x^2 f$ is the Hessian matrix of f with respect to the variable x. Here, we have used that the $\mathcal{O}(\sqrt{\varepsilon})$ and $\mathcal{O}(\varepsilon^{3/2})$ terms vanish after integration in z by oddness with respect to z.

By the same computation for the kernel ϕ, we have

$$\begin{aligned}
&\frac{1}{(\varepsilon r)^n}\int_{\mathbb{S}^{n-1}\times\mathbb{R}^n}\phi\Big(\frac{|x-y|}{\varepsilon r}\Big)f^\varepsilon(y,\omega,t)dyd\omega\\
&\quad-\int_{\mathbb{S}^{n-1}\times\mathbb{R}^n}\phi(|z|)f^\varepsilon(x+\varepsilon rz,\omega,t)dzd\omega\\
&\quad=\int_{\mathbb{S}^{n-1}\times\mathbb{R}^n}\phi(|z|)(f^\varepsilon+\varepsilon r\nabla_x f\cdot z+O(\varepsilon^2))(x,\omega,t)dzd\omega\\
&\quad=\Phi_0\int_{\mathbb{S}^{n-1}}f^\varepsilon(x,\omega,t)d\omega+O(\varepsilon^2),
\end{aligned}$$

with $\Phi_0=\int_{\mathbb{R}^n}\phi(|z|)dz$.

Appendix B Proof of Theorem 3.2.1

We prove that (3.2.41) leads to (3.2.32). Thanks to (3.2.37), Eq. (3.2.41) can be written:

$$P_{\Omega^\perp}\int_{\omega\in\mathbb{S}^2}(\mathcal{T}_1(\rho M_\Omega)+\mathcal{T}_2(\rho M_\Omega)+\mathcal{T}_3(\rho M_\Omega))h(\omega\cdot\Omega)\omega d\omega:=T_1+T_2+T_3=0, \tag{3.5.1}$$

where $\mathcal{T}^k$, $k=1,2,3$ are given by (3.2.40). Now, $\mathcal{T}_1(\rho M_\Omega)$ can be written:

$$\mathcal{T}_1(\rho M_\Omega)=\partial_t(\rho M_\Omega)+\nabla_x\cdot(\omega\rho M_\Omega)-\Phi_0\nabla_x\cdot\left(\nabla_x\left(\frac{\rho^2}{2}\right)M_\Omega\right). \tag{3.5.2}$$

We recall that the first two terms of $\mathcal{T}_1$ at the right hand side of (3.5.2) and the corresponding terms in T_1 have been computed in [29]. The computation for the third term of $\mathcal{T}_1$ is easy and we get:

$$T_1=\beta_1\rho\partial_t\Omega+\beta_2\rho(\Omega\cdot\nabla_x)\Omega+\beta_3P_{\Omega^\perp}\nabla_x\rho+\beta_4(\nabla_x\left(\frac{\rho^2}{2}\right)\cdot\nabla_x)\Omega$$

where the coefficients are given by

$$\begin{aligned}
&\beta_1=\frac{1}{d(n-1)}\langle\sin^2\theta\,h\rangle_{M_\Omega},\quad \beta_2=\frac{1}{d(n-1)}\langle\sin^2\theta\cos\theta\,h\rangle_{M_\Omega},\\
&\beta_3=\frac{1}{n-1}\langle\sin^2\theta\,h\rangle_{M_\Omega},\quad \beta_4=-\frac{\Phi_0}{d(n-1)}\langle\sin^2\theta\,h\rangle_{M_\Omega}.
\end{aligned}$$

Now observe that for a constant vector $A\in\mathbb{R}^n$, we have

$$\nabla_\omega(\omega\cdot A)=P_{\omega^\perp}A,\qquad \nabla_\omega\cdot(P_{\omega^\perp}A)=-(n-1)\omega\cdot A. \tag{3.5.3}$$

Thus, using (3.2.40), (3.5.3) and the chain rule, we get for $\mathcal{T}_2(\rho M_\Omega)$

$$\begin{aligned}
\mathcal{T}_2(\rho M_\Omega) &= \alpha\Phi_0\Big((n-1)\omega\cdot\nabla_x(\rho^2/2)-d^{-1}\nabla_x(\rho^2/2)\cdot\Omega\\
&\qquad+d^{-1}(\omega\cdot\nabla_x(\rho^2/2))(\omega\cdot\Omega)\Big)M_\Omega
\end{aligned}$$

Finally, we obtain:

$$T_2=\beta_5P_{\Omega^\perp}\nabla_x\left(\frac{\rho^2}{2}\right),$$

where

$$\beta_5 = \alpha\Phi_0\left(\langle\sin^2\theta\, h\rangle_{M_\Omega} + \frac{1}{d(n-1)}\langle\sin^2\theta\,\cos\theta\, h\rangle_{M_\Omega}\right).$$

The terms $T_4(\rho M_\Omega)$ and T_3 have been computed in [32]. In particular, it is easy to see that we get them from the formulae for $\mathcal{T}_2(\rho M_\Omega)$ and T_2 by changing $-\alpha\Phi_0\nabla_x(\rho^2/2)$ into $k_0 P_{\Omega^\perp}\Delta_x(\rho\Omega)$. Therefore, we get:

$$T_3 = \beta_6\, P_{\Omega^\perp}\Delta_x(\rho\Omega),$$

where

$$\beta_6 = k_0\left(\langle\sin^2\theta\, h\rangle_{M_\Omega} + \frac{1}{d(n-1)}\langle\sin^2\theta\,\cos\theta\, h\rangle_{M_\Omega}\right).$$

Inserting the expressions of T_1, T_2 and T_3 into (3.5.1) we get (3.2.32).

Appendix C Proof of Proposition 3.3.1

We follow the lines of the proof of Proposition 3.1 of [71]. Assume that $\rho^\eta \to \rho^0$ and $\Omega^\eta \to \Omega^0$ as η tends to zero. Then, set

$$R^\eta := \rho^\eta(1 - |\Omega^\eta|^2)\Omega^\eta.$$

Multiplying equation (4.3.34) by η and then taking the limit $\eta \to 0$ yields $R^\eta \to 0$. It follows that $|\Omega^0|^2 = 1$. Since the vector R^η is parallel to Ω^η, we have $P_{(\Omega^\eta)^\perp} R^\eta = 0$, which implies that

$$P_{(\Omega^\eta)^\perp}\Big(\partial_t(\rho^\eta\Omega^\eta) + \nabla_x\cdot(\rho^\eta V^\eta \otimes \Omega^\eta) + \nabla_x p(\rho^\eta) - \gamma\Delta_x(\rho^\eta\Omega^\eta)\Big) = 0.$$

Therefore, letting $\eta \to 0$, we obtain

$$\partial_t(\rho^0\Omega^0) + \nabla_x\cdot(\rho^0 V^0 \otimes \Omega^0) + \nabla_x p(\rho^0) - \gamma\Delta_x(\rho^0\Omega^0) = \beta\Omega^0. \tag{3.5.4}$$

where β is a real number, $p(\rho^\eta) \to p(\rho^0) = d\rho^0 + \alpha\Phi_0(d+c_2)(\rho^0)^2/2$, $V^0 = c_2\Omega^0 - \Phi_0\nabla_x\rho^0$ and $U^0 = c_1\Omega^0 - \Phi_0\nabla_\perp\rho^0$. By taking the scalar product of (3.5.4) with Ω^0, we get

$$\beta = \partial_t\rho^0 + \nabla_x\cdot(\rho^0 V^0) - \nabla_x p(\rho^0)\cdot\Omega^0 - \gamma\Delta_x(\rho^0\Omega^0)\cdot\Omega^0.$$

Inserting this expression of β into (3.5.4) we find the equation for the evolution of the average direction (3.2.32) and thus the SOHR model (3.2.31)-(3.2.34).

Chapter 4

Existence of solution for a system of repulsion and alignment: comparison between theory and simulation

This chapter is a work in progress.

4.1 Introduction

We consider a macroscopic model of dense suspension of elongated self-propelled particles in a fluid such as bacteria, sperm cells, etc. The particle model from which this hydrodynamic model comes considers the movement of particles via alignment interaction and exclusive volume interaction. The alignment interaction leads to particles alignment with the mean direction of their neighbours while the steric repulsion rules out the formation of high concentration of particles. This model is motivated by recent experimental observations in raw ram sperm which indicate that sperm cells occupy about 50% of the total volume of sperm. Therefore, it is legitimate to consider both volume exclusion and alignment interactions. The goal of the present work is to study the existence of solution of this continuous model by both theory and simulations.

The simplest model, proposed by Vicsek and his coauthors [93], considers alignment interaction in which particles move at a constant speed and have tendency to align to their neighbours with some additional random noise. Despite its simplicity in appearance, this model can find many important applications in wide range of biological systems such as cluster, migration.

Volume exclusion interaction have been studied intensively in the recent years[5, 23, 58, 75]. In systems of dense suspension, particles are very close together. Therefore, steric repulsion plays an important role in the movement of particles. In [75], the authors have shown that elongated self-propelled particles interacting through volume exclusion result in alignment.

Macroscopic models is well suited to study modelling of large scale systems in contrast with particle models (also known as 'Individual-Based Models' or IBM) which focus on the inter-particle interaction scale. When the number of particles are large, the computational cost of IBM models becomes very large. Moreover, the macroscopic models allows us to study the qualitative behaviors of the system at large scale such as equilibrium solution, long time behaviors, phase transition, etc. The derivation of such models has studied by many authors [5, 9, 29, 79]. In particular, a rigorous derivation (the so-called 'Self-Organized Hydrodynamics' (SOH)) through kinetic equation

has been done in [29] (see the review [25]). Some related research on the SOH model have been established such as the existence of solution in two and three dimensions [29], numerical simulations [71]. Within this framework, phase transition have been analyzed [4, 24, 27, 44]. By following the method used in [29], the hydrodynamic model of self-propelled particles interacting through local alignment and repulsion is derived in the chapter 3, the so called Self-Organized Hydrodynamic model with Repulsion (SOHR). This model presents a new way to incorporate repulsion in macroscopic models of self-organized dynamics. In the same work, the authors also present some numerical simulations which validate their numerical scheme and validate the SOHR model by comparison with those of the particle one.

The SOHR model describes the evolution of two macroscopic quantities: the density of particles $\rho(t,x) \subset \mathbb{R}_+$ and the average orientation $\Omega(t,x) \subset \mathbb{S}^{n-1}$ of the flow at a given point $(t,x) \subset [0,T] \times \mathbb{R}^n$. n is the spatial dimension and $\mathbb{S}^{n-1}$ denotes the unit sphere in $\mathbb{R}^n$. The evolution of ρ and Ω are governed by the following equations:

$$\partial_t \rho + \nabla_x \cdot (\rho U) = 0 \tag{4.1.1}$$

$$\rho \partial_t \Omega + \rho (V \cdot \nabla)\Omega + P_{\Omega^\perp} \nabla p(\rho) = \gamma P_{\Omega^\perp} \Delta(\rho \Omega) \tag{4.1.2}$$

$$|\Omega| = 1 \tag{4.1.3}$$

where the vector U, V and the pressure $p(\rho)$ are given by

$$U = \beta_1 \Omega - \beta_2 \nabla_x \rho, \quad V = \beta_3 \Omega - \beta_4 \nabla_x \rho, \quad p(\rho) = c_1 \rho + c_2 \rho^2/2 \tag{4.1.4}$$

and the coefficients $\beta_1, \cdots, \beta_4, c_1, c_2, \gamma$ are constants depending on the intensity noise. In chapter 3, we always have $\beta_2 = \beta_4$. $P_{\Omega^\perp} = (\mathrm{Id} \quad \Omega \otimes \Omega)$ is the orthogonal projection onto the plan orthogonal to Ω, where $\otimes$ denotes the tensor product of two vectors and Id is the identity matrix. This model is similar to the SOH model [25]. The significant differences are additional terms coming from the repulsive force at the particle level. Equation (4.1.1) is a conservative equation of mass. The density moves with the velocity U consisting of a term $\beta_1 \Omega$, the same as the SOH model, and an additional term which plays the role of a diffusion term in porous media which prevents the high concentration of particles. Equation (4.1.2) describes the movement of the mean orientation with the velocity V, influenced by a term playing the role of pressure due to gradient of the density. The appearance of the term $-\beta_4 \nabla_x \rho$ in the velocity vector V makes change the moving direction of the mean orientation towards regions of low concentration if the coefficient β_4 is positive and towards regions of high concentration if the coefficient β_4 is negative. The pressure $p(\rho)$ consists of a linear part, the same as in the SOH model, and a non linear part which increases the repulsive force when concentrations become high. A different point between the Navier-Stokes equations and the SOH model [25] is that the convection velocities of the density and the mean orientation are different while those of the Navier-Stokes equations are equal. Moreover, the coefficients β_1, β_3 satisfy $0 < \beta_3 \leq \beta_1$ where $\beta_1 = \beta_3$ if and only if the noise is absent. For the SOH model, in [43], it was shown that the coefficient β_3 may be negative. In this case, the mean orientation Ω is transported in opposite direction to the flow. An example of such system is a car traffic in congested situations. The two equations is supplemented of a geometric constraint $|\Omega| = 1$. This constraint is preserved at all times by the projection operator $P_{\Omega^\perp}$. This property results from the loss of Galilean invariance [92] which is an essential difference between collective phenomena in standard statistical physics and biology.

This chapter is devoted to study the existence of solutions of the SOHR model from both theory and simulation point of view. By using techniques in [32], we also show that a local solution of the system (4.1.1), (4.1.2) exists uniquely on $[0,T]$ for $\beta_1 > 0$ and $\beta_2, c_1, c_2, \gamma$ non-negative constants. In order to perform simulations, we follow the scheme used in the chapter 3 where the convergence of this scheme and the convergence of numerical solutions of the SOHR model have been already shown . The numerical results reveal that the existence time of numerical solution depends on the relationship between the coefficients. More precisely, when β_4 is sufficiently large, the numerical

solutions exist only for short time. By contrast, when β_1 is small enough, the numerical solution exists for long time.

The outline of the paper is as follows. In section 1, we present the theorem for the existence of the solution. In section 3, we report the solutions for the vortex problem in some cases of the coefficients. A conclusion will be drawn in section 3

4.2 Existence theory in 2D

In this section we study the existence of the local solution of the system (4.1.1), (4.1.1) in 2-dimensions with the initial condition

$$\rho(t=0) = \rho_0 > 0, \quad \Omega(t=0) = \Omega_0, \quad |\Omega_0| = 1.$$

We assume that the domain is the square box $\Pi^2 = [0,1]^2$ with periodic boundary conditions. The coefficient β_1 is positive constant and $\beta_2, c_1, c_2, \gamma$ are non-negative constants.

Theorem 4.2.1. *We assume that the initial data belong to $H^m(\Pi^2)$ with $m > 2$. Then there exists a time $T > 0$ and a unique solution (ρ, ψ) in $L^\infty([0,T]; H^m(\Pi^2)) \cap H^1([0,T]; H^{m-2}(\Pi^2))$ such that ρ is positive. Moreover, if the coefficients $\beta_2, \gamma > 0$ then the solution also belongs to $L^2([0,T]; H^{m+1}(\Pi^2)) \cap H^1([0,T]; H^{m-1}(\Pi^2))$.*

In 2 dimensions, we can write $\Omega = (\cos\psi, \sin\psi)$. Then the system (4.1.1), (4.1.2) can be rewritten as follows:

$$\partial_t \rho + \beta_1 \nabla_x \rho \cdot \Omega - \beta_1 \rho \Omega^\perp \cdot \nabla\psi \quad \beta_2 \Delta\rho^2/2 \tag{4.2.5}$$

$$\partial_t \psi + \beta_3 \Omega \cdot \nabla\psi + \frac{\rho'(\rho)}{\rho} \Omega^\perp \cdot \nabla\rho - \beta_1 \nabla_x \psi \quad \nabla\rho - \gamma(\Delta\psi - 2\nabla_x \rho \cdot \nabla_x \psi/\rho) \tag{4.2.6}$$

4.2.1 Maximum principle and symmetrization

We denote ρ_{min}, ρ_{max} by

$$\rho_{min} = \min_{x \in \Pi^2} \rho_0(x), \quad \rho_{max} = \max_{x \in \Pi^2} \rho_0(x). \tag{4.2.7}$$

Let $\rho^k(x) = \rho(kh, x)$, $h > 0$, then the equation (4.2.5) can be written as follows

$$(\rho^k - \rho^{k-1})/h + \beta_1 \nabla_x \rho^k \cdot \Omega^k + \beta_1 \rho^k (\Omega^-)^k \cdot \nabla\psi^k = \beta_2 \rho^k \Delta\rho^k - \beta_2 |\nabla\rho^k|^2 + \epsilon(h) \tag{4.2.8}$$

where $\epsilon(h) \to 0$ as $h \to 0^+$. We assume that $\rho^k(x_0) = \max_x \rho(kh, x)$. This means that

$$\nabla_x \rho(kh, x_0) = 0, \quad \Delta\rho(kh, x_0) \leq 0.$$

From (4.2.5) we obtain

$$\frac{\rho^k(x_0) - \rho^{k-1}(x_0)}{h} \quad \epsilon(h) \leq \beta_1 \rho^k(x_0) \|\nabla\psi^k(x)\|_{L^\infty(\Pi^2)} \tag{4.2.9}$$

Taking the limit $h \to 0^+$, and applying Gronwall's inequality, we have the following a priori estimate

$$\rho_{min} \exp\Big(\int_0^t -\beta_1 \|\nabla_x \psi(\cdot, s)\|_{L^\infty(\Pi^2)} ds\Big) \leq \rho(t,x) \leq \rho_{max} \exp\Big(\int_0^t \beta_1 \|\nabla_x \psi(\cdot, s)\|_{L^\infty(\Pi^2)} ds\Big).$$

We introduce the functions $\tilde{\rho} = a(\rho)$, $\lambda(\tilde{\rho})$, $h(\tilde{\rho})$, such that

$$a'(\rho) = \frac{\sqrt{p'(\rho)}}{\rho}, \quad \lambda(\tilde{\rho}) = a'(\rho)\rho, \quad h(\tilde{\rho}) = 2\ln\rho.$$

Then, the system (4.2.5), (4.2.6) becomes:

$$\begin{aligned} \partial_t\tilde{\rho} = &-\beta_1\Omega \ \nabla_x\tilde{\rho} - \beta_1\lambda(\tilde{\rho})\Omega^\perp\cdot\nabla_x\psi + \beta_2\nabla\cdot(a^{-1}(\tilde{\rho})\nabla\tilde{\rho}) \\ &-\beta_2\nabla\lambda(\tilde{\rho})\cdot\nabla(a^{-1}(\tilde{\rho})) + \beta_2\nabla a^{-1}(\tilde{\rho})\cdot\nabla\tilde{\rho} \qquad (4.2.10) \\ \beta_1\partial_t\psi = &-\beta_3\beta_1\Omega\cdot\nabla\psi - \beta_1\lambda(\tilde{\rho})\Omega^\perp\cdot\nabla\tilde{\rho} - \beta_1\beta_4\nabla_x\psi\cdot\nabla a^{-1}(\tilde{\rho}) \\ &+\gamma\beta_1(\Delta\psi + \nabla_x h(\tilde{\rho})\cdot\nabla_x\psi) \qquad (4.2.11) \end{aligned}$$

since

$$\begin{aligned} a'(\rho)\Delta\frac{\rho^2}{2} &= \nabla\cdot(a'(\rho)\rho\nabla\rho) - a''(\rho)\rho\nabla\rho\cdot\nabla\rho \\ &= \nabla\cdot(a'(\rho)\rho\nabla\rho) \quad (\lambda'(\tilde{\rho})a'(\rho) \quad a'(\rho))\nabla\rho\cdot\nabla\rho \\ &= \nabla\cdot(\rho\nabla\tilde{\rho}) - \nabla\lambda(\tilde{\rho})\cdot\nabla\rho + \nabla\tilde{\rho}\cdot\nabla\rho \\ &= \nabla\cdot(a^{-1}(\tilde{\rho})\nabla\tilde{\rho}) \quad \nabla\lambda(\tilde{\rho})\cdot\nabla a^{-1}(\tilde{\rho}) + \nabla a^{-1}(\tilde{\rho})\cdot\nabla\tilde{\rho}. \end{aligned}$$

Now, the existence of local solutions of this system follows from the modified Garlerkin method for quasi-linear parabolic equations (see e.g.Taylor's book [88]). The a priori estimate of the solutions can be proved using the same techniques in [32] and exploiting the symmetrization of the terms $\lambda(\tilde{\rho})\Omega^\perp\cdot\nabla_x\psi$ and $\lambda(\tilde{\rho})\Omega^\perp\cdot\nabla\tilde{\rho}$.

4.2.2 Existence of approximating solution

We consider the approximating system:

$$\begin{aligned} \partial_t\tilde{\rho}^\varepsilon &= J^\varepsilon A_1(J^\varepsilon\tilde{\rho}_\varepsilon, J^\varepsilon\psi_\varepsilon) \qquad (4.2.12) \\ \partial_t\psi^\varepsilon &\quad J^\varepsilon A_2(J^\varepsilon\tilde{\rho}_\varepsilon, J^\varepsilon\psi_\varepsilon) \qquad (4.2.13) \end{aligned}$$

where the functions $A_1(\tilde{\rho},\psi)$, $A_2(\tilde{\rho},\psi)$ denote the right hand side of the equations (4.2.10), (4.2.11), respectively. Here, J^ε is a Friedrichs mollifier, which we can take to be of the form

$$J^\varepsilon = \varphi(\varepsilon\sqrt{-\Delta}) \qquad (4.2.14)$$

with an even function $\varphi\in\mathcal{S}(\Pi^2)$, and $\varphi(0) = 1$. Equivalently, for $f\in D'(\Pi^2)$ the Fourier transform $\mathcal{F}$ of $J^\varepsilon f$ is given by

$$\mathcal{F}(J^\varepsilon f)(k) = \varphi(\varepsilon|k|)\mathcal{F}f(k) \qquad (k\in\mathbb{R}^2). \qquad (4.2.15)$$

We see that the function $A = (A_1, A_2)$ is Lipschitz thanks to Plancherel's theorem. By classical theory of ODE this yields the existence of a short-time solution of the system (4.2.12), (4.2.13).

4.2.3 Estimation of the approximating solution

In this subsection, we will show that the solution $(\tilde{\rho}_\varepsilon, \psi_\varepsilon)$ exists for t in a time interval independent of ε and has a limit as $\varepsilon\to 0$. For this purpose, we estimate the H^m – norm of the solution $(\tilde{\rho}_\varepsilon, \psi_\varepsilon)$. We denote $D^\alpha = \partial_{x_1^{\alpha_1}\ldots x_n^{\alpha_n}}$ with $|\alpha| = \sum_{i=1}^n\alpha_i$. We take the D^α- derivative of (4.2.12), multiply it by $D^\alpha\tilde{\rho}_\varepsilon$ and integrate it with respect to x. We do the same thing for equation (4.2.13), but we multiply it by $D^\alpha\psi_\varepsilon$. Then we sum up the resulting identities to get

$$
\begin{aligned}
0 \;=\; & \frac{d}{dt}\|D^\alpha\hat\rho_\varepsilon(t)\|^2-\beta_1\frac{d}{dt}|\,D^\alpha\psi_\varepsilon(t)\|^2\\
& +\beta_1\langle D^\alpha\big(J^\varepsilon(\Omega_\varepsilon\cdot\nabla)J^\varepsilon\hat\rho_\varepsilon\big),D^\alpha\hat\rho_\varepsilon\rangle+\beta_1\beta_3\langle D^\alpha\big(J^\varepsilon\big(\Omega_\varepsilon\cdot\nabla\big)J^\varepsilon\psi_\varepsilon\big),D^\alpha\psi_\varepsilon\rangle\\
& +\beta_1\langle D^\alpha\big(J^\varepsilon(\lambda(J^\varepsilon\hat\rho)(\Omega_\varepsilon^\perp\cdot\nabla)J^\varepsilon\psi_\varepsilon\big),D^\alpha\hat\rho_\varepsilon\rangle-\beta_1\langle D^\alpha(J^\varepsilon\lambda(J^\varepsilon\hat\rho_\varepsilon)(\Omega_\varepsilon^\perp\cdot\nabla)J^\varepsilon\hat\rho_\varepsilon),D^\alpha\psi_\varepsilon\rangle\\
& +\beta_2\langle D^\alpha\big(J^\varepsilon\nabla\cdot(a^{-1}(J^\varepsilon\hat\rho_\varepsilon)\nabla J^\varepsilon\hat\rho_\varepsilon)\big),D^\alpha\hat\rho_\varepsilon\rangle\\
& -\beta_2\langle D^\alpha\big(J^\varepsilon\nabla\lambda(J^\varepsilon\hat\rho_\varepsilon)\cdot\nabla a^{-1}(J^\varepsilon\hat\rho_\varepsilon)\big),D^\alpha\hat\rho_\varepsilon\rangle\\
& +\beta_2\langle D^\alpha\big(J^\varepsilon\nabla a^{-1}(J^\varepsilon\hat\rho_\varepsilon)\cdot\nabla(J^\varepsilon\hat\rho_\varepsilon)\big),D^\alpha\hat\rho_\varepsilon\rangle\\
& -\gamma\beta_1\langle D^\alpha J^\varepsilon\Delta J^\varepsilon\psi_\varepsilon,D^\alpha\psi_\varepsilon\rangle\\
& -\beta_1\beta_4\langle D^\alpha\big(J^\varepsilon\nabla J^\varepsilon\psi_\varepsilon\cdot\nabla a^{-1}(J^\varepsilon\hat\rho)\big),D^\alpha\psi_\varepsilon\rangle\\
& -\gamma\beta_1\langle D^\alpha(J^\varepsilon\nabla h(J^\varepsilon\hat\rho_\varepsilon)\cdot\nabla J^\varepsilon\psi_\varepsilon),D^\alpha\psi_\varepsilon\rangle\\
=\;& I_1-I_2+\cdots+I_9
\end{aligned}
$$

It is not hard to see that

$$
I_7\;\geq\;\gamma\beta_1\|\nabla D^\alpha(J^\varepsilon\psi_\varepsilon)\|^2. \tag{4.2.16}
$$

Now, we estimate I_1. Since J^ε commutes with D^α, and is self-adjoint, we can write

$$
\begin{aligned}
I_4 \;=\;& \beta_2\langle D^\alpha\big(a^{-1}(J^\varepsilon\hat\rho_\varepsilon)\nabla J^\varepsilon\hat\rho_\varepsilon\big),\nabla D^\alpha J^\varepsilon\hat\rho_\varepsilon\rangle\\
=\;& \beta_2\langle a^{-1}(J^\varepsilon\hat\rho_\varepsilon)\nabla D^\alpha(J^\varepsilon\hat\rho_\varepsilon),\nabla D^\alpha J^\varepsilon\hat\rho_\varepsilon\rangle\\
& +\beta_2\langle D^\alpha\big(a^{-1}(J^\varepsilon\hat\rho_\varepsilon)\nabla J^\varepsilon\hat\rho_\varepsilon\big)-a^{-1}(J^\varepsilon\hat\rho_\varepsilon)\nabla D^\alpha(J^\varepsilon\hat\rho_\varepsilon),\nabla D^\alpha J^\varepsilon\hat\rho_\varepsilon\rangle\\
=\;& I_{41}+I_{42}
\end{aligned}
$$

We need the following lemma whose proof can be found later on.

Lemma 4.2.2. *We have*

$$
|I_k|\leq C(\|J^\varepsilon\hat\rho_\varepsilon\|_{W^{1,\infty}}+\|J^\varepsilon\psi_\varepsilon\|_{W^{1,\infty}})(\|J^\varepsilon\hat\rho_\varepsilon\|_{H^m}^2+\|J^\varepsilon\psi_\varepsilon\|_{H^m}^2),\quad k=2,3 \tag{4.2.17}
$$

$$
|I_{41}|\geq f_0\beta_2\|\nabla D^\alpha(J^\varepsilon\hat\rho_\varepsilon)\|^2 \tag{4.2.18}
$$

$$
\begin{aligned}
|I_k|\leq\;& \frac{f_0\beta_2}{4}\|\nabla D^\alpha(J^\varepsilon\hat\rho_\varepsilon)\|^2\\
& +C(\|J^\varepsilon\hat\rho_\varepsilon\|_{W^{1,\infty}}^2+\|J^\varepsilon\psi_\varepsilon\|_{W^{1,\infty}}^2)(\|J^\varepsilon\hat\rho_\varepsilon\|_{H^m}^2+\|J^\varepsilon\psi_\varepsilon\|_{H^m}^2),\quad k=4,2,5,6
\end{aligned} \tag{4.2.19}
$$

$$
\begin{aligned}
|I_k|\leq\;& \frac{\gamma\beta_1}{4}\|\nabla D^\alpha(J^\varepsilon\psi_\varepsilon)\|^2\\
& +C(\|J^\varepsilon\hat\rho_\varepsilon\|_{W^{1,\infty}}^2+\|J^\varepsilon\psi_\varepsilon\|_{W^{1,\infty}}^2)(\|J^\varepsilon\hat\rho_\varepsilon\|_{H^m}^2+\|J^\varepsilon\psi_\varepsilon\|_{H^m}^2),\quad k=8,9
\end{aligned} \tag{4.2.20}
$$

where C denote generic constants depending on the parameters of the problem.

Now, coming back to our estimates. Summing all terms together for all possible indices α such that $|\alpha|\leq m$, we obtain

$$
\begin{aligned}
& \frac{d}{dt}(\|\hat\rho_\varepsilon(t)\|_{H^m}^2+\beta_1\|\psi_\varepsilon(t)\|_{H^m}^2)\\
& \qquad+\frac{f_0\beta_2}{4}\|\nabla(J^\varepsilon\hat\rho_\varepsilon)\|_{H^m}^2+\frac{\gamma\beta_1}{2}\|\nabla(J^\varepsilon\psi_\varepsilon)\|_{H^m}^2\\
& \qquad\leq C(\|J^\varepsilon\hat\rho_\varepsilon\|_{W^{1,\infty}}^2+\|J^\varepsilon\psi_\varepsilon\|_{W^{1,\infty}}^2+1)(\|J^\varepsilon\hat\rho_\varepsilon\|_{H^m}^2+\|J^\varepsilon\psi_\varepsilon\|_{H^m}^2)
\end{aligned} \tag{4.2.21}
$$

For $m\geq\dfrac{n}{2}+1$, using the Sobolev imbedding theorem, we have

$$
(\|J^\varepsilon\hat\rho_\varepsilon\|_{W^{1,\infty}}+\|J^\varepsilon\psi_\varepsilon\|_{W^{1,\infty}})\leq C(\|J^\varepsilon\hat\rho_\varepsilon\|_{H^m}+\|J^\varepsilon\psi_\varepsilon\|_{H^m}). \tag{4.2.22}
$$

So, we get

$$\frac{d}{dt}(\|\hat{\rho}_\varepsilon(t)\|^2_{H^m} + \beta_1\|\psi_\varepsilon(t)\|^2_{H^m}) \le C(\|J^\varepsilon\hat{\rho}_\varepsilon\|^2_{H^m} + \|J^\varepsilon\psi_\varepsilon\|^2_{H^m} + 1)^2 \tag{4.2.23}$$

Since the sequence $\{J^\varepsilon,\ 0 < \varepsilon \le 1\}$ is uniformly bounded on each space $C^m(\Pi^2)$ and $H^m(\Pi^2)$, inequality (4.2.23) yields

$$\frac{d}{dt}(\|\hat{\rho}_\varepsilon(t)\|^2_{H^m} + \beta_1\|\psi_\varepsilon(t)\|^2_{H^m}) \le C(\|\hat{\rho}_\varepsilon(t)\|^2_{H^m} + \|\psi_\varepsilon(t)\|^2_{H^m} + 1)^2. \tag{4.2.24}$$

It follows from Gronwall's inequality that there exists a function $K(t)$, finite on some interval $[0, T]$ such that

$$\|\hat{\rho}_\varepsilon(t)\|^2_{H^m} + \|\psi_\varepsilon(t)\|^2_{H^m} \le K(t),\ \forall\varepsilon. \tag{4.2.25}$$

Therefore, the approximating solutions $(\hat{\rho}_\varepsilon, \psi_\varepsilon)$ belong to $C(0, T; H^m(\Pi^2))$. On the other hand, taking the H^{m-2} norm in equations (4.2.12), (4.2.13), we obtain

$$\begin{aligned}\|(\hat{\rho}_\varepsilon)_t\|_{H^{m-2}} + \beta_1\|(\psi_\varepsilon)_t\|_{H^{m-2}} &\le C(\|\hat{\rho}_\varepsilon\|_{H^m} + \|\psi_\varepsilon\|_{H^m}) \\ &+ C(\|\hat{\rho}_\varepsilon\|_{H^{m-1}} + \|\psi_\varepsilon\|_{H^{m-1}})(\|\hat{\rho}_\varepsilon\|_{W^{1,\infty}} + \|\psi_\varepsilon\|_{W^{1,\infty}})\end{aligned} \tag{4.2.26}$$

So, the approximating solutions belong to $C^1(0, T, H^{m-2}(\Pi^2))$.

Limit of the approximating solution

From the above results, the bounded family

$$(\hat{\rho}_\varepsilon, \psi_\varepsilon) \subset C(0, T; H^m(\Pi^2)) \cap C^1(0, T; H^{m-2}(\Pi^2))$$

has a weak* limit $(\hat{\rho}, \psi) \in L^\infty(0, T; H^m)$. Let $[H^{s_1}(\mathbb{R}^n), H^{s_2}(\mathbb{R}^n)]_\sigma$ be the interpolation space of two spaces $H^{s_1}(\mathbb{R}^n)$ and $H^{s_2}(\mathbb{R}^n)$ for $s_1, s_2 \in \mathbb{R}$ and $\sigma \in (0, 1)$. We have

$$[H^{s_1}(\mathbb{R}^n), H^{s_2}(\mathbb{R}^n)]_\sigma = H^{s_1\sigma + (1-\sigma)s_2}(\mathbb{R}^n) \tag{4.2.27}$$

By setting $u_\varepsilon := (\hat{\rho}_\varepsilon, \psi_\varepsilon)$ and choosing $s_1 = m - 2$, $s_2 = m$, we get

$$\|u_\varepsilon\|_{H^{m-2}} \le \|u_\varepsilon\|^\sigma_{H^{m-2}}\|u_\varepsilon\|^{1-\sigma}_{H^m} \tag{4.2.28}$$

Consider now

$$\|u_\varepsilon\|_{C^\sigma(0,T,H^{m-2})} = \|u_\varepsilon\|_{C(0,T,H^{m-2})} + \sup_{t_1 \ne t_2}\frac{\|u_\varepsilon(t_1) - u_\varepsilon(t_2)\|_{H^{m-2}}}{|t_1 - t_2|^\sigma}. \tag{4.2.29}$$

Using inequality (4.2.28), we get

$$\begin{aligned}&\frac{1}{|t_1 - t_2|^\sigma}\|u_\varepsilon(t_1) - u_\varepsilon(t_2)\|_{H^{m-2}} \\ &\le \frac{1}{|t_1 - t_2|^\sigma}\|u_\varepsilon(t_1) - u_\varepsilon(t_2)\|^\sigma_{H^{m-2}}\|u_\varepsilon(t_1) - u_\varepsilon(t_2)\|^{1-\sigma}_{H^m} \\ &\le \frac{1}{|t_1 - t_2|^\sigma}\|\int_0^1 \partial_t u_\varepsilon(t_1\lambda + (1-\lambda)t_2)d\lambda\|^\sigma_{H^{m-2}}|t_1 - t_2|^\sigma\|u_\varepsilon(t_1) - u_\varepsilon(t_2)\|^{1-\sigma}_{H^m} \\ &\le \|\int_0^1 \partial_t u_\varepsilon(t_1\lambda + (1-\lambda)t_2)d\lambda\|^\sigma_{H^{m-2}}\|u_\varepsilon(t_1) - u_\varepsilon(t_2)\|^{1-\sigma}_{H^m} \\ &< +\infty.\end{aligned}$$

So, the family $\{(\hat{\rho}_\varepsilon, \psi_\varepsilon),\ 0 \le \varepsilon \le 1\}$ is bounded in $C^\sigma(0, T; H^{m-2\sigma}(\Pi^2))$ for each $\sigma \in (0, 1)$. Applying Ascoli's theorem, there exists a subsequence $\{(\hat{\rho}_{\varepsilon_l}, \psi_{\varepsilon_l})\}$ of the sequence $\{(\hat{\rho}_\varepsilon, \psi_\varepsilon),\ 0 < \varepsilon \le 1\}$ such that

$$(\hat{\rho}_{\varepsilon_l}, \psi_{\varepsilon_l}) \to (\hat{\rho}, \psi) \text{ in } C(0, T; C^2(\Pi^2)) \tag{4.2.30}$$

since the inclusion $H^{m-2\sigma} \hookrightarrow C^2$ is compact for small σ and $m > n/2+2$. Taking the limit $\varepsilon_l \to 0$ in the system (4.2.12), (4.2.13), we conclude that $(\hat\rho, \psi)$ is a solution of the system (4.2.10), (4.2.11). Moreover, if $\beta_2, \gamma > 0$, taking the integral of the inequality (4.2.21) with respect to t, we see that the solution $(\hat\rho, \psi)$ also belongs to $L^2(0,T; H^{m+1}(\Pi^2))$. Taking the H^{m-1} -norm of the system (4.2.10), (4.2.11) and using the same computation as in the proof of Lemma 4.2.2, we get

$$\begin{aligned}\|(\hat\rho)_t\|_{H^{m-1}} + \beta_1 \|(\psi)_t\|_{H^{m-1}} &\le C(\|\hat\rho\|_{H^{m+1}} + \|\psi\|_{H^{m+1}}) \\ &+ C(\|\hat\rho\|_{H^m} + \|\psi\|_{H^m})(\|\hat\rho\|_{W^{1,\infty}} + \|\psi\|_{W^{1,\infty}}).\end{aligned}$$

This inequality implies that $(\hat\rho, \psi)$ also belongs to $H^1(0,T; H^{m-1}(\Pi^2))$. Since the function $a(\rho)$ is smooth and invertible for $\rho > 0$, the estimates on $\hat\rho$ immediately transfer to ρ. The proof is complete.

Proof of Lemma 4.2.2

We recall the following lemma (p.11 in [88]):

Lemma 4.2.3. *For any pair of function f, g in $H^m(\mathbb{R}^n) \cap L^\infty(\mathbb{R}^n)$, we have*

$$\|fg\|_{H^m} \le C(\|f\|_{H^m}\|g\|_{L^\infty} + \|g\|_{H^m}\|f\|_{L^\infty}) \tag{4.2.31}$$

If additionally, we suppose that $\nabla f \in L^\infty(\mathbb{R}^n)$, we have for any $\alpha \in \mathbb{N}^m$, with $|\alpha| = \sum_{i=1}^m \alpha_i = m$

$$\|D^\alpha(fg) - fD^\alpha g\|_{L^2} \le C(\|f\|_{H^m}\|g\|_{L^\infty} + \|g\|_{H^{m-1}}\|\nabla f\|_{L^\infty}), \tag{4.2.32}$$

where $D^\alpha = \partial_{x_1^{\alpha_1}\cdots x_m^{\alpha_m}}$.

The terms I_2, I_3, I_9 have been estimated in [43].

Estimate of I_{42}: Since J^ε commutes to D^α and is self-adjoint, using Green's formula, Lemma 4.2.3 and Cauchy-Schwartz inequality, we get

$$\begin{aligned}|I_{42}| &= \beta_2|(D^\alpha\big(a^{-1}(J^\varepsilon\hat\rho_\varepsilon)\nabla J^\varepsilon\hat\rho_\varepsilon\big) - a^{-1}(J^\varepsilon\hat\rho_\varepsilon)\nabla D^\alpha(J^\varepsilon\hat\rho_\varepsilon), \nabla D^\alpha J^\varepsilon\hat\rho_\varepsilon)| \\ &\le \beta_2\|D^\alpha\big(a^{-1}(J^\varepsilon\hat\rho_\varepsilon)\nabla J^\varepsilon\hat\rho_\varepsilon\big) - a^{-1}(J^\varepsilon\hat\rho_\varepsilon)\nabla D^\alpha(J^\varepsilon\hat\rho_\varepsilon)\|_{L^2}\|\nabla D^\alpha J^\varepsilon\hat\rho_\varepsilon\|_{L^2} \\ &\le C\|J^\varepsilon\hat\rho_\varepsilon\|_{H^m}\|\nabla J^\varepsilon\hat\rho_\varepsilon\|_{L^\infty}\|\nabla J^\varepsilon\hat\rho_\varepsilon\|_{H^m} \\ &\le \frac{\beta_2 f_0}{4}\|\nabla J^\varepsilon\hat\rho_\varepsilon\|^2_{H^m} + C\|J^\varepsilon\hat\rho_\varepsilon\|^2_{H^m}\|\nabla J^\varepsilon\hat\rho_\varepsilon\|^2_{L^\infty} \\ &\le \frac{\beta_2 f_0}{4}\|\nabla J^\varepsilon\hat\rho_\varepsilon\|^2_{H^m} + C(\|J^\varepsilon\hat\rho_\varepsilon\|^2_{H^m} + \|J^\varepsilon\psi_\varepsilon\|^2_{H^m})(\|J^\varepsilon\hat\rho_\varepsilon\|^2_{W^{1,\infty}} + \|J^\varepsilon\psi_\varepsilon\|^2_{W^{1,\infty}})\end{aligned}$$

where the third inequality uses Lemma 4.2.3 and the fourth one uses Young's inequality $AB \le C_0A^2 + B^2/(4C_0)$ with $C_0 = \beta_2 f_0$.

Estimate of I_5, I_6: Due to similarity of I_5 and I_6 it suffices to estimate I_5. By using Green's formula, Lemma (4.2.3) and Cauchy-Schwartz's inequality, we have

$$\begin{aligned}|I_5 &= \beta_2|(D^\alpha\big(J^\varepsilon\nabla\lambda(J^\varepsilon\hat\rho_\varepsilon)\cdot\nabla a^{-1}(J^\varepsilon\hat\rho_\varepsilon)\big), D^\alpha\hat\rho_\varepsilon)| \\ &\le C\|\nabla D^\alpha J^\varepsilon\hat\rho_\varepsilon\|_{L^2}\|D^{\alpha-1}\big(\nabla\lambda(J^\varepsilon\hat\rho_\varepsilon)\cdot\nabla a^{-1}(J^\varepsilon\hat\rho_\varepsilon)\big)\|_{L^2} \\ &\le C\|\nabla D^\alpha J^\varepsilon\hat\rho_\varepsilon\|_{L^2}\|\nabla\lambda(J^\varepsilon\hat\rho_\varepsilon)\cdot\nabla a^{-1}(J^\varepsilon\hat\rho_\varepsilon)\|_{H^{m-1}} \\ &\le C\|\nabla D^\alpha J^\varepsilon\hat\rho_\varepsilon\|_{L^2}\|J^\varepsilon\hat\rho_\varepsilon\|_{H^m}\|J^\varepsilon\hat\rho_\varepsilon\|_{W^{1,\infty}} \\ &\le \frac{\beta_2 f_0}{4}\|\nabla D^\alpha J^\varepsilon\hat\rho_\varepsilon\|^2_{L^2} + C(\|J^\varepsilon\hat\rho_\varepsilon\|^2_{H^m} + \|J^\varepsilon\psi\|^2_{H^m})(\|J^\varepsilon\hat\rho_\varepsilon\|^2_{W^{1,\infty}} + \|J^\varepsilon\psi_\varepsilon\|^2_{W^{1,\infty}}).\end{aligned}$$

Estimate of I_8: The terms I_8 is estimated similarly as I_5, I_6. We get

$$\begin{aligned}|I_8| &= \beta_1\beta_4|(D^\alpha\big(J^\varepsilon\nabla J^\varepsilon\psi_\varepsilon\cdot\nabla a^{-1}(J^\varepsilon\hat\rho)\big), D^\alpha\psi_\varepsilon)| \\ &\le \beta_1\beta_4\|\nabla D^\alpha J^\varepsilon\psi_\varepsilon\|_{L^2}\|D^{\alpha-1}\big(\nabla J^\varepsilon\psi_\varepsilon\cdot\nabla a^{-1}(J^\varepsilon\hat\rho_\varepsilon)\big)\|_{L^2} \\ &\le C\|\nabla D^\alpha J^\varepsilon\psi_\varepsilon\|_{L^2}(\|J^\varepsilon\hat\rho_\varepsilon\|_{H^m}\|J^\varepsilon\psi_\varepsilon\|_{W^{1,\infty}} + \|J^\varepsilon\psi_\varepsilon\|_{H^m}\|J^\varepsilon\hat\rho\|_{W^{1,\infty}}) \\ &\le \frac{\beta_1\gamma}{4}\|\nabla D^\alpha J^\varepsilon\psi_\varepsilon\|^2_{L^2} - C(\|J^\varepsilon\hat\rho_\varepsilon\|^2_{H^m} + \|J^\varepsilon\psi_\varepsilon\|^2_{H^m})(\|J^\varepsilon\hat\rho_\varepsilon\|^2_{W^{1,\infty}} + \|J^\varepsilon\psi_\varepsilon\|^2_{W^{1,\infty}})\end{aligned}$$

4.3 Simulations

In this section, we will compare the theoretical and numerical results of the system (4.1.1), (4.1.2) in two dimensions. Numerical methods for this system have been presented in chapter 3. We recall that this system is not conservative because of the geometric constraint $|\Omega_i| = 1$. However, we could consider this system as the zero relaxation limit of the conserved one. This idea has been introduced by Motsch and Navoret [71] to numerically solve the SOH model. By this way, the numerical solutions of the SOHR model are considered as those of the following relaxation system:

$$\partial_t \rho^\eta + \nabla_x \cdot (\rho^\eta U^\eta) = 0. \tag{4.3.33}$$

$$\partial_t(\rho^\eta \Omega^\eta) + \nabla_x \cdot (\rho^\eta V^\eta \otimes \Omega^\eta) + \nabla_x p(\rho^\eta) - \gamma \Delta_x(\rho^\eta \Omega^\eta) = \frac{\rho^\eta}{\eta}(1 - |\Omega^\eta|^2)\Omega^\eta. \tag{4.3.34}$$

$$U^\eta = \beta_1 \Omega^\eta \quad \beta_2 \nabla_x \rho^\eta \qquad V^\eta = \beta_3 \Omega^\eta \quad \beta_4 \nabla_x \rho^\eta \tag{4.3.35}$$

where the geometric constraint $|\Omega| = 1$ is removed. The scheme proposed for this model can be found in chapter 3.

In this section, we will study the role of additional terms (the terms $\nabla\rho$ in U and V) in the SOHR model to the SOH model obtained in [29]. Initial condition are chosen as follows.

$$\rho_0 = 1, \quad \Omega_0 = (\cos\theta_0, \sin\theta_0), \tag{4.3.36}$$

$$\theta_0(x, y) = \begin{cases} \arctan(\dfrac{y_1}{x_1}) - \dfrac{\pi}{2}\mathrm{sign}(x_1) \text{ if } x_1 \neq 0 \\ \pi \text{ if } x_1 = 0 \text{ and } y_1 > 0 \\ 0 \text{ if } x_1 = 0 \text{ and } y_1 < 0 \end{cases} \tag{4.3.37}$$

where

$$\begin{aligned} x_1 &= x - L_x/4,\ y_1 = y \quad L_y/4 \quad \text{if} \quad x < L_x/2,\ y < L_y/2, \\ x_1 &= x - 3L_x/4,\ y_1 = y - L_y/4 \quad \text{if} \quad x \geq L_x/2,\ y \leq L_y/2, \\ x_1 &= x - L_x/4,\ y_1 = y - 3L_y/4 \quad \text{if} \quad x \leq L_x/2,\ y \geq L_y/2, \\ x_1 &= x - 3L_x/4,\ y_1 \quad y - 3L_y/4 \quad \text{if} \quad x \geq L_x/2,\ y \geq L_y/2 \end{aligned}$$

and L_x, L_y are the length of domain in x, y-directions, respectively. Simulation will be performed with periodic boundary conditions in both directions. In order to avoid the complexity of boundary behaviors, we choose $L_x = L_y = 10$. Parameters, which are fixed for all simulations if not differently stated, are $\Delta x = \Delta y = 0.2$, $\Delta t = 0.01$, $\beta_1 = 0.9$, $\beta_3 = 0.8$, $c_1 = 0.1, c_2 = 0.2, \gamma = 0.1$. We let the parameters β_2, β_4 vary.

Firstly, we will verify the role like a non-linear diffusion term of the term $-\beta_2\nabla\rho$ in the expression of the velocity U by simulations. Inserting this term in equation (4.1.1) results in $-\beta_2\Delta(\rho^2/2)$. For this purpose, we will perform simulations for different values of β_2. To do so, we fix $\beta_4 = 0$, and let β_2 vary. Figure 4.1, 4.2, 4.3 illustrate the solution of the system (4.1.1), (4.1.2) for $\beta_2 = 0$, $\beta_2 = 0.6$ and $\beta_2 = 2$, respectively. It is clear that this term contributes to prevent the formation of high concentration of the density ρ.

Secondly, we will investigate the role of the term $\nabla\rho$ in the expression of the velocity V in the system (4.1.1), (4.1.2) by simulations. For this purpose, we fix the coefficients $\beta_2 = 0$ and let β_4 vary. Simulations are performed for some cases of coefficients which are shown in the table 4.1.

In figures 4.4, 4.5, 4.6, we report the density ρ (left) and the mean orientation Ω (right) of the SOHR model at time $T = 1.5s$ in the cases 1, 2, 3, respectively. We observe that in the absence of the porous term β_2, when $\beta_4 > \beta_{4crit}$ a critical value, the solution becomes singular. When $\beta_4 < \beta_{4crit}$, the solution is regular. For $\beta_4 = 0.3$, the solution is regular (see figure 4.4) but starts

Coefficients	β_1	β_2	β_4	c_2	γ
case 1	0.9	0	0.3	0.2	0.1
case 2	0.9	0	0.8	0.2	0.1
case 3	0.9	0	2	0.2	0.1

Table 4.1: This table shows some cases of coefficients.

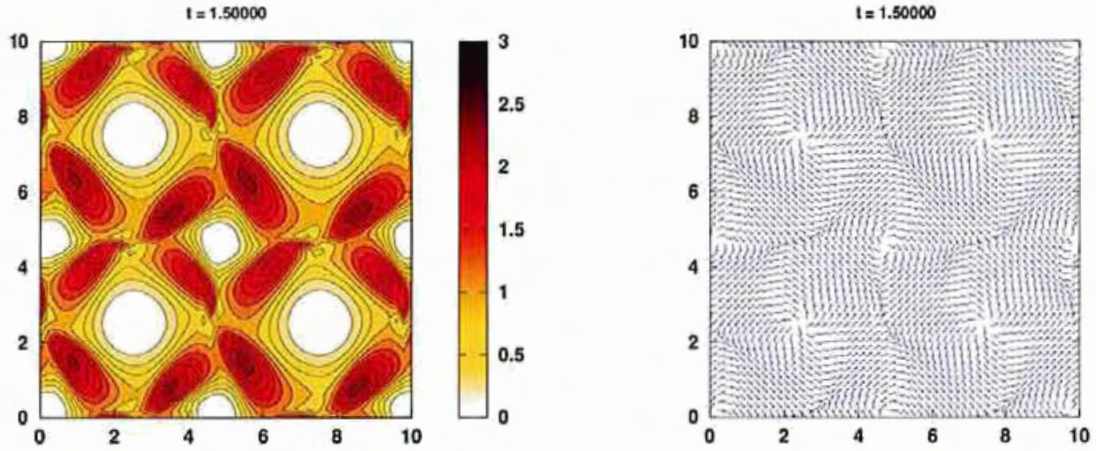

(a) density ρ (b) Ω

Figure 4.1: The solution of the SOHR model for $\beta_2 = 0, \beta_4 = 0, \gamma = 0.1, c_2 = 0.2$

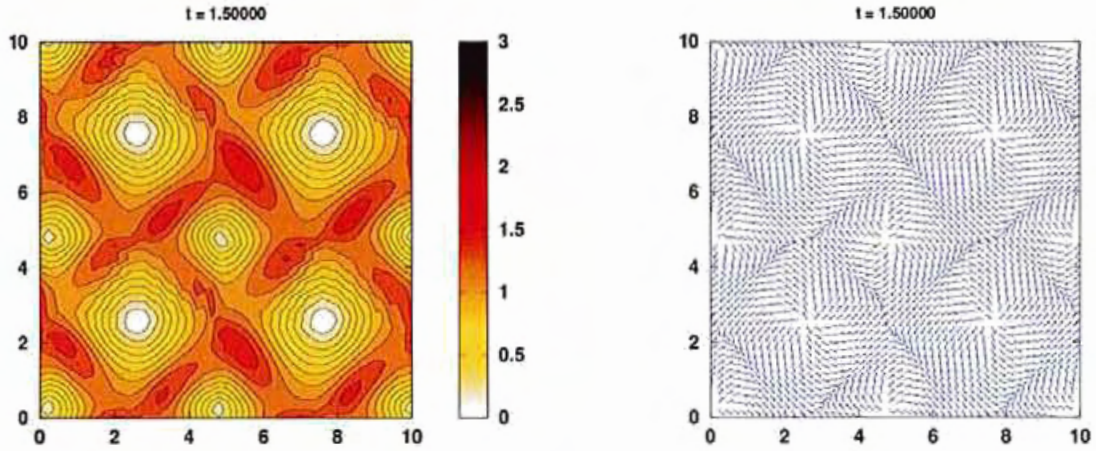

(a) density ρ (b) Ω

Figure 4.2: The solution of the SOHR model for $\beta_2 = 0.6, \beta_4 = 0, \gamma = 0.1, c_2 = 0.2$.

being unstable at some points at $\beta_4 = 0.8$ (see figure 4.5) and becomes totally unstable at $\beta_4 = 2$ (see figure 4.6). Therefore, the term $-\beta_4(\nabla\rho \cdot \nabla)\Omega$ plays a role of a unstable term and brings the singularity to the system.

We will study more about the case where the unstability of the solution occurs (case 2). For this purpose, we fix $\beta_4 = 0.8$, and change only one of the coefficients c_2, γ, β_2. The coefficients of the

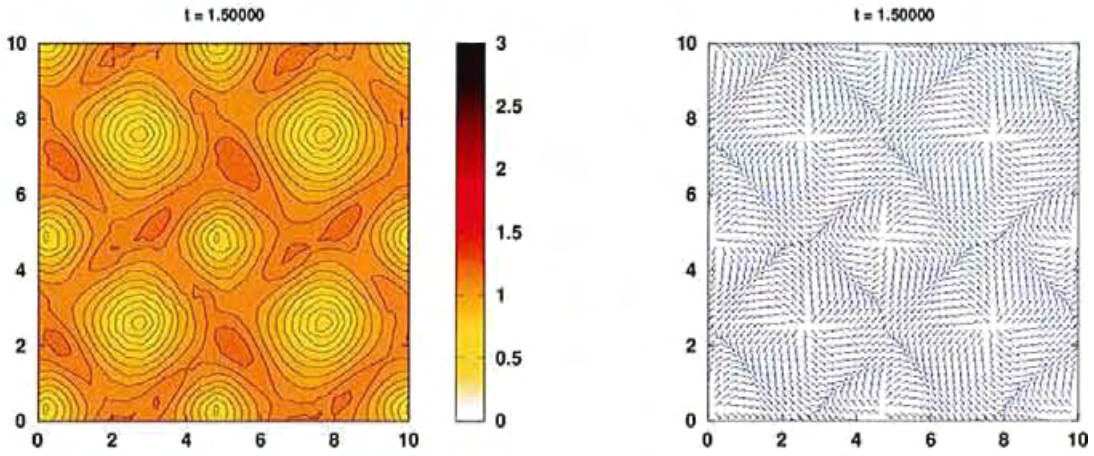

(a) density ρ (b) Ω

Figure 4.3: The solution of the SOHR model for $\beta_2 = 2, \beta_4 = 0, \gamma = 0.1, c_2 = 0.2$.

Coefficients	β_1	β_2	β_4	c_2	γ
case 4	0.9	0	0.8	1	0.1
case 5	0.9	0	0.8	0.2	0.5
case 6	0.9	0.6	0.8	0.2	0.1
case 7	0.1	0	0.8	0.2	0.1

Table 4.2: This table reports some cases of the coefficients.

SOHR model chosen are shown in table 4.2.

The solution in the cases 4, 5, 6 are presented in figures 4.7, 4.8, 4.9, respectively. We see that the solution of the SOHR system becomes regular again when we increase one of the coefficients of diffusion terms (including the coefficients c_1, c_2 which play roles of pressure). Figure 4.11 displays the solution of the SOHR model for the case 7. It shows that when the convection velocity β_1 is small enough, the solution becomes regular. By performing simulation for case 2 with initial condition $\rho_0 = 1$ (see the solution in figure 4.5) and $\rho_0 = 0.1$ (see the solution in figure 4.10), the solution is singular with $\rho_0 = 1$ but regular with $\rho_0 = 0.1$. Therefore, the existence of numerical solution of the SOHR model depends on the relationship between the coefficients and on the initial condition ρ_0.

We can explain part of this dependence by the maximum principle. Indeed, from the maximum principle, if $\Delta\rho(t, x_0) < 0$ for all $t \in [0, T]$, there exists a positive constant c_0 such that $\Delta\rho(t, x_0) \leq -c_0$. Then we have

$$\rho(t, x) \leq \rho_{max} \exp\Big(\int_0^t (\beta_1 \|\nabla_x \psi(\cdot, s)\|_{L^\infty(\Pi^2)} - \beta_2 c_0) ds \Big). \tag{4.3.38}$$

where $\rho_{max} = \max_{[0,10]} \rho(x, 0)$ and $\Omega = (\cos\psi, \sin\psi)$. The maximal value of the density is an exponential function of time t. So, if $\beta_2 = 0$ or β_2 is too small, this maximal value increases very fast when t pass a value $t_0 > 0$. It could reach a very large number, the numerical solution should blow up. By contrast, if β_2 is large enough to dominate $\beta_1 \|\nabla_x \psi(\cdot, s)\|_{L^\infty(\Pi^2)}$, the solution is bounded by ρ_{max}. This leads to the existence of numerical solution on longer interval $[0, T]$. The numerical results also reveal that in the presence of the unstable term $-\beta_4 \rho(\nabla\rho \cdot \nabla)\Omega$, the coefficient of the diffusion terms (including the parameters which play the role of pressure) need to

be large enough to prevent the unstability of the solution. On the other hand, Theorem 4.2.1 says that there exists a time $T > 0$ such that the theoretical solution of the SOHR model exists locally on interval $[0, T]$. However, we don't know exactly the time T. Therefore, when numerical solution of the system pass the time T, the program of computation will give wrong values of solution. This explains the unstability of the numerical solutions of the SOHR model in some cases of coefficients.

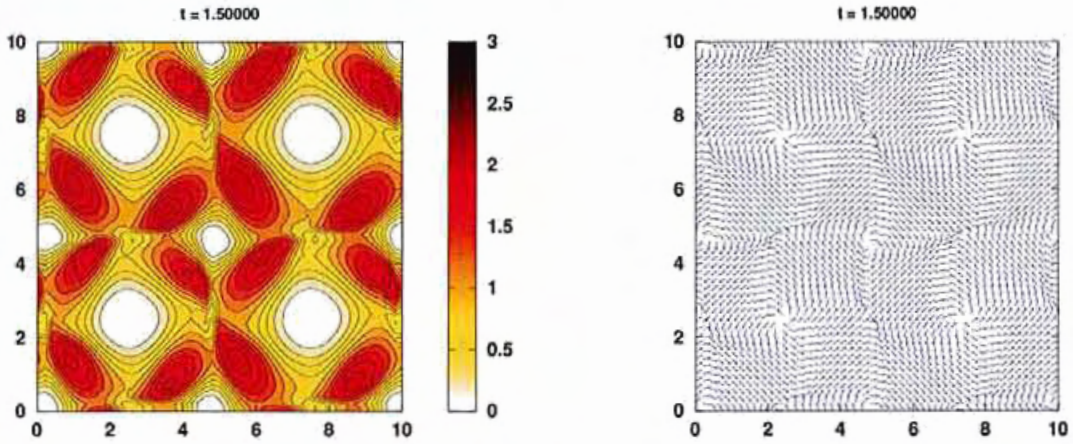

(a) density ρ (b) Ω

Figure 4.4: The solution of the SOHR model for $\beta_2 = 0, \beta_4 = 0.3, \gamma = 0.1, c_2 = 0.2$

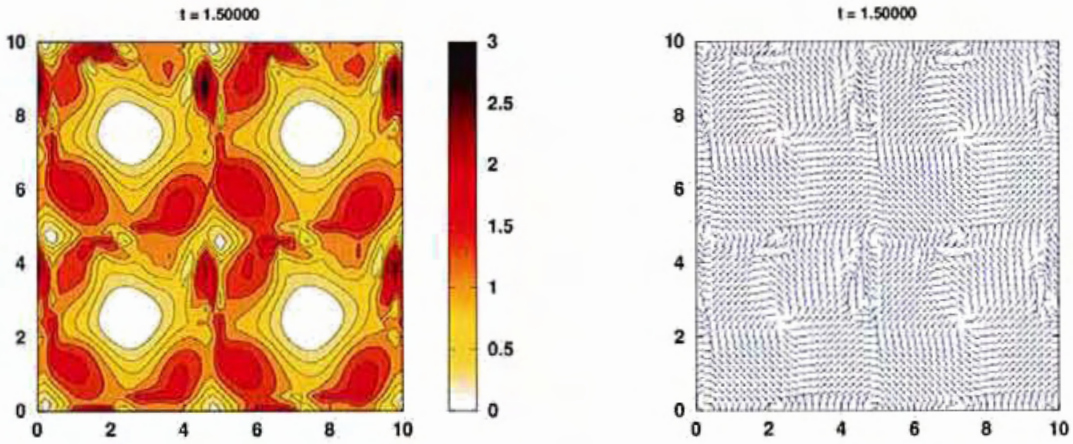

(a) density ρ (b) Ω

Figure 4.5: The solution of the SOHR model for $\beta_2 = 0, \beta_4 = 0.8, \gamma = 0.1, c_2 = 0.2$

4.4 Conclusion

In this chapter, we have studied the existence of solution of a macroscopic model for a system of self-propelled particles with alignment and repulsion in two dimensions. On one hand, we have proved existence of solutions by using the modified Garlerkin method for quasi-linear parabolic

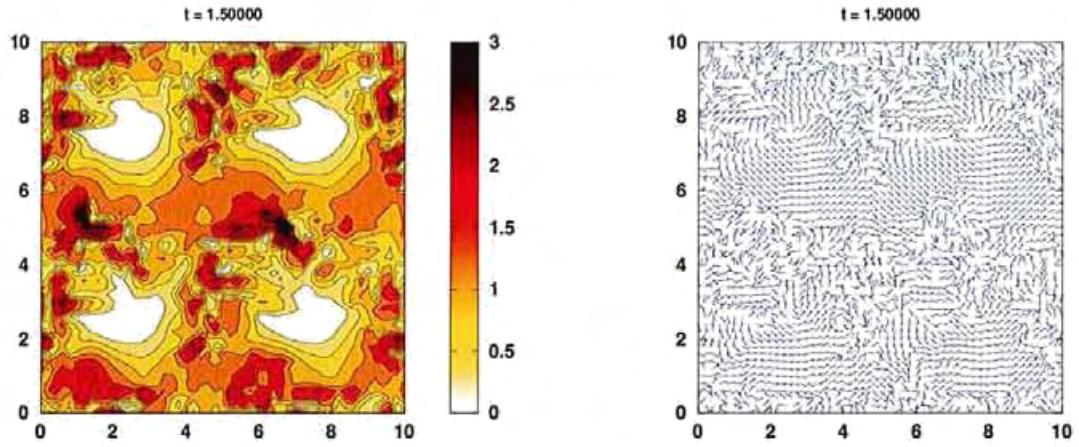

(a) density ρ (b) Ω

Figure 4.6: The solution of the SOHR model for $\beta_2 = 0, \beta_4 = 2, \gamma = 0.1, c_2 = 0.2$

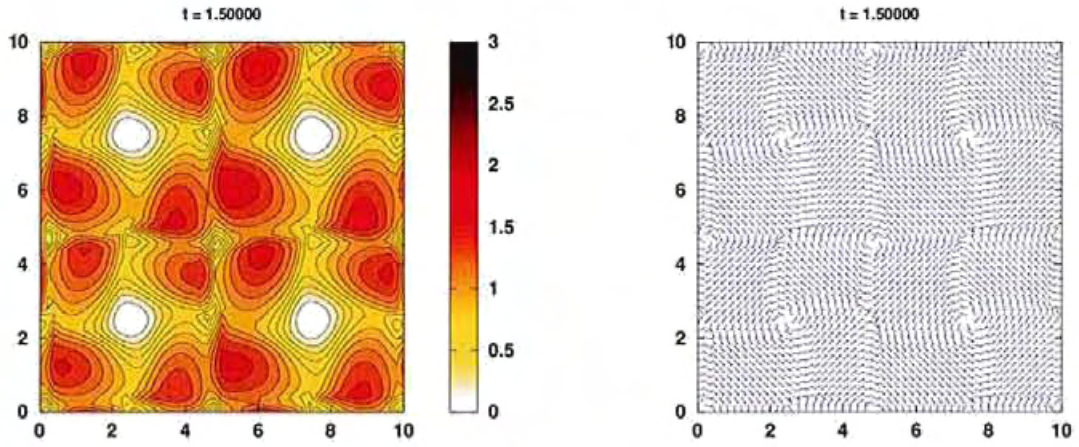

(a) density ρ (b) Ω

Figure 4.7: The solution of the SOHR model for $\beta_2 = 0, \beta_4 = 0.8, \gamma = 0.1, c_2 = 1$

equations. On the other hand, we have also performed simulations to compare theoretical and numerical results. It is a open problem to study the existence of the solution in higher dimensions.

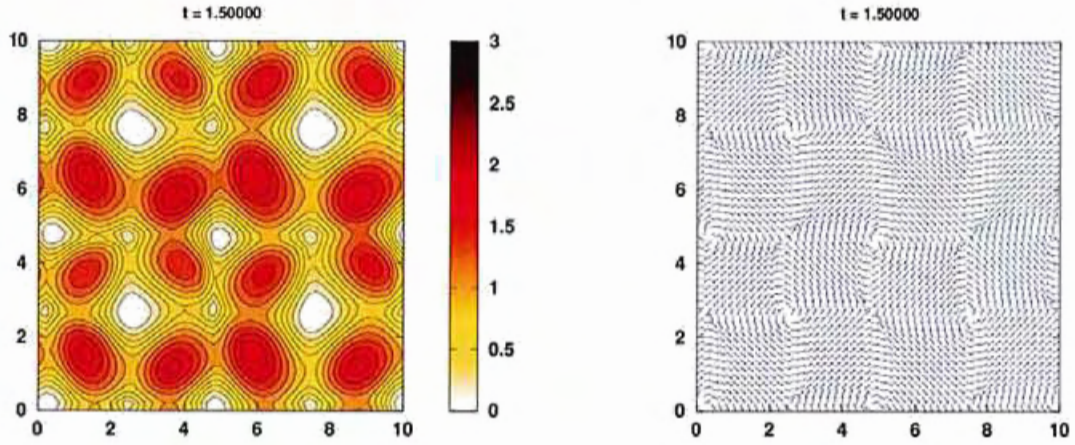

(a) density ρ (b) Ω

Figure 4.8: The solution of the SOHR model for $\beta_2 = 0, \beta_4 = 0.8, \gamma = 0.5, c_2 = 0.2$

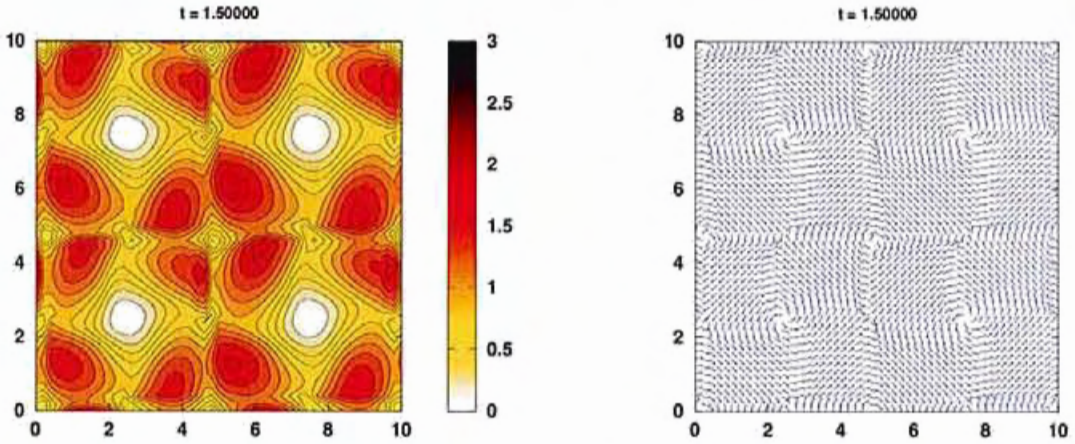

(a) density ρ (b) Ω

Figure 4.9: The solution of the SOHR model for $\beta_2 = 0.6, \beta_4 = 0.8, \gamma = 0.1, c_2 = 0.2$

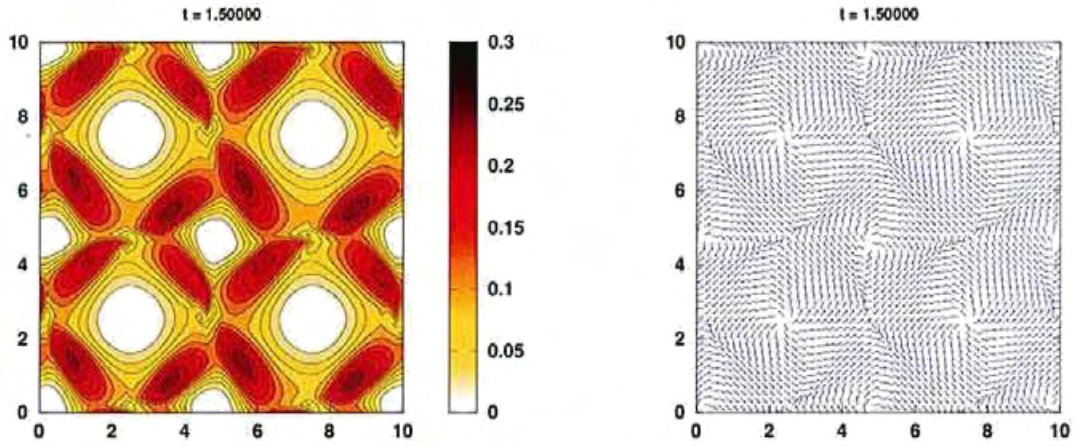

(a) density ρ (b) Ω

Figure 4.10: The solution of the SOHR model for $\beta_2 = 0, \beta_4 = 0.8, \gamma = 0.1, c_2 = 0.2, \rho_0 = 0.1$

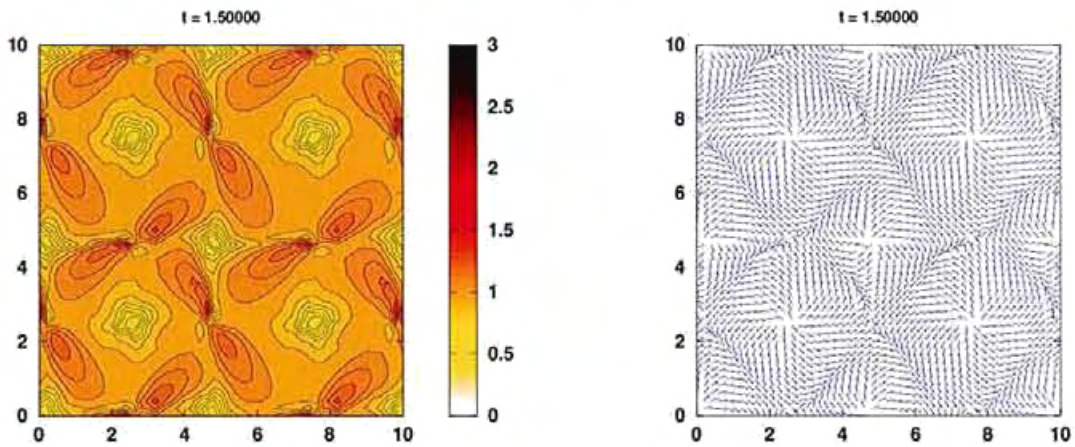

(a) density ρ (b) Ω

Figure 4.11: The solution of the SOHR model for $\beta_1 = 0.1, \beta_2 = 0, \beta_4 = 0.8, \gamma = 0.1, c_2 = 0.2$

Part III: Experiments

Chapter 5

Collective motion of self-propelled robots

This chapter is a work in collaboration with P. Degond, F. Plouraboué, E. Climent, G. Dimarco, O. Praud, N. Wang. The idea of studying collective motion of hexbugs is due to Degond (?). Wang was in charge of the numerical codes to find the positions and the orientations of the hexbugs. The numerical model for the hexbugs is due to Wang. I took care of performing all experiments with Praud and Plouraboué. I have also done data processing, developed and simulated the numerical model thanking to Degond and Plouraboué. Then all of us have met to finish this work.

5.1 Introduction

Large-scale structures can be observed in systems of self-propelled particles with local interaction such as fish school, sperm cell, human crowd, etc. Many models have been proposed to capture and describe such phenomena. The Vicsek model [93] is considered as the simplest model which exhibits collective behavior. In this model, point particles move with constant speed and tend to align their direction to the average direction of their neighbors. This model also exhibits phase transition where all particles move in the same direction. Moreover, elongated self-propelled particles interact by steric interaction as in [75] also resulting in alignment. In [64], the authors studied with experiments and simulations collective behavior of vibrated polar rods. They showed that self-propelled particles aggregate at the boundary of arena. A similar phenomena also occurs for vibrated polar disks [35, 36, 95].
In this work, we report on experiments conducted on simple robots (hexbugs) and simulations where elongated polar self-propelled particles are used (see figure 5.9). We find a similar phenomena as [35, 64] observed for vibrated polar particles. After some transient time, the bugs aggregates and collectively align perpendicularly to the domain boundary. This phenomena occurs even with small packing fraction. In order to model this collective behavior, we build a microscopic model in which particles interact through volume exclusion and change their angular velocity as they hit a wall or collide. The amplitude of angular acceleration depends on that of repulsive force. Our model is able to reproduce qualitatively the behaviors of hexbugs. Most of our findings, are similar to that of Giomi et coauthors [50], a reference that we found lately. [50] also performed experiments and simulations on elongated self-propelled robots in circular confined domain, using individual tracking and simulations. They provide a phase diagram for the collective pattern of motion with three states: Swirling, stasis and disordered. The first phase corresponds to the formation of mobile clusters near the boundary with local orientation close to tangent. The second one, is the same as the first one except for the clusters are non-mobile and orthogonal to the local tangent. Finally the disordered phase corresponds to no apparent collective structures. In the phase space they

observed that for high density and high speed the swirling phase is predominant, and, that bellow a critical density, disorder prevails.

Our experiments are performed into an annular domain, and mainly display two phases: Stacked and disordered where stacking phase appears when bugs are locally align perpendicularly to the boundary whereas they gently move along it. Nevertheless, some aspects of our observations and analysis are original, and will try to focus on those in the following.

5.2 Results

The experimental setup is detailed in the "Material and Methods" section. Bugs were confined in annular arenas. We use two rings with different values of radius R_{in}, R_{out}. Observing the motion of each pair of hexbugs in the first ring, most of the bugs move along circles of various radii and change their direction of motion after colliding. Figure 5.1 shows the mean speed of 12 different pairs of bug during 100 seconds.

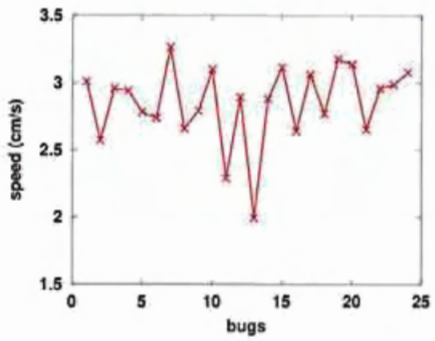

Figure 5.1: The average speed of 12 different pairs of bugs as they move in the experimental ring.

Observing the motion of the bugs in the confined ring, the particles align perpendicularly to the boundary so as to form clusters as we increase the number of hexbugs in the ring (figure 5.3a). If the total number of the hexbugs in the ring are small ($N \leq 12$ corresponding to packing fraction $\phi \leq 0.08$ in the first ring), the lifetime of clusters is short. The larger the number of hexbugs in a cluster is, the longer lifetime of the cluster is. In this case, the cluster will move slowly along the boundary of the ring. However, as the packing fraction is large, it causes jamming phenomena of the hexbugs. Figure 5.2 illustrates the motion of clusters in time for one of the experiments with 15 bugs in the first ring.

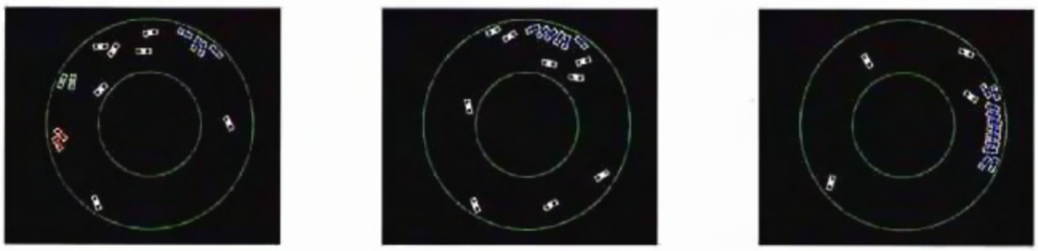

(a) clusters at time t_0(s) (b) clusters at time $t = t_0 + 0.6$ (s) (c) clusters at time $t = t_0 + 10$ (s)

Figure 5.2: Snapshots of the clusters motion at successive times for one experiment with 15 bugs. Clusters are coded in different colors.

Based on experimental observations, we propose a microscopic model where particles interact through volume exclusion. Each particle move due to a swimming velocity and angular velocity. The repulsive force will act on the particle if one particle is close to another one or to the boundary. Angular acceleration decreases due to a frictional force with frictional coefficient β. The model is described in detail in the section 5.4.4. This model is able to reproduce qualitatively these behaviors. Figure 5.3a, 5.3b illustrate the particles aggregate at the boundary of the ring to form clusters for experiment and simulation, respectively. To study this phenomena, we focus on clusters at the boundary. Figure 5.4 shows clusters (white stripes) for one experiment with 10, 15 bugs in the first ring. Figure 5.5 shows clusters for one experiment with 20 bugs and 30 bugs in the second ring.

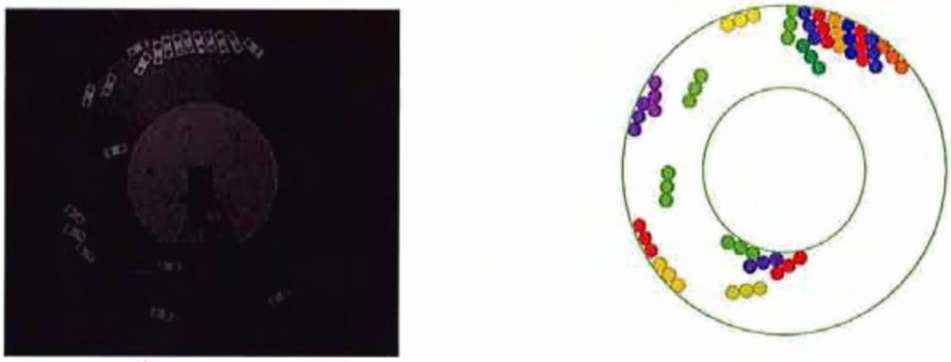

(a) experiment (b) model

Figure 5.3: Snapshots illustrate the movement of 20 bugs in the arena (figure 5.3a) and for model (fig 5.3b).

(a) 10bugs (b) 15bugs

Figure 5.4: This figure illustrates the motion of clusters for one of the experimental replications with 10, 15 bugs in the first ring. Horizontal axis show values of angle φ in polar coordinates and vertical axis is time, running downwards.

Clusters are defined as connected components of binary image 5.5. More details about clusters identification et segmentation can be found in the 'Materials and Methods' section. We focus on some characteristics of clusters like size and lifetime. For this purpose, we conduct experiments with 10, 15, 20, 30 hexbugs. In order to compare characteristics of clusters and compare them with the model prediction in the section 5.4.4. We then perform simulations with time step $\Delta t = 0.001$ for time $T = 20$ seconds. The time step has been chosen so that very few overlapping is observed

(a) 20bugs (b) 30bugs

Figure 5.5: This figure illustrates the motion of clusters along the border for one of the experimental replications with 20, 30 bugs in the second ring using a space-time diagram. The angular position of each clusters frontier has been segmented and represented in black (no cluster) and white (cluster) images. Horizontal axis show values of angle φ in polar coordinates and vertical axis is time, running downwards. As time goes by, one can see that larger and larger clusters emerge from the dynamic, so that after a transient, only one big drifting cluster is form, the velocity of which is related to the local slope of the white stripes.

during collisions as repulsive forces acts on each particle. Furthermore, the total dimensionless time $T = 20$ seconds has been chosen so as to match the one used in the experiments (it has been made dimensionless by convective time $\tau = 6r_b/v_0$ where $6r_b$, v_0 are the bug length and the bug speed, respectively.

Parameters of the microscopic model have been chosen as follows: $v_0 = 0.5$, $F_0 = 50$, $\lambda = 7$, $\beta = 1.5$, $r = 0.205$. Figure 5.6 shows size distribution and lifetime distribution of clusters for both experiment and model with 20 (figure 5.6a) and 30 bugs (figure 5.6b).

This figure shows a excellent match between the model and the experiment for the size distribution of clusters. However, the density of the lifetime of clusters obtained from experiments is more concentrated near zeros than the one obtained from simulations.

Figures 5.7a, 5.7b show lifetime distribution in log-log scale with different number of bugs for both the experiments and the model, respectively. The observed behavior is close to a power-law distribution, whose slope similar from one experiment to another one and close to -2, so that the slope looks independent of the bug number.

This is the signature of a universal dynamics to reach the stacking phase, so that we found that the stacking phase establishment follows a critical law whose exponent does not depend on the distance to the critical order parameter (the critical density) since the exponent weakly depends on the bugs number for a given arena. It is striking to observed that the exponent found from the simulations is very similar to the one found from the experiments.

Figure 5.8 shows mean speed as function of inverse mean size of clusters. We just compute speed for clusters that lifetime is more than 2 seconds. This figure shows that the larger mean size of clusters is, the smaller mean speed is.

5.3 Discussion

In this work, we have studied experimentally the emergence of clusters of the hexbugs confined into an annular domain to reach a steady collective motion. We show the stacking phase which is close to the static phase of Giomi et al [50] so that self-propelled elongated particles can exhibit new organization of motion where the particles align orthogonally at the boundary of the arena

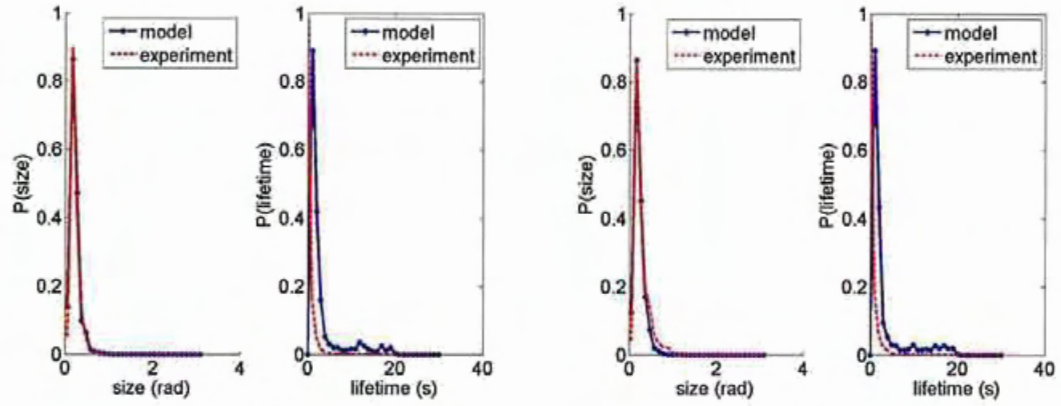

(a) 20bugs (b) 30bugs

Figure 5.6: Size distribution and lifetime distribution of clusters for the experiments with 20 bugs and 30 bugs. The parameters for the microscopic model are chosen as follows: $v_0 = 0.5$, $F_0 = 50$, $\lambda = 7$, $\beta = 1.5$, $\Delta t = 0.001$, $n = 3$, $r_b = 0.1$, $m_b = 1$ and $r = 0.205$.

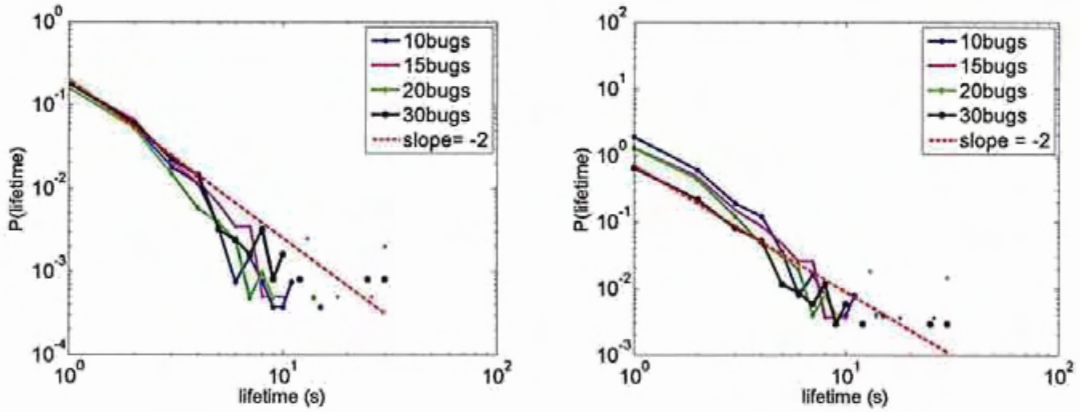

(a) for the experiments (b) for the model

Figure 5.7: Lifetime distribution of clusters in log-log scale for the experiments (figure 5.7a) and the model (figure 5.7b) with the different number of bugs 10bugs (blue), 15bugs (magenta), 20bugs (green), 30bugs (black) and a red line of slope -2.

to form clusters. We have also built a model which is able to reproduce qualitatively the collective behavior of the stacking phase and found some universal critical dynamics to stacking phase.

5.4 Material and Methods

5.4.1 Experimental setup and data processing

In order to investigate the emergence of collective motion in systems of elongated self-propelled particles which interact through volume-exclusion interactions, experiments with simple self-propelled robots were performed in 2013 at the IMFT, France. A system consisting of 80 Hexbug (see fig 5.9) was used. Bugs have been placed in ring shaped arena with inner radius R_{in} and outer radius

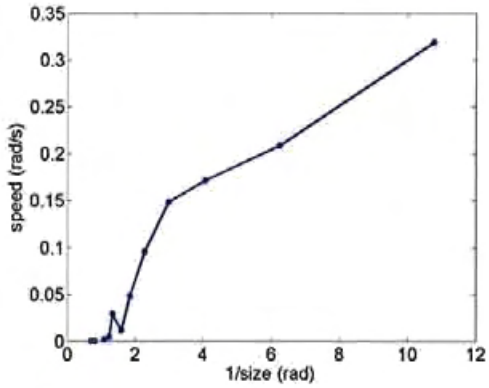

Figure 5.8: Mean speed of clusters in versus of inverse mean size of clusters for all experiments.

R_{out}. Two rings were used with different values of radius R_{in}, R_{out}. The inner and outer radius of the first ring are $R_{in} = 12\text{cm}, R_{out} = 20.5\text{cm}$. For the second ring, the outer radius is fixed by $R_{out} = 35.5\text{cm}$ and the inner radius is 15.5cm. In order to prevent the bugs from flipping, the rings were covered by a glass (see fig 5.3). Two digital cameras (PCO SCMOS camera and PCO 2000 camera) were used to capture the motion of the hexbugs at a rate of 10 frames per second. All frames of the first camera have the same resolution which is 2560×2160 pixels and that of the second one is 2048×2048 pixels.

Figure 5.9: A self-propelled robot of the brand Hexbug: a small battery-powered electric engine triggers the vibration of the device. The bended plastic legs offer differential friction with the substrate. As a result, the device moves ahead. Due to unbalanced bending, most of these devices move along circles of various radii.

To measure the position and the orientation of each bug we regard their movement in two dimensions. For this purpose, a rectangular tag (see fig 5.10a) was attached to the back of the hexbug. The tag allows us to label the hexbug. The position of the hexbug is defined by the centre of the tag (the point O in fig 5.10b). The orientation of the bug (the vector AX in fig 5.10b) is the outward pointing normal vector placed at the centre of the hole (the point A), which is parallel to the line OA.

A reference is always captured for each session to reduce noise of images. The movies of 12 pairs of the hexbugs with new batteries were firstly recorded to compute their mean velocity. In order to observe the emergence of collective behavior of the bugs, we have performed successively experiments with the first ring for 10, 15, 20 bugs. With the second ring, movies were also taken for 15, 20, 25, 30 bugs.

(a) A bug attached tag

(b) a tag

Figure 5.10: A bug is labelled by a tag.

5.4.2 Data analysis

Images recorded for each session were analyzed according to the following data:

- We assigned a code number identifying for each bug and this number was fixed throughout a session.
- Data of each bug consists of the number of frame, its position and its orientation according to this frame.
- The position of the centre of the ring.

All recorded images were converted to binary images with a given value threshold. Each bug is correspond to a connected component of binary images. The position of the bug was described as the center of mass of the connected component with no holes. Similarly, we also compute the center of mass of the circle which allows us to define the orientation of the bug. In order to find out to which bug each connected component is related in the library, we compare it to all the bugs in the library from a pixel based error distance. Error distance of this connected component to each element in the bug library is computed by the sum of all pixels where two images are different. The code number of this connected component is the index of the bug in the library for which the obtained error distance is minimum. Because of the noise, the program could not find out the position of some connected components or, in some case error distance might have several minima. In these cases, the program was run with different image thresholds. If the program still find no solution, the bug position in these frames were computed by linear interpolation. Sum of all frames for each bug that we could not find out the position is always less than 5%.

5.4.3 Clustering Method

The collected data give access to the two dimensional Cartesian coordinates $(x_i, y_i, \theta_i)(t^n)$ of each bug. In polar coordinate, the position of each bug is defined by a pair $(r_i, \varphi_i)(t^n)$

$$x_i = r_i \cos\varphi_i + x_{center}, \quad y_i = r_i \sin\varphi_i + y_{center} \tag{5.4.1}$$

where x_{center}, y_{center} is the center of the ring in the Cartesian coordinate and $t^n = n\Delta t$ with $\Delta t = 0.1$s.

Cluster: Two bugs belong to the same cluster at a given moment of time if their positions satisfy the following conditions

- They move close to outer boundary
- They move close together
- Their lifetime needs to be more than a time t_0.

In order to determine whether the i-bug and j-bug belongs to the same cluster, we construct a N-by-N adjacency matrix A with N is the number of the bugs in a experiment, given by.

$$A(i,j) = \begin{cases} 1, & \text{if i-bug and j-bug belong to the same cluster} \\ 0, & \text{otherwise} \end{cases} \tag{5.4.2}$$

Therefore, the number of clusters corresponds to the connected component of the adjacency matrix of the bugs neighbour graph. The number of bugs for one cluster is the number of nodes in the connected component in this matrix.

Cluster (velocity, size, lifetime) We assume that the bugs $(r_i, \varphi_i)_{i\in I}(t^n)$ belong to the same cluster. We denote cluster boundaries $(\varphi^n_{max}, \varphi^n_{min})$ at time t^n by

$$\varphi^n_{max} = \max_{i\in I} \varphi_i(t^n), \quad \varphi^n_{min} = \min_{i\in I} \varphi_i(t^n).$$

We define the size of the cluster is the smallest angle formed between φ^n_{max} and φ^n_{min}. In order to calculate lifetime of clusters, we construct a lattice in the angular-time 2D space (φ_i, t^n) where $\varphi_i = i\Delta\varphi - \pi$, and $t^n = n\Delta t$. The point (φ_i, t^n) takes value 1 if φ_i belongs to the interval $[\varphi^n_{min}, \varphi^n_{max}]$ and takes 0 in otherwise cases. Then we obtain a binary image of clusters (see figure 5.4, 5.5). Clusters are defined as connected components of this binary image. This allows us to compute lifetime and boundaries of clusters. Figures 5.11, 5.12 show the boundaries of clusters corresponding to the experiments shown in figure 5.4, 5.5.

The characteristics of clusters have studied in clusters of pedestrians [70]. However, in this paper, the authors defined a cluster in an other way. In order to reduce oscillations of the boundaries of clusters, we filter them by convolution in time with a truncated Gaussian function with a support larger than $\Delta\varphi$. The cluster boundary velocity is estimated by the time derivative of the cluster boundary.

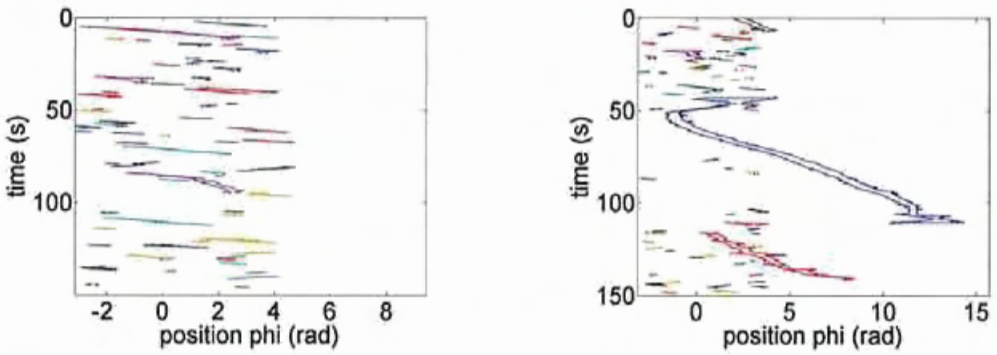

(a) 10bugs (b) 15bugs

Figure 5.11: This figure illustrates the boundary of clusters for one of the experimental replications with 10, 15 bugs corresponding to the experiments shown in figure 5.4. Horizontal axis show values of angle φ in polar coordinates and vertical axis is time, running downwards.

5.4.4 Simulation Model

In order to describe the stacking phenomena of the bugs, we constructed a mechanical model which is able to reproduce experimental behavior of the hexbugs. We consider a system of N-rod particles. Each rod particle consists of n-beads with its radius r_b and its mass m_b. Let $X_i(t) \in \mathbb{R}^2$ denote the centre position of i-rod at time t, and $v_i(t), \omega_i(t), \Omega_i(t)$ denote the velocity, the orientation and

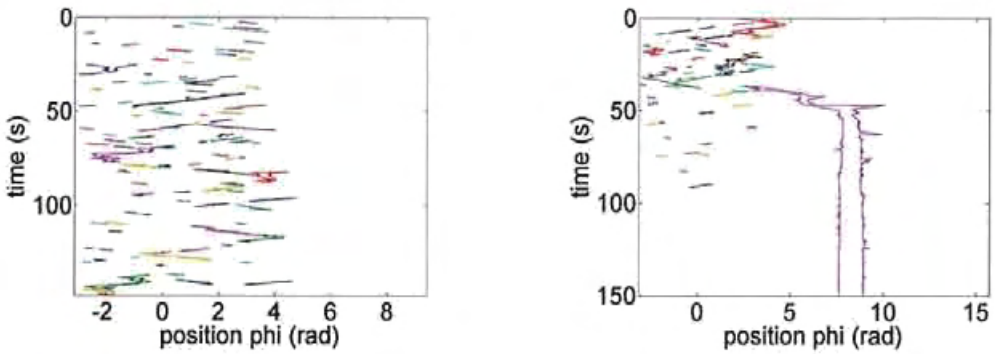

(a) 20bugs (b) 30bugs

Figure 5.12: This figure illustrates the boundary of clusters for one of the experimental replications with 20, 30 bugs corresponding to the experiments shown in figure 5.5. Horizontal axis show values of angle φ in polar coordinates and vertical axis is time, running downwards.

the angular velocity, respectively. The position of the j-th bead of the i-th rod X_{ij} is computed by the following formula:

$$X_{ij} = X_i + \omega_i\Big[\big(-(n-1)+2(j-1)\big)r_b\Big].$$

A rod interact to an other rod or to boundary due to a repulsive force F_i. This force make the rod change its angular velocity. This angular velocity will tend to 0 due to a dynamic frictional force $-\beta\Omega_i I_i$ with friction parameter β. The dynamics are described by the following equations:

$$\frac{dX_i}{dt} = v_i, \tag{5.4.3}$$

$$m\frac{dv_i}{dt} = \lambda(v_o\omega_i - v_i) + F_i, \quad I_i\frac{d\Omega_i}{dt} = \tau_i - \beta\Omega_i I_i. \tag{5.4.4}$$

where the mass of the rod m is equal nm_b. The repulsive force F_i acts on each rod given by

$$F_i = \sum_{j=1}^{n}\sum_{\substack{k=1,N\\ l=1,n}} F_{ijkl}$$

where $F_{ijkl} = F(X_{ij} - X_{kl})$ is the repulsive force between the j-th bead of the i-th rod and the the l-th bead of the k-th rod, given by

$$F(x) = \begin{cases} F_0\dfrac{x}{|x|}\left(1 - \dfrac{|x|}{r}\right) \text{ if } |x| < r \\ 0 \quad \text{otherwises.} \end{cases} \tag{5.4.5}$$

The coefficients λ, F_0 represent the intensities of self-propulsive and repulsive force, respectively. The torque τ_i and the moment of inertia I_i are given by

$$\tau_i = \sum_{j=1}^{n}\Big((X_{ij} - X_i) \times \sum_{\substack{k=1,N\\ l=1,n}} F_{ijkl}\Big)$$

$$I_i = \sum_{j=1}^{n} |X_{ij} - X_i|^2 m_b.$$

The boundary condition: The boundary condition chosen is repulsive. When a rod is close to the boundary of the ring, a repulsive $F_{boundary}$ acts on this rod make it change the orientation of the motion. This force is computed by

$$F_{boundary}(x) = \begin{cases} F_0 \frac{x}{|x|}(1 - \frac{R_{out} - |x|}{r_{boun}}) \text{ if } R_{out} - |x| < r_{boun} \\ F_0 \frac{x}{|x|}(1 - \frac{|x| - R_{in}}{r_{boun}}) \text{ if } |x| - R_{in} < r_{boun} \\ 0 \quad \text{otherwises.} \end{cases} \tag{5.4.6}$$

The parameters: In order to compare some cluster characteristics of the experiment with those of the model, we perform simulations for the model. The parameters are chosen as followings: $r_b = 0.1$, $r_0 = 0.5$, $n = 3$, $\lambda = 7$ $F_0 = 50$, $r = 0.205$, $r_{boun} = 0.105$, $\beta = 1.5$, $m_b = 1$. This leads to chose $\Delta t = 10^{-3}$. Indeed, parameters β should verify $\Delta t \ll 1/\beta$ so that the time step Δt permits to capture the angular relaxation time $1/\beta$ due to the friction parameter β. Similarly, since the dimension of λ, denoted by $[\lambda] = m/T$ and $m = nm_b = 3$, we set $3/\lambda$ a typical relaxation time for velocity, which should be chosen as $3/\lambda \gg \Delta t$ (here $3/7 \gg 10^{-3}$). Finally, there is a third characteristic time in the model, provided by the angular relaxation (5.4.4), given by $T \sim \sqrt{mnr_b/F_0}$ and the time step should also verify $\Delta t \ll \sqrt{mnr_b/F_0}$, which in our case given for $m = 3$, $r_b = 0.1$, $F_0 = 50$, is verified since $1/7 \gg 10^{-3}$. To ensure packing fraction being equal between simulations and experiments, we chose $R_{in} = 1.2$, $R_{out} = 2.4$ for the first ring and $R_{in} = 1.45$, $R_{out} = 4.25$ for the second ring. With these choices, the model can be consider as an overdamped model.

Conclusion

In this thesis, we have studied theoretically and numerically models of self-propelled particles such as fish school, sperm cells, etc. In chapter 1 we have derived hydrodynamic models for systems of noisy self rotating particles in plane. The particles have angular velocities and interact through alignment rule. In the first one where proper rotation is small compared with the alignment interaction. In this regime, the hydrodynamic limit yields the SOH (Self-Organized Hydrodynamic) model with an addition term from the angular velocity. In the second one, where the proper rotation is of the same order as the alignment interaction This changes the equilibrium velocity distribution of the particles. In order to preserve the propensity of the particles align with their neighbors, we modify the interaction force. The obtained hydrodynamic model involves significant modifications compared with the SOH model.

We have also proposed a new model for motion of self-propelled particles which interact through alignment and repulsion. In chapter 2, a macroscopic model (which is called Self-Organized Hydrodynamic with Repulsion or SOHR model) have been derived from the corresponding microscopic model. To numerically validate this hydrodynamic model, we have studied its numerical solutions and compare them with those of the particle model. Existence of this continuum model has been considered for both theory and simulations in chapter 3. We have proved the local existence of solution in two dimensions. On the other hand, we have performed simulations to compare the numerical and theoretical results.

Finally in chapter 4 we have investigated collective behaviors of simple robots (hexbug) into an annular domain. Our experiments display two phases: stacked and disordered where stacking phase appears when bugs are locally align perpendicular to the boundary whereas they gently move along it. Some characteristics for clusters like size and lifetime have investigated. We also built a microscopic model which is able to reproduce quantitatively this phenomena.

There are some directions in which we can extend known works in the literature. In the chapter 2, perspective include a deeper analytical study of the models, such as proving linearized stability in general case and local well-posedness of smooth solutions. Simulations will be performed to validate the models.

We have derived macroscopic models from microscopic models via kinetic equations. However all mean field limits and hydrodynamic limits are formal. Therefore, it is necessary to study theoretical framework for these limits. It would also be interesting to find weak solution of the SOHR model.

For futur study we would like to consider binary collision, collective properties of system of hexbugs such as the probability density function of angle before and after collision. We expect that this study will develop a model of interaction between hexbugs based on experimental data.

It would be interesting to study collective behaviors from kinetic equations. We could perform simulations for kinetic equations to compare with those of microscopic models and macroscopic models.

Bibliography

[1] J. A. Acebrón, L. L. Bonilla, C. J. Pérez Vicente, F. Ritort, R. Spigler, The Kuramoto model: a simple paradigm for synchronization phenomena, Rev. Mod. Phys., 77 (2005) 137 185.

[2] M. Aldana, V. Dossetti, C. Huepe, V. M. Kenkre, H. Larralde, Phase transitions in systems of self-propelled agents and related network models, Phys. Rev. Lett., 98 (2007), 095702.

[3] I. Aoki, A simulation study on the schooling mechanism in fish, Bulletin of the Japan Society of Scientific Fisheries, 48 (1982) 1081-1088

[4] A. Barbaro, P. Degond, Phase transition and diffusion among socially interacting self-propelled agents, Discrete Contin. Dyn. Syst. Ser. B, to appear.

[5] A. Baskaran, M. C. Marchetti. Hydrodynamics of self-propelled hard rods. Phys. Rev E 77 (2008) 011920.

[6] A. Baskaran, M. C. Marchetti. Nonequilibrium statistical mechanics of self-propelled hard rods, J. Stat. Mech. Theory Exp., (2010) P04019.

[7] N. Bellomo, J. Soler, On the mathematical theory of the dynamics of swarms viewed as complex systems. *Math. Models Methods Appl. Sci.* 22, Supp. 1 (2012) 11-40006.

[8] F. Berthelin, P. Degond, V. Le Blanc, S. Moutari, J. Royer, M. Rascle, A Traffic-Flow Model with Constraints for the Modeling of Traffic Jams, Mathematical Models and Methods in Applied Sciences 18, Suppl. (2008), pp. 1269-1298

[9] E. Bertin, M. Droz and G. Grégoire, Hydrodynamic equations for self-propelled particles: microscopic derivation and stability analysis, J. Phys. A: Math. Theor., 42 (2009) 445001.

[10] L. Bertini, G. Giacomin, K. Pakdaman, Dynamical aspects of mean field plane rotators and the Kuramoto model, J. Stat. Phys., 138 (2010) 270-290.

[11] L. Bertini, G. Giacomin, C. Poquet, Synchronization and random long time dynamics for mean-field plane rotators, preprint arXiv:1209.4537.

[12] F. Bolley, J. A. Cañizo, J. A. Carrillo, Mean-field limit for the stochastic Vicsek model, Appl. Math. Lett., 25 (2011) 339-343.

[13] F. Bolley, J. A. Cañizo, J. A. Carrillo, Stochastic Mean-Field Limit: Non-Lipschitz Forces & Swarming, Math. Models Methods Appl. Sci., 21 (2011) 2179-2210.

[14] M. Bostan and J. A. Carrillo, Asymptotic Fixed-Speed Reduced Dynamics for Kinetic Equations in Swarming, Preprint UAB

[15] J. A. Carrillo, M. Fornasier, J. Rosado, G. Toscani, Asymptotic Flocking Dynamics for the kinetic Cucker-Smale model, SIAM J. Math. Anal., 42 (2010) 218-236.

[16] H. Chaté, F. Ginelli, G. Grégoire, F. Raynaud, Collective motion of self-propelled particles interacting without cohesion, Phys. Rev. E 77 (2008) 046113.

[17] Z. Chen, H. T. Zhang, No-beacon collective circular motion of jointly connected multi-agents, Automatica, 47 (2011), 1929-1937.

[18] A. A. Chepizhko, V. L. Kulinskii, On the relation between Vicsek and Kuramoto models of spontaneous synchronization, Physica A, 389 (2010) 5347-5352.

[19] Y-L. Chuang, M. R. D'Orsogna, D. Marthaler, A. L. Bertozzi and L. S. Chayes, State transitions and the continuum limit for a 2D interacting, self-propelled particle system, Physica D, 232 (2007) 33-47.

[20] I. D. Couzin, J. Krause, R. James, G. D. Ruxton and N. R. Franks, Collective Memory and Spatial Sorting in Animal Groups, J. theor. Biol., 218 (2002), 1-11.

[21] F. Cucker, S. Smale, Emergent behavior in flocks, IEEE Transactions on Automatic Control, 52 (2007) 852 862.

[22] A. Czirók, E. Ben-Jacob, I. Cohen, T. Vicsek, Formation of complex bacterial colonies via self-generated vortices. Phys. Rev. E, 54 (1996) 1791-18091.

[23] A. Czirók, T. Vicsek, Collective behavior of interacting self-propelled particles. Physica A 281 (2000), 17-29.

[24] P. Degond, A. Frouvelle, J-G Liu, Macroscopic limits and phase transition in a system of self-propelled particles, J. Nonlinear Sci., appeared online.

[25] P. Degond, A. Frouvelle, J.-G. Liu,S. Motsch, L. Navoret, Macroscopic models of collective motion and self-organization, submitted. arXiv:1304.6040.

[26] P. Degond, A. Frouvelle J.-G. Liu, A note on phase transitions for the Smoluchowski equation with dipolar potential, submitted.

[27] P. Degond, A. Frouvelle, J-G. Liu, Phase transitions, hysteresis, and hyperbolicity for self-organized alignment dynamics, preprint.

[28] P. Degond, J. Hua, Self-Organized Hydrodynamics with congestion and path formation in crowds, Journal of Computational Physics. 237 (2013), pp. 299-319

[29] P. Degond, S. Motsch, Continuum limit of self-driven particles with orientation interaction, Math. Models Methods Appl. Sci., 18 Suppl. (2008) 1193-1215.

[30] P. Degond, S. Motsch, Large scale dynamics of the Persistent Turning Walker model of fish behavior, J. Stat. Phys., 131 (2008) 989-1021.

[31] P. Degond, S. Motsch, A macroscopic model for a system of swarming agents using curvature control, J. Stat. Phys., 143 (2011) 685-711

[32] P. Degond, J-G. Liu, S. Motsch, V. Panferov, Hydrodynamic models of self-organized dynamics: derivation and existence theory, Methods Appl. Anal., to appear.

[33] P. Degond, L. Navoret, R. Bon, D. Sanchez, Congestion in a macroscopic model of self-driven particles modeling gregariousness, J. Stat. Phys., 138 (2010), pp. 85-125.

[34] P. Degond, P. F. Peyrard, G. Russo, Ph. Villedieu, Polynomial upwind schemes for hyperbolic systems, C. R. Acad. Sci. Paris, Ser I, 328 (1999) 479-483.

[35] J. Deseigne, O. Dauchot and H. Chaté, Collective motion of vibrated polar disks. Phys. Rev. Lett., 105 (2010).

[36] J. Deseigne, S.Léonard, O.Dauchot, and H.Chaté, Vibrated polar disks: spontaneous motion, binary collisions and collective dynamics, Soft matter, 8 (2012), 5629.

[37] D'Orsogna, M., Chuang, Y., Bertozzi, A., Chayes, L., Self-propelled particles with soft-core interactions: patterns, stability, and collapse. Phys. Rev.Lett. 96(10), 104,302 (2006).

[38] J. Dunstan, Gastón Miño, E. Clement, R. Soto, A two-sphere model for bacteria swimming near solid surfaces, Phys. Fluids 24 (2012), 011901.

[39] W. M. Durham, J. O. Kessler, R. Stocker, Disruption of vertical motility by shear triggers formation of thin phytoplankton layers, Science 323 (2009), 1067-1070.

[40] W. M. Durham, E. Climent, R. Stocker, Gyrotaxis in a Steady Vortical Flow, Phys. Rev. Lett. 106 (2011), 238102.

[41] H.Fehske, R. Schneider and A. Weisse, Computational Many-Particle Physics, Springer Verlag, 2007.

[42] M. Fornasier, J. Haskovec, G. Toscani, Fluid dynamic description of flocking via the Povzner-Boltzmann equation, Phys. D, 240 (2011), 21-31.

[43] A. Frouvelle, A continuum model for alignment of self-propelled particles with anisotropy and density-dependent parameters, Math. Mod. Meth. Appl. Sci., 22 (2012) 1250011 (40 p.).

[44] A. Frouvelle, J.-G. Liu, Dynamics in a kinetic model of oriented particles with phase transition, SIAM J. Math. Anal., 44 (2012) 791-826.

[45] J. Gautrais, C. Jost, M. Soria, A. Campo, S. Motsch, R. Fournier, S. Blanco, G. Theraulaz, Analyzing fish movement as a persistent turning walker, J. Math. Biol., 58 (2009) 429-445.

[46] J. Gautrais, F. Ginelli, R. Fournier, S. Blanco, M. Soria, H. Chaté, G. Theraulaz, Deciphering interactions in moving animal groups. Plos Comput. Biol., 8 (2012) e1002678.

[47] G. Giacomin, E. Luçon, C. Poquet, Coherence stability and effect of random natural frequencies in populations of coupled oscillators, preprint arXiv:1111.3581.

[48] G. Giacomin, K. Pakdaman, X. Pellegrin, C. Poquet, Transitions in active rotator systems: invariant hyperbolic manifold approach, SIAM J. Math. Anal., 44 (2012) 4165-4194.

[49] F. Ginelli, F. Peruani, M. Bar and H. Chaté, Large-Scale collective properties of self-propelled rods, Phys. Rev. Lett., 104 (2010), 184502.

[50] L. Giomi, N. Hawley-Weld and L. Mahadevan, Swarming, swirling and stasis in sequestered bristle-bots. Proc. R. Soc. A 2013, 469.

[51] G. Grégoire, H. Chaté, and Y. Tu. Moving and staying together without a leader. Phys. Nonlinear Phenom., 181: 157-170. (2003).

[52] G. Grégoire, H. Chaté, Onset of collective and cohesive motion, Phys. Rev. Lett., 92 (2004), 025702.

[53] D.Grossman, I.S.Aranson and E.Ben Jacob, Emergence of agent swarm migration and vortex formation through inelastic collisions, New J. Phys., 10 (2008) 023036.

[54] S. -Y. Ha, C. Lattanzio, B. Rubino, M. Slemrod, Flocking and synchronization of particle models, Quart. Appl. Math., 69 (2011), 91-103.

[55] S. -Y. Ha, J.-G. Liu, A simple proof of the Cucker-Smale flocking dynamics and mean-field limit, Commun. Math. Sci., 7 (2009) 297-325.

[56] S.-Y. Ha, E. Tadmor, From particle to kinetic and hydrodynamic descriptions of flocking, Kinetic and Related Models, 1 (2008) 415-435.

[57] C.K. Hemelrijk and H. Hildenbrandt, Self-Organized Shape and Frontal Density of Fish Schools, Ethology, 114(3): 245-254, 2008

[58] S. Henkes, Y. Fily, M. C. Marchetti, Active jamming: Self-propelled soft particles at high density, Phys. Rev. E 84 (2011), 040301.

[59] J. P Hernandez-Ortiz, P. T Underhill, M. D. Graham, Dynamics of confined suspensions of swimming particles, J. Phys.: Condens. Matter 21 (2009) 204107.

[60] R. W Hockney and J. W Eastwood, Computer Simulation Using Particles, Institute of Physics Publishing, 1988.

[61] E. P. Hsu, Stochastic Analysis on Manifolds, Graduate Series in Mathematics, American Mathematical Society, 2002.

[62] G. B. Jeffrey, The motion of ellipsoidal particles immersed in a viscous fluid, Proc. R. Soc. London. Ser A., 102 (1922), 161-179.

[63] Donald L.Koch, Ganesh Subramanian, Collective hydrodynamics of swimming microorganisms: Living fluids, Annu.Rev.Fluid Mech. 2011, 43:637-59.

[64] A. Kudrolli, G. Lumay, D. Volfson and L. S. Tsimring, Swarming and Swirling in Self-Propelled Polar Granular Rods, Phys. Rev. Lett. 100, (2008).

[65] Y. Kuramoto, Chemical Oscillations, Waves, and Turbulence, Springer, 1984.

[66] E. Lauga, W. R. DiLuzio, G. M. Whitesides, H. A. Stone, Swimming in circles: motion of bacteria near solid boundaries, Biophysics Journal, 90 (2006), 400-412.

[67] E. Luçon, Large time asymptotics for the fluctuation SPDE in the Kuramoto synchronization model, preprint arxiv 1204.2176.

[68] V. Mirabet, P. Auger, and C. Lett. Spatial structures in simulations of animal grouping. Ecological Modelling, 201(3-4): 468-476, 2007

[69] A. Mogilner, L. Edelstein-Keshet, L. Bent and A. Spiros, Mutual interactions, potentials, and individual distance in a social aggregation, J. Math. Biol., 47 (2003) 353-389.

[70] S. Motsch, M. Moussaïd, E.G. Guillot, M. Moreau, J. Pettré, G. Theraulaz, C. Appert-Rolland, P.Degond, Pedestrian counterflow drives cluster dynamics and traffic efficiency, submitted.

[71] S. Motsch, L. Navoret, Numerical simulations of a non conservative hyperbolic system with geometric constraints describing swarming behavior, Multiscale Model. Simul., 9 (2011) 1253-1275.

[72] S. Motsch, E. Tadmor, A new model for self-organized dynamics and its flocking behavior, J. Stat. Phys., 144 (2011) 923-947.

[73] D. A. Paley, N. Ehrich Leonard, R. Sepulchre, D. Grünbaum, J. J. Parrish, Oscillator models and collective motion, IEEE Control Syst. Mag., 27 (2007), 89-105.

[74] T. J. Pedley, N. A. Hill, J. O. Kessler, The growth of bioconvection patterns in a uniform suspension of gyrotactic micro-organisms, J. Fluid. Mech., 195 (1988) 223-237.

[75] F. Peruani, A. Deutsch, M. Bär, Nonequilibrium clustering of self-propelled rods, Phys. Rev. E 74 (2006) 030904(R).

[76] F. Peruani, A. Deutsch, M. Bär, A mean-field theory for self-propelled particles interacting by velocity alignment mechanisms, Eur.Phys.J.Special Topics 157, 111-122(2008)

[77] Fernando Peruani, Tobias Klauss, Andreas Deutsch and Anja Voss-Boehme Traffic Jams, Gliders, and Bands in the Quest for Collective Motion of Self-Propelled Particles, Phys. Rev. E 106, 128101 (2011)

[78] F. Peruani, F. M. Nicola, L. G. Morelli, Mobility induces global synchronization of oscillators in periodic extended systems, New J. Phys., 12 (2010) 093029.

[79] V. I. Ratushnaya, D. Bedeaux, V. L. Kulinskii, A. V. Zvelindovsky, Collective behavior of self propelling particles with kinematic constraints: the relations between the discrete and the continuous description, Phys. A 381 (2007). 39-46.

[80] I. H. Riedel, K. Kruse, J. Howard, A self-organized vortex array of hydrodynamically entrained sperm cells, Science, 309 (2005), 300-303.

[81] D.Saintillan and M.J.Shelley, Instabilities and Pattern Formation in Active Particle Suspensions: Kinetic Theory and Continuum Simulations, Phys Rev. Lett, 100. 178103 (2008)

[82] D. Saintillan, M.J. Shelley, Instabilities, pattern formation and mixing in active suspensions, Phys.Fluids 20 (2008) 123304.

[83] D Saintillan and M J Shelley, Instabilities, pattern formation, and mixing in active suspensions, Physics of fluids 20, 123304 (2008).

[84] D.Saintillan and M.J.Shelley, Emergence of coherent structures and large-scale flows in motile suspensions, J. R. Soc. Interface (2012) 9.

[85] R. Sepulchre, D. A. Paley, N. Ehrich Leonard, Stabilization of planar collective motion with limited communication, IEEE Trans. Automat. Control, 53 (2008) 706-719.

[86] K.Sugawara Y.Hayakawa, T.Mizuguchi and M.Sano, Collective Motion of Multi-Robot System based on Simple Dynamics, in Human Robot Interaction edited by N.Sarkar (2007), chap 20, pp.357-368

[87] B.Szabó, G.J Szöllösi, B. Gönci, Zs. Jurányi, D. Selmeczi, and T. Vicsek Phase transition in the collective migration of tissue cells: Experiment and model, Phys. Rev. Lett, 74. 061908 (2006).

[88] M E. Taylor. Partial Differential Equations III, Applied Mathematical Sciences Series, Vol. 117, Springer, 1996, 2011.

[89] Jake P.Taylor-King, Benjamin Franz, Christian A.Yates and Radek Erban, Mathematical modelling of turning delays in swarm robotics, submitted.

[90] J. Toner and Y. Tu, Flocks, Long-range order in a two-dimensional dynamical XY model: how birds fly together. Phys. Rev. Lett., 75 (1995) 4326-4329

[91] J. Toner, Y. Tu and S. Ramaswamy, Hydrodynamics and phases of flocks, Annals of Physics, 318 (2005) 170-244

[92] Y. Tu, J. Toner and M. Ulm, Sound waves and the absence of Galilean invariance in flocks. Phys. Rev. Lett., 80 (1998) 4819-4822.

[93] T. Vicsek, A. Czirók, E. Ben-Jacob, I. Cohen, O. Shochet, Novel type of phase transition in a system of self-driven particles, Phys. Rev. Lett., 75 (1995) 1226-1229.

[94] T. Vicsek, A. Zafeiris, Collective motion, Phys. Rep., 517 (2012) 71-140.

[95] C.A. Weber, T.Hanke, J.Deseigne, S.Léonard, O.Dauchot, E.Frey and H.Chaté, Long-range ordering of vibrated polar disks, Phys. Rev. Lett., 110 (2013).

[96] F. G. Woodhouse, R. E. Goldstein, Spontaneous Circulation of Confined Active Suspensions, Phys. Rev. Lett. 109 (2012) 168105.

Résumé

Dans cette thèse, nous étudions le comportement collectif de particules auto-propulsées. Ce travail comporte trois parties.

Dans la première partie, nous considérons un modèle individu-centré pour les particules d'auto rotation interagissant par une règle d'alignement et étudions leurs limites macroscopiques. Deux cas de scaling ont été étudiés. Dans le cas de petite vitesse angulaire, le modèle obtenu est une légère modification du modèle 'Hydrodynamique auto-organisé' qui avait été introduit précédemment par Degond et Mostch. Dans le cas de grande vitesse angulaire, le modèle obtenu est plus compliqué. Une étude préliminaire de la stabilité linéaire a été également proposée.

Dans la deuxième partie, nous étudions un modèle macroscopique du système de particules auto-propulsées interagissant avec leurs voisins par une règle d'alignement et de répulsion. Nous fournissons une validation numérique de ce modèle en le comparant avec le modèle individu centré. L'existence de solutions du modelè macroscopique à deux dimensions est prouvée.

La dernière partie est consacrée à l'étude expérimentale du comportement collectif de robots auto-propulsés dans une enceinte annulaire confinée.

Mots clés: Mathématiques et Biologie, Modèle Individu Centré, Équations Cinétiques, Modèles Macroscopiques. Solutions numeriques, Suspensions actives, Mouvement collectif.

Abstract

In this thesis we study collective motions of self-propelled particles. This work consists of three parts.

In the first part, we consider an Individual-Based Model for self-rotating particles interacting through local alignment and investigate its macroscopic limit. We study the mean-field kinetic and hydrodynamic limits of this system within two different scalings. In the small angular velocity regime, the resulting model is a slight modification of the 'Self-Organized Hydrodynamic' model which has been previously introduced by Degond and Motsch. In the large angular velocity case, the macroscopic model obtained is more complex. A preliminary study of the linearized stability is proposed.

In the second part, we study a macroscopic model for a system of self-propelled particles which interact with their neighbors via alignment and repulsion. We provide a numerical validation of the continuum model by comparison with the particle model. The existence of local solutions of this macroscopic model is also studied.

The last part concerns experimental investigation of collective behavior of simple robots in a confined ring.

Key words: Mathematics and Biology, Individual Based Model, Kinetic Equations, Macroscopic Models, Numerical solutions, Active Suspensions, Collective Motion.